Alma Mater Studiorum – Università di Bologna

DOTTORATO DI RICERCA IN

CHIMICA

Ciclo XXVII

Settore Concorsuale di afferenza: 03/C2
Settore Scientifico disciplinare: CHIM/04

Selective oxidation of 5-hydroxymethylfurfural using monometallic and bimetallic supported nanoparticles

Presentata da: Alice Lolli

Coordinatore Dottorato	**Relatore**
Prof. Aldo Roda	**Prof.ssa Stefania Albonetti**
	Correlatore
	Prof. Fabrizio Cavani

Esame finale anno 2015

SOMMARIO

ABSTRACT

This work deals with the oxidation of 5-hydroxymethylfurfural (HMF) to 2,5-furandicarboxylic acid (FDCA) using metal supported catalysts. The reaction was performed in mild conditions, using water as solvent, in the presence of a base and O_2 as oxidant. Catalysts were prepared from the immobilisation of preformed monometallic (Au, Pd) and bimetallic (AuCu, AuPd) nanoparticles with different morphology and metal molar ratio on commercial oxides (TiO_2, CeO_2). Au-TiO_2 catalyst was found to be very active for HMF oxidation; however this system deactivated very fast. For this reason, we prepared bimetallic gold-copper nanoparticles and an increase in the catalytic activity was observed together with an increase in catalyst stability. AuCu with a molar ratio Au:Cu 3:1 was the most active sample and the interaction between the alloyed metals enhanced the catalytic performance. In order to optimise the interaction of the metal active phase with the support, Au and AuCu nanoparticles were supported onto CeO_2, which is characterised by greater redox properties and surface defects sites. Au-CeO_2 catalyst was found to be more active than the bimetallic one, leading to the conclusion that in this case the most important feature is the interaction between gold and the support. Catalyst pre-treatments (calcination and washing) were carried out to maximise the contact between the metal and the oxide and an increase in the FDCA production could be observed. The presence of ceria defective sites was crucial for FDCA formation. Mesoporous cerium oxide was synthesised with the hard template method and was used as support for Au nanoparticles to promote the catalytic activity. In order to study the role of active phase in HMF oxidation, PdAu nanoparticles were supported onto TiO_2. Au and Pd monometallic catalysts were very active in the formation of HMFCA (5-hydroxymethyl-2-furan carboxylic acid), but Pd was not able to convert it, leading to a low FDCA yield. On the contrary, Au and PdAu samples catalysed FDCA formation. The calcination of PdAu catalysts led to Pd segregation on the particles surface, which changed the reaction pathway and included an important contribution of the Cannizzaro reaction. PVP protected PdAu nanoparticles, synthesised with different morphologies (core-shell and alloyed structures), confirmed the presence of a different reaction mechanism when the metal surface composition changes.

AIM OF THE WORK

This work deals with the synthesis of active and stable catalysts that can be used for the oxidation of 5-hydroxymethylfurfural (HMF) into 2,5-furandicarboxilic acid (FDCA) in liquid phase. At first, monometallic (Au, Pd) and bimetallic (AuCu, AuPd) nanoparticles were prepared in different metal molar ratio and morphologies (alloy and core-shell structure), using a simple procedure which requires β-D-glucose as reducing agent and PVP (polyvinylpyrrolidone) as stabiliser, in a basic water solution. Then, they were supported onto TiO_2 and CeO_2 using the incipient impregnation method. All sols and supported catalysts were characterised with DLS (Dynamic light scattering), XRD (X-ray diffraction), HRTEM (High Resolution Transmission Electron Microscope), surface area and porosimetry measurement, TPR/O analysis (Temperature Programmed Reduction/Oxidation), TGA (Thermogravimetric analysis) and DTA (Differential Thermal analysis).

The prepared catalysts were tested in the liquid phase oxidation of 5-hydroxymethylfurfural (HMF). Catalytic tests were performed in an autoclave reactor using water as solvent, O_2 pressure as oxidant in the presence of NaOH; reaction temperature was set in the range 60-90°C.

AuCu based catalysts supported on CeO_2 were studied with a view to increase the activity and selectivity in HMF oxidation by optimizing the interaction both between the metals and with the support. With this aim several pre-treatments were performed on the prepared catalysts in order to activate the materials, by getting rid of the organic stabiliser (PVP, polyvinylpyrrolidone), which surrounds metal nanoparticles and therefore maximizing the contact between the metal and the support. The influence of the following pre-treatments on the catalytic activity was studied in detail:

- ✓ Calcination 300°C
- ✓ Washing in reaction conditions (in the autoclave reactor)
- ✓ Washing in reaction conditions and calcination 300°C

Since the activity of cerium oxide based catalysts is strictly correlated to defects formation, redox properties and gold-support interactions, the use of supports with high surface areas and regular-shaped mesopores seemed to be worthy of investigation. With this aim, hard-templated cerium oxide samples have been synthesized, thoroughly characterized and used as support for pre-formed gold nanoparticles.

Finally the role of active phase composition and morphology was investigated by preparing bimetallic PdAu catalysts in order to investigate the effect of these parameters on the catalytic activity and product selectivity in the oxidation of HMF. HMF reaction pathway was studied using unsupported alloyed and core-shell nanoparticles to observe the different reaction mechanism that takes place exposing preferentially Pd or Au atoms on the surface.

CHAPTER 1

Introduction

1.1 Biomass as an alternative source for the synthesis of fuels and chemicals

During the last decades, many efforts have been devoted to the study of biomass conversion in order to produce fuels and chemicals. The decrease of fossil sources is one of the main reasons which have been favouring the exploitation of the renewable resources, together with the environmental impact. As a matter of fact, the production of energy from renewables is considered to be CO_2 neutral if compared to fossil fuels[1], allowing the reduction of the greenhouse gas emissions. The increase in the oil price and some geopolitical issues correlated to the location of petroleum reserves have been enhanced the production of fuels and chemicals from alternative sources. Furthermore, the possibility of the use of waste material for chemicals and fuels production could also be useful to solve partially the problem of waste production. From the ethic point of view, the use of second generation bio-fuels produced from lignocellulosic materials avoids food competition. Another advantage that is present in the use of biomass for fuels and chemicals production is that it can be found in high quantity all around the world. This could help to avoid political problems between countries, since every country has its own source within its boundaries.

However, the cost of fuels produced from biomass is still higher than that produced from oil and it has been estimated from the International Energy Agency that in 2030 fuels from biomass will cover only the 14% of the total[2]. The cost of biofuels depends on biomass feedstock which is correlated to its location and its availability. Market fluctuation together with plant and process costs should be taken into account. In order to lower these costs, it is very important to adapt biofuels synthesis and transportation with the actual infrastructure and to use biomass produced within a short distance from the chemical plant in order to reduce CO_2 emission due to transportation.

Another interesting aspect of the biorefinery is the creation of a bio-based industry for the production of polymers and chemicals. The biorefinery concept is the transformation of carbohydrates, lignin and oil obtained from biomass to produce fuels, chemicals and other materials with a high added-value. One of the advantages that is correlated to the exploitation of biomass for the production of platform molecules is their high level of functionalization. In these molecules a high number of functional groups is present and this peculiar characteristic could limit the number of the following chemical reactions, favouring one of the main Green Chemistry principles such as the reduction of reaction steps. Biorefinery processes can be divided into two main categories which includes either biochemical (basically from sugars fermentation) or thermochemical processes, usually gasification or pyrolysis for syngas production[3].

1.1.1 Biomass conversion

Full biomass exploitation and reduction of transportation costs are key factors for biorefinery processes. However, several new technologies must be taken into consideration, namely separation, fermentation, pressing, classification and drying talking about biomass conversion. It is also necessary to consider the complicated nature of biomass, which consist of a mixture of cellulose, hemicellulose, starch, lignin and chitin. Sometimes, proteins, wax, organic acids, fats, minerals and free sugars can be included. Due to its heterogeneous composition, several approaches can be followed for converting biomass[4]:

- Considering its heterogeneous nature, it is possible to convert it into syngas, used in chemical industry
- Developing specific reactions to convert single components into valuable building blocks (approach used for agricultural crops with a high protein content)
- Separating the different component and converting them into “pure” building blocks (for lignocellulosic biomass)
- Using a combination of the previous reported approaches.

Biomass conversion can occur using a gasification process, leading to the formation of syngas. The latter can be transformed into methanol or hydrocarbons with the Fisher-

Tropsch reaction, following the reaction pathways already used for petroleum feedstock. This process can lead to the synthesis of chemicals; however, since it requires high process temperature, its sustainability still has to be verified. A different approach for the combined gasification/Fisher-Tropsch reaction can be the aqueous phase reforming yielding directly to H_2, CO_2 and alkanes. In this case the starting material is made up of sugar polyols, derived from lignocellulosic material such as wheat straw[5] or glycerol[6,7].

Pyrolysis can be considered another route to obtain chemicals from degraded molecules. This process is performed at high temperature in absence of oxygen and lead to the formation of gas, tar and bio-oil which is formed by a mixture of different compounds. The composition of the bio-oil is strictly correlated to the nature of the starting material. However, fragments of cellulose, hemicellulose and lignin can be found as well as phenolic compounds which derive from lignin degradation. Both gasification and pyrolysis are energy demanding processes and their sustainability has to be verified by means of Life Cycle Assessment[1].

Catalytic reactions can be used to convert renewable feedstock into a mixture of products: for example, polyols can be obtained from polysaccharides through several catalytic reactions.

For the production of fine chemicals from carbohydrates another approach that is used for biomass conversion is platform molecules synthesis. With this aim, lignocellulosic waste material could be used and fermentation or catalytic conversion can be carried on.

1.1.2 Lignocellulosic biomass conversion

From the ethic point of view, the use of lignocellulosic material as biomass source can be considered the best way to produce fuels and chemicals from renewables, since it prevents food competition. It also reduces intensive cultivation, allowing the use of biomass from marginal lands. Cellulose (38-50%), hemicellulose (23-32%) and lignin (15-30%) are the main components of lignocellulosic materials. This source is very abundant since it is the key structural element of plants; however it is also present in agricultural waste (sugarcane bagasse, wood residues, saw and paper mill waste) and municipal paper waste. The depolymerisation of this material leads to the formation of monosaccharides, which can be further converted to platform molecules, as reported in Figure 1-1.

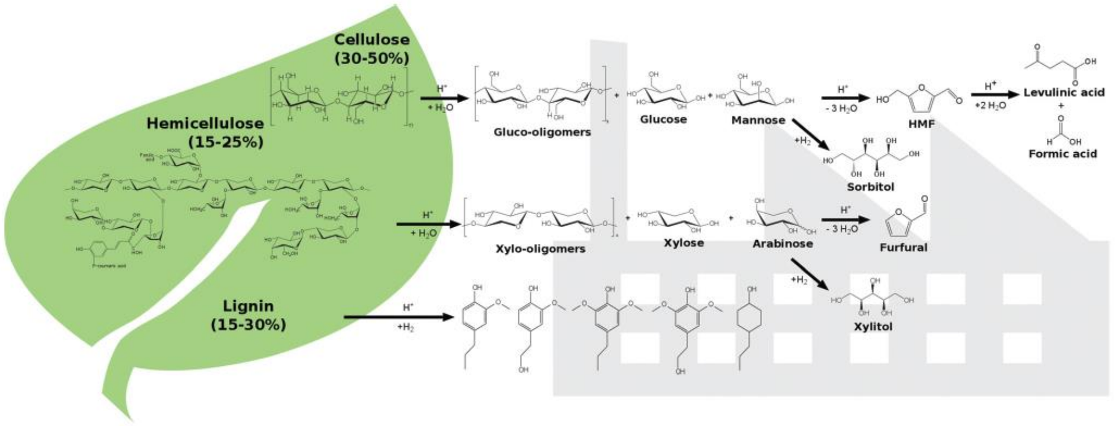

Figure 1-1 Platform molecules preparation from lignocellulosic biomass[8].

Cellulose and hemicellulose are natural polymers made up of molecules connected by β-1,4-glucoside bond. Hemicellulose is mainly composed of C5 sugar, namely xylose and it is chemically linked to lignin. It is positioned at the interface between cellulose and lignin. Cellulose and hemicellulose can be hydrolysed in water at high temperature (> 300°C) or in the presence of an acid catalyst. Because of its high crystallinity, that is mainly due to hydrogen bonds between adjacent chains, cellulose is not hydrolysed easily. On the contrary hemicellulose can be hydrolysed more faster, forming mainly xylose, its major constituent. Therefore, hemicellulose hydrolysis happens first at lower temperature and xylose can be separated from the remaining cellulose. Increasing the temperature cellulose hydrolysis occurs leading to the formation of glucose. However, the following aspects must be considered before approaching a chemo or bio process for lignocellulose conversion:

- Lignin amount; in particular for enzymatic processes, it is necessary to lower lignin content since it can avoid the interaction between the catalyst and the carbohydrates
- Hemicellulose amount
- Degree of crystallinity and polymerisation for cellulose; for a higher degree of crystallinity cellulose cannot be easily attacked.

Cellulose depolymerisation can be catalysed by enzymatic processes. Many biological reactions take place in nature but these enzymatic processes are too slow for industries.

Therefore, it is possible with several pre-treatments to accelerate the process of biomass conversion getting rid of lignin and hemicellulose, reducing the crystallinity and the polymerisation degree belonging to the structure of cellulose, increasing its surface area[2]. With respect to chemo-catalytic reactions, enzymes can be more selective and can be easily stocked. However, they are characterised by a lower reaction rate and the use of these materials for industrial processes is still a matter of debate because of their expensive costs. The utilised hydrolysis processes are reported in Figure 1-2.

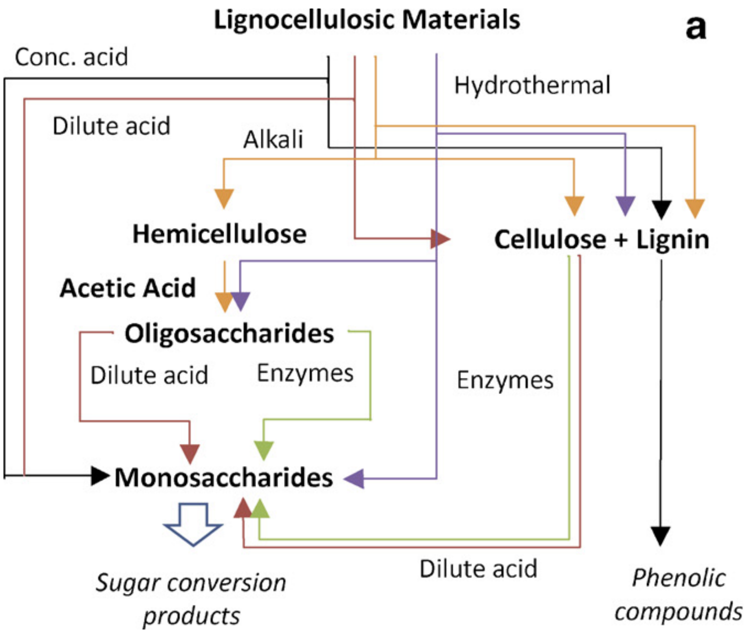

Figure 1-2 Biomass processes[2].

Concentrated solution of mineral acid such as H_2SO_2 and HCl and gaseous HF have been used for cellulose and hemicellulose depolymerisation. However, all these treatments leave a great fraction of oligomers; in order to produce monomers, this step has to be followed by a further hydrolysis reaction, diluting the oligomer solution in water and adding a dilute acidic solution (0.5-5%wt acid). In this case, higher temperature should be reached and this reaction should be carefully controlled since sugars degradation can occur in this medium and it is favoured by an increase in the reaction temperature (Figure 1-3)[8]. Hemicellulose sugar stability can be increased in the presence of a mixture of H_3PO_4:H_2SO_4 in the ratio 7:3[9]. Using mineral acids, high sugar yield can be obtained but it is necessary to develop a process for acid recovery after reaction so that the whole process could be considered competitive. Combining the acid treatment with the biomass milling, it is possible to achieve high products yield using a lower acid content, reducing the recovery costs. In this case it has to be considered the energy request of the high energy mill, in order to estimate the total economic impact of the process. The acid content could be also lowered if ionic liquids and solvents are used for cellulose solubilisation. Hydrothermal processes can also be performed; however, they require high temperature and low residence time. In fact, in these conditions sugar degradation happens faster than biomass hydrolysis[8].

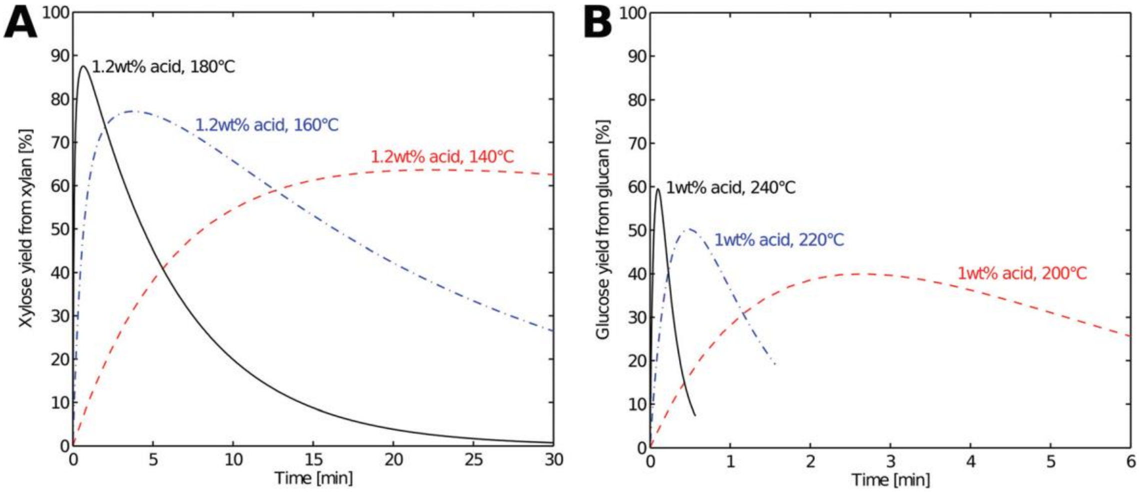

Figure 1-3 Xylose (A) and glucose (B) yields obtained with mineral acid hydrolysis of hardwood[8].

However, these homogeneous processes are very expensive in terms of products separation and recovery. For this reason, many recent researches have been focused on the development of heterogeneous catalysts. Ru and Pt supported catalyst have found to be active in the formation of hexitols under mild conditions[10]. The catalytic approach seems to be more promising with respect to the enzymatic one, since the latter requires longer reaction time.

Since both monosaccharides synthesis and sugar conversion take place with the same active catalyst, it is theoretically possible to start from biomass and obtain platform molecules, performing an one pot synthesis. Several processes are involved into biomass conversion, namely hydrolysis, dehydration, isomerisation, reforming, aldol condensation, hydrogenation, selective oxidation and hydrogenolysis. Hydrolysis and dehydration reaction lead to the synthesis of two main platform molecules such as furfural and 5-hydroxymethyl furfural (HMF), which can be further converted by means of oxidation, hydrogenation, rehydration and aldol condensation for solvents, fuels and monomers production. From HMF oxidation DFF (2,5-diformylfuran) and FDCA (2,5-furandicarboxylic acid) can be formed and from HMF hydrogenation BHMF (2,5-bishydroxymethylfuran) and BHM-THF (2,5-bishydroxymethyltetrahydrofuran) can be synthesized (Figure 1-4). All these compounds are used in the polymer industry for polyesters, polyurethanes and polyamides production. Moreover, HMF rehydration leads to the formation of levulinic acid, which can be converted to levulinate ester, used as fuel additive, by means of esterification reaction[11].

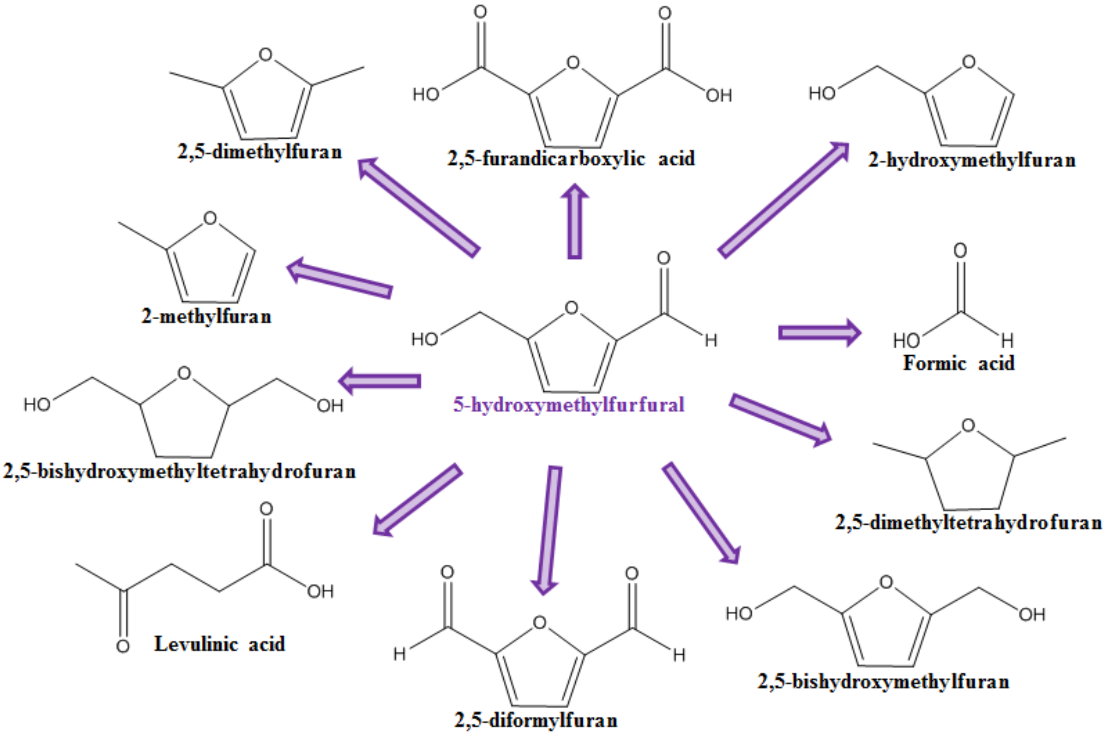

Figure 1-4 Main HMF derivatives.

1.2 HMF synthesis

HMF is considered to be one of the most important “sleeping giants”. It has been studied for more than one hundred years and during the last decade it has gained much more importance. This aspect can be gathered by looking at the number of publication which concerns this topic and how fast it has increased during more recent years. The

synthesis of HMF has been first published in 1895 by Dull and Kiermeyer[12]; many research projects have been carried on from the beginning of the XXth century up to now. HMF can be synthesized from a triple dehydration of hexoxes (fructose e glucose) or even directly from cellulosic or lignocellulosic feedstock. Ketohexoses can produce HMF more efficiently and with higher selectivities with respect to aldohexoses. In fact, the hydrolysis of sucrose is faster than the dehydration of glucose and sometimes in the final mixture an excess of glucose can be found. Furthermore, the aldehydic group of glucose can react either with another molecule of glucose or with HMF, forming some oligomers. For these reasons, it can be more convenient to isomerise glucose into fructose to synthesize HMF. However, HMF stability must be taken into consideration since it is one of the major problems that has to be faced during its synthesis. In fact, in the presence of an acidic medium it can be degraded to form levulinic and formic acids. The production of HMF with high selectivity, is a very demanding goal due to the high reactivity that characterises this compound.
Sugar dehydration can be performed with the following catalysts:

- Mineral and organic acids
- Solid acid catalysts

The involved catalytic processes can either be homogeneous or heterogeneous; the latter is more efficient in terms of catalyst separation, recyclability and process safety.

1.2.1 Mineral and organic acids

Mineral acids, such as H_2SO_4, H_3PO_4, HCl, HI can be used for HMF synthesis. For example, H_2SO_4 in sub-critical water at 250°C led to a 53% yield of HMF from fructose[13]. When acetone was used as solvent at 180°C under sub-critical conditions HMF yield rose up to 72%[14].
HMF synthesis starting from glucose is characterised by lower selectivity and lower reaction rates. As matter of fact, in the presence of H_3PO_4 as catalyst only 15% of yield was achieved at 190°C. More efficient processes were developed using biphasic systems. These processes allowed a continuous extraction of HMF in the organic phase, avoiding a prolonged contact of the substrate with the acid catalyst and preventing condensation reaction and humins formation (Figure 1-5).

Dumesic et al.[15] performed an acquous phase dehydration from D-fructose using HCl as catalyst. HMF was continuously removed extracting the reaction mixture with methylisobutylketone (MIBK), in order to product degradation; yields up to 90% were reached.

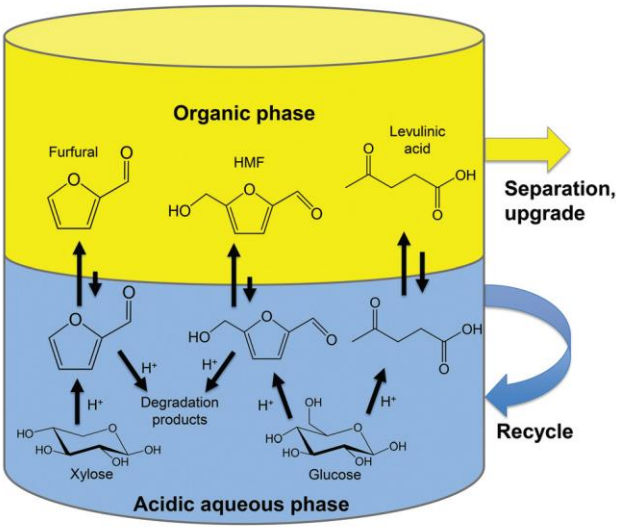

Figure 1-5 Biphasic system for producing dehydration products from lignocellulosic materials[8].

It is also possible to synthesize HMF from biomass feedstocks, like polysaccharides, cellulose and lignocellulose. This is a very promising process from the industrial point of view because it is a so-called one pot synthesis, which eliminate one reaction step. This could be easily performed since both the dehydration step and the hydrolysis reaction are performed with the same acid catalyst. Higher yield were obtained using a biphasic system and H_3PO_4 as catalyst[16]. Furthermore, H_2SO_4 in a biphasic reaction mixture containing N,N-dimethyacetamide, can be used producing high HMF yields at 100°C for 5h[17].

Some organic acid such as oxalic acid were used as catalyst, but they were not convenient from the economical point of view.

1.2.2 Solid acid catalysts

Ion-exchange resins, vanadyl phosphate TiO_2, ZrO_2 and Al_2O_3[19] have been used as solid acid catalysts for HMF synthesis. They are better catalysts if compared to the homogeneous one because they can work at higher temperatures, they can be easily separated and they can be modified in order to obtain different level of acidity, which can help to avoid by-products formation. The modification of these materials, obtained with the introduction of other elements, modified the acid-base properties which influenced the reaction mechanism. As a matter of fact, glucose isomerisation to fructose is favoured by basic sites, while fructose dehydration is promoted by acid sites.

Ion exchange resins such as Amberlist-15, Dowex 50wx8-100 and the zeolite H-mordenite gave the best result in terms of HMF yield[18]. Moreover, the use of non-protic solvents such as DMSO could prevent levulinic acid and humins formation.

Even porous material have been studied for HMF production. In particular, zeolites (H-2SM5, H-Mordenite, H-BEA, H-Y Faujasite) with their tuneable acidity, shape selectivity and high thermal stability have been investigated in the carbohydrates dehydration reaction. H-Mordenite was found to be very active and selective towards HMF formation, since its characteristic bidimensional shape allowed a fast diffusion of the substrate within its porosity. On the contrary, in the relative bigger porosity characteristic of H-Y Faujasite, some molecular rearrangements could take place and HMF and fructose degradation may occur[19]. H-BEA zeolite was not considered a good catalyst for this reaction, since it favoured too much HMF hydration.

Mg-Al hydrotalcites were used in a recent work to promote glucose isomerisation to fructose[20]. Lantanoid metals were used to catalyse sugar dehydration together with Cu, Cr, Sn salts. All the element belonging to the lantanoid group are active in HMF synthesis in the aqueous media and they can avoid levulinic acid formation.

1.3 Applications: HMF oxidation

Biomasses are currently the most promising alternative to fossil sources for the production of fuels and chemicals[11,21]. In the transformation of biomass into chemicals, an important role is played by furfural derivatives that have functional groups in position five[22,23]. For instance, 5-hydroxymethyl-2-furfural (HMF) is a key precursor for the synthesis of derivatives with application in the pharmaceutical and polymer industries[11,24,25,26].

5-hydroxymethylfurfural can be oxidized to obtain 2,5-furandicarboxylic acid (FDCA), a monomer for the synthesis of a new class of polymers, alternative to those obtained from terephthalic acid. As an example, Avantium is using FDCA to produce polyethylene furandicarboxylate (PEF); the exact route for the synthesis of FDCA has not yet been disclosed, but the current technology for terephthalic acid production using metal/bromide catalysts is probably being evaluated. One drawback of these catalytic systems is the use of corrosive media and dangerous compounds, which make the process polluting[27,28,29]. At the beginning, this reaction was studied using stoichiometric oxidants such as N_2O_4, HNO_3 and $KMnO_4$. Nowadays, it has been found out gold supported catalysts can be very active and the research has been focused on the study of the best support. Corma et al[30]. studied HMF oxidation using gold supported onto C, CeO_2, TiO_2 and Fe_2O_3 in the presence of a base. Moreover, there are concerns regarding the purity of both the product and the final polymer. However, since many big companies are interested in bio-based packaging, the process for FDCA production has been deeply investigated. Since the market is very sensitive to the green image of the product, some companies such as Coca-Cola and Danone are trying to decrease the utilisation of fossil resources. Although, it is not just a matter of commercial advertisement since the use of these material can really low the environmental impact. Using PEF, both the amount of non-renewable energy used and greenhouse gases emissions could be halved, if compared to the environmental impact of PET production[31]. Other compounds could be obtained from HMF oxidation: 5-hydroxymethyl-2-furancarboxylic acid (HMFCA) and diformylfuran (DFF). The previous one has been obtained using silver oxide and a mixture of silver and copper oxides in basic condition[32]. However, this is one of the key intermediate to form FDCA and can be obtained high yield using Pd, PdAu, AuCu, Au supported catalysts, like it is reported in our works[50,]**Errore. Il segnalibro non è definito.**[,56]**Errore. Il segnalibro non è definito.**. Gorbanev[39] reported HMFCA production using Au-TiO_2 at ambient temperature and Davis[33] obtained 92% selectivity using Au-C and Au-TiO_2. The selective preparation of the DFF, has gained even more importance from the industrial point of view since it is a very versatile compound, which can be used in several polymeric application (resins and ligands). Diformylfuran preparation were studied using $BaMnO_4$, $KMnO_4$, NaOCl, PCC, TMACC and TEMPO as oxidant, which are very expensive and toxic substances. Recently, processes which use O_2 as oxidant have been developed and one of the most active catalyst has been found to be V_2O_5-TiO_2[34]. Ru based catalysts are found to be very selective for the oxidation of HMF to DFF. As a matter of fact, Ru clusters supported onto CTF (covalent triazine frameworks) and other support such as activated carbon, γ-Al_2O_3, hydrotalcites and MgO[35] and Ru-metallorganic complexes supported on carbon nanotubes[36] were investigated. Moreover, trimetallic mixed oxide Ru-Co-Ce were found to be very active for DFF formation[37]. Finally, a very recent paper shows high selectivities in DFF formation[38].

1.3.1 Influence of the active phase and support: Gold based catalysts

Recently Au-supported catalysts were found to be very active for HMF oxidation to FDCA[39,40]. Even if gold it is not active as bulk material, its reactivity increases when it is present in nanometric size. As a matter of fact, there are four main factors responsible for gold nanoparticles catalytic activity:

1. Particle size and shape
2. Metal-support interaction
3. Presence of cationic species
4. Synthesis and pre-treatment procedure.

Gold catalytic activity is strictly correlated to particles size. In general, the smaller the particle the higher is the metal dispersion onto the support. This means that a greater number of particles can be in direct contact with the support, thus creating more defective sites such as terraces, edges and corners. Moreover, atoms can interact more easily and surface mobility increases. Recently, it has been demonstrated that even gold particles characterised by bigger dimensions (20-45 nm) can still be considered active for the aqueous phase oxidation of alcohols in the presence of a base. However, their activity decreases with the increase of particle size and it is more dependent to the base content[41].

The role of the support in gold supported catalysts is to increase particle stability during the catalytic tests and eventually during pre-treatment procedure. However, the use of different support characterized by different defective sites, influences the catalytic activity. For example, it is reported that for CO oxidation the catalytic activity depends both on Au size and the type of support[42]. The aerobic oxidation of the HMF was performed using different gold supported catalysts. TiO_2 and CeO_2 are the most common support, which have been utilised to prepare this type of catalysts and they have also shown the best catalytic activity if compared to Fe_2O_3, and carbon. Moreover, a great influence of the support was highlighted by the use of nanoparticulate ceria, that displayed an enhanced activity with respect to the non-nanoparticualte one[30].

During the last decade, many researchers have focused their attention on the study of the type of active phase which is really responsible for catalysis. Some of them believe that the most important feature of gold based catalyst is the interface between Au and the oxide used as support[43].

Since the type of support and the catalyst preparation method have been playing a pivotal role on catalytic activity, different support and different synthetic procedure have been developed. TiO_2, CeO_2 and carbon are the most used support for catalyst preparation. Often, catalysts are prepared by incipient wetness and wetness impregnation, entailing the use of a solution with a volume equal to or greater than the pore volume of the support respectively. More frequently solutions of the metal precursor typically $HAuCl_4$ and $PdCl_2$ are directly impregnated onto the support; this methodology brings to the formation of particles with 10 nm as average diameter. On the other hand the deposition precipitation method, which causes salt crystal precipitation on the support, allows the formation of very small nanoparticles. It is also possible to prepare catalyst using colloid or organometallic complexes. In literature it has been reported that the use of mono and bimetallic carbonyl cluster (Au-Fe) supported onto SBA-15 were used to catalyse methanol combustion[44] and the complete oxidation of toluene, dichlorobenzene and methanol together with preferential CO oxidation in the presence of H_2[45]. The preparation of a metal nanoparticle suspension which is then impregnated onto the support gives the possibility to strictly control the features of the final nanoparticles in terms of size and shape. Furthermore, it allows the synthesis of bimetallic nanoparticles in form of alloy ore core-shell with different metal molar ratio. The following procedure have been recently studied for nanoparticles synthesis:

1. Sol-gel method
2. Microemulsion
3. Hydrothermal synthesis
4. Gas phase synthesis
5. Synthesis procedure using polyols
6. Synthesis in water

From the among cited preparation methodologies, the latest it the most interesting since it can get rid of organic solvent and expensive equipment. Nanoparticles synthesis could be performed in water in the presence of reducing and protective agents. If it is present in excess, the reducing agent could be also used as stabilizing agent; this is the case of glucose, which can be both the reducing and the protective agent[46]. β-D-glucose is a reducing sugar and its reducing power can be emphasised adding NaOH. It has been demonstrated that the pH of the water solution is fundamental for the reduction of Au^{3+} atoms. Figure 1-6 reports UV-Vis spectra of a β-D-glucose 0.03M solution with different NaOH content. Undoubtedly, the absorbance increase with the base content and the gold plasmon band undergoes into a blue-shift, thus indicating the formation of smaller nanoparticles.

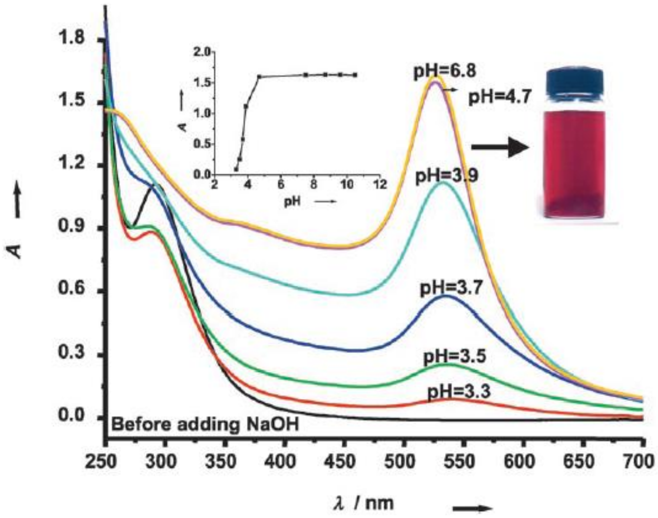

Figure 1-6 Nanoparticle suspension UV-Vis spectra for different pH values[46].

Moreover, the amount of reducing agent has to be optimized in order to obtain a controlled particle size distribution. In fact, it has been observed that an increasing amount of glucose in the solution would lead to particles with smaller size (Figure 1-7).

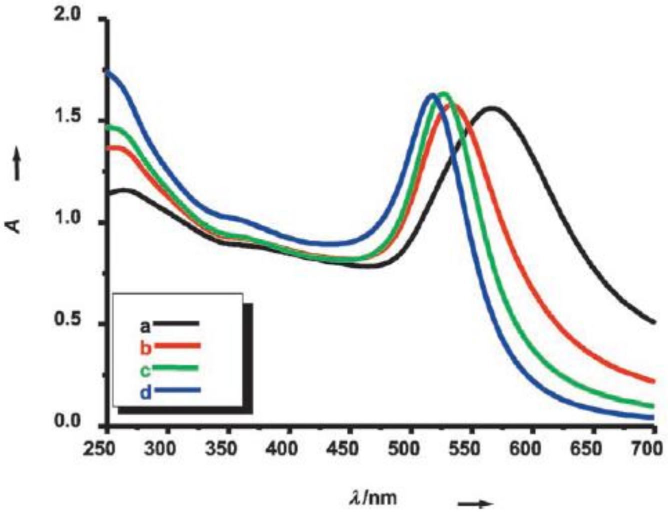

Figure 1-7 UV-Vis spectra of gold nanoparticle suspension with different β-D-glucose concentration. Legend: a) 0.005 M, b) 0.01 M, c) 0.03 M, d) 0,05 M.

One of the most utilized stabilising agents is PVP (polyvinylpyrrolidone) together with PVA (polyvinylalcohol). They are used as steric hindrance stabilising agents, creating a shell around the metal particle. Another important chemical characteristic of these polymers is their solubility in water. PVP is used not only as protective agent but it could also be used as reducing agent[47,48]. It has been demonstrated that the reducing power of PVP is mainly due to two features:

- the presence of OH terminal group; the reducing power increase with the decrease of the molecular weight and thus in the presence of a greater numebre of OH terminal
- PVP tendency to oxidation, due to the residual peroxo-group remained from the synthesis; this oxidation is also enhanced by the presence of cationic metals.

PVP content has to be optimised. As a matter of fact, the increase in the concentration of PVP revealed a decrease in the particle dimension. Furthermore, PVP concentration affected also particle shape, creating round and monodisperse nanoparticles for great PVP content[47]. Finally, the length of the polymer chain can influence particle size and shape. In general, small round nanoparticle are obtained with short chained PVP, while increasing the molecular weight of the polymer an increase of average diameter and the formation of polygonal particles could be observed. This is due to the fact that a longer PVP chain may favour the growth of the particles in particular crystallographic planes, giving rise to the formation of elongated particles[49].

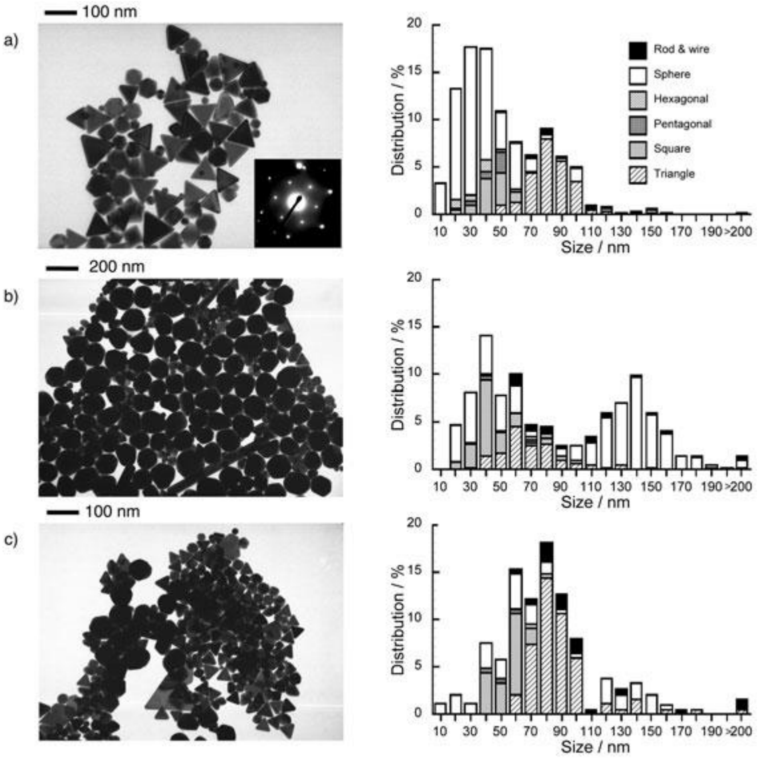

Figure 1-8 TEM images and particle size distribution for gold nanoparticles synthesized with PVP with different chain length. Legend: a) 10 K, b) 40 K, c) 360 K[49].

1.3.2 Influence of the active composition: Bimetallic catalysts[50]

According to the current state of the art, the use of bimetallic catalysts with controlled size and composition may be a promising way to improve catalyst activity and stability[51,52]. Most of the times, an increase in the catalytic performances has been observed due to the synergistic effect of the combination of the two metals, which brings an improvement in the chemical and physical properties if compared to the monometallic sample[53].

Bimetallic nanoparticles have a complex structure and different morphologies. As a matter of fact, they can be synthesised as core-shell structure, heterogeneous structure or in form of alloy (Figure 1-9).

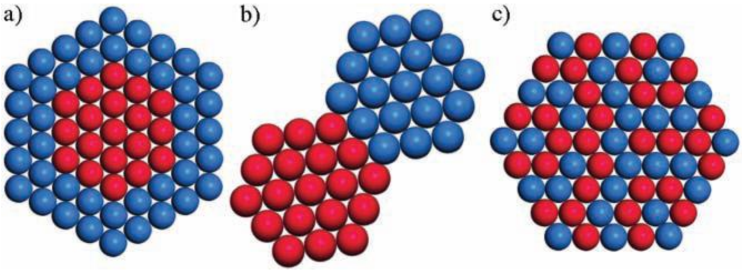

Figure 1-9 Different morphologies for bimetallic nanoparticles: a) core-shell, b) heterogeneous structure, c) alloy[54].

At first, in order to form core-shell particles, the reduction of the first metal has to take place; this will be the core of the structure. Then, the second metal will grow around the previous one since the spontaneous nucleation is not favoured if in the same ambient of reaction a seed has already been formed. However, in certain conditions the spontaneous nucleation of the two metals may occur forming heterogeneous structures. In this case, both metallic species are able to nucleate separately. As far as the alloy formation is concerned, they can be considered as homogeneous mixture of the two metals when new metal-metal bonds are formed. This is a fundamental characteristic of alloyed particles and it can be observed by means of a X-ray diffraction analysis. Heterogeneous and core-shell structures have the typical reflection peaks of the metals that are present in the structure, while for the alloys a peak shift could be observed. For instance, alloys have more ordered morphologies if compared to core-shell and heterogeneous structures.

All these bimetallic structures can be synthesised in solid, liquid and gas phase. It is possible to obtain bimetallic alloys with metallurgic techniques; nevertheless, solid state synthesis procedures are carried out at very high temperatures and they do not allow the formation a material with a high surface area. These bulk alloys are not catalytically active and this is the reason way nanomaterial have gained a great relevance in this field.

Even for the synthesis of nanoalloys, it is necessary to develop a strategy which allows a proper control of shape, size, composition and morphology. Sol-gel synthesis and microemulsion procedures are not used in this case because it is not possible to strictly control particle size. On the contrary, synthesis procedures performed in water and in solvents are the best methodologies to control nanomaterial properties, giving the possibility to change the characteristic of the particles by modifying some process parameters[55].

In our previous works[51,56], we prepared PVP-stabilized Au and Au-Cu nanoparticles supported onto TiO_2 using a simple strategy which enabled a careful size, structure and composition control. Unprecedented catalytic activity and stability were obtained with these catalytic materials in the oxidation of HMF to FDCA. Preformed AuCu colloidal nanoparticles, which were impregnated onto commercial TiO_2, showed a more interesting activity if compared to the monometallic counterpart. These catalysts not only increased the activity but also catalysts stability in the HMF oxidation reaction. The stabilisation effect due to copper content was demonstrated to be correlated to the amount of copper contained in samples[56]. The catalytic properties of this alloy were previously studied in other oxidation reactions, where it gave excellent results because for the ability of copper to better disperse gold nanoparticles. Au-Cu nanoparticles have been used for the oxidation of propene; the alloy with greater Cu content was shown to have the highest activity. These catalysts were also used for CO oxidation where they improved both the activity and the stability of the system with respect to the monometallic catalysts. In addition, benzyl alcohol oxidation gave good results using gold- copper supported catalyst; in this case the most active alloy was the one characterised by a bigger amount of gold[57].

The combination of Pd and Au was also shown to be very successful in producing active and selective catalysts[52,58]. This bimetallic system has been widely studied for a number of different applications[59,60]. In particular, Prati and co-workers[61,62,63] and Hutchings and co-workers[64,65] have demonstrated that the supported Pd-Au alloy shows excellent performances for many oxidation reactions such as the selective oxidation of alcohols and the synthesis of H_2O_2 from H_2 and O_2. This type of catalyst has also been tested in HMF oxidation; Villa et al.[66] have recently reported on the activity of Pd-Au supported catalysts, underling that the preparation of bimetallic systems with high gold content increased catalyst stability.

Depending on the type of synthesis and catalysts thermal treatment, it is possible to develop Pd-Au nanoparticles with different morphologies ranging from core-shell to homogeneous alloys[67]. One of the Pd-Au alloy most frequently used in catalytic applications is made up of Pd:Au in the molar ratio of 1:1. Nevertheless, it has been reported that metals concentration on the nanoparticles surface may be different from that of the bulk. Notably, Pd may migrate and concentrate in the outer part of the particles, developing a core-shell structure[68,69]; this phenomenon may significantly influence the catalytic activity.

1.3.3 Reaction mechanism

Aerobic alcohol oxidation reaction mechanism has been deeply investigated. It is very well known that using Au based catalyst, it is necessary to insert in the reaction mixture NaOH, which acts actually a co-catalyst. Prati and co-workers have demonstrated that polyols and sugars can be oxidised in water with gold catalyst only in the presence of a base[70]. The same results were obtained by Carretin[71] et al. for glycerol oxidation and by Klitgaard[72] for benzyl alcohol oxidation.

Sodium hydroxide has a relevant importance even for HMF oxidation as shown by Pasini et al.[51] and Davis and co-workers[73]. The presence of the base in an aqueous medium is fundamental for the hydration of the aldehydic group, forming a germinal diol through a nucleofilic addition of the OH^- to the carbonyl group and a proton transfer from H_2O[74]. The diol is then dehydrogenated to form the carboxylic acid, thanks to the OH groups that are present on the catalyst's surface (Figure 1-10). This reaction deposits two electron on the metal and after this, the alcohol chain is dehydrogenated after having been deprotonated by the base. C-H bond is activated by the hydroxide ions and the aldehyde is formed, leaving two more electron on the metal surface. Finally, the aldehyde is formed as previously described.

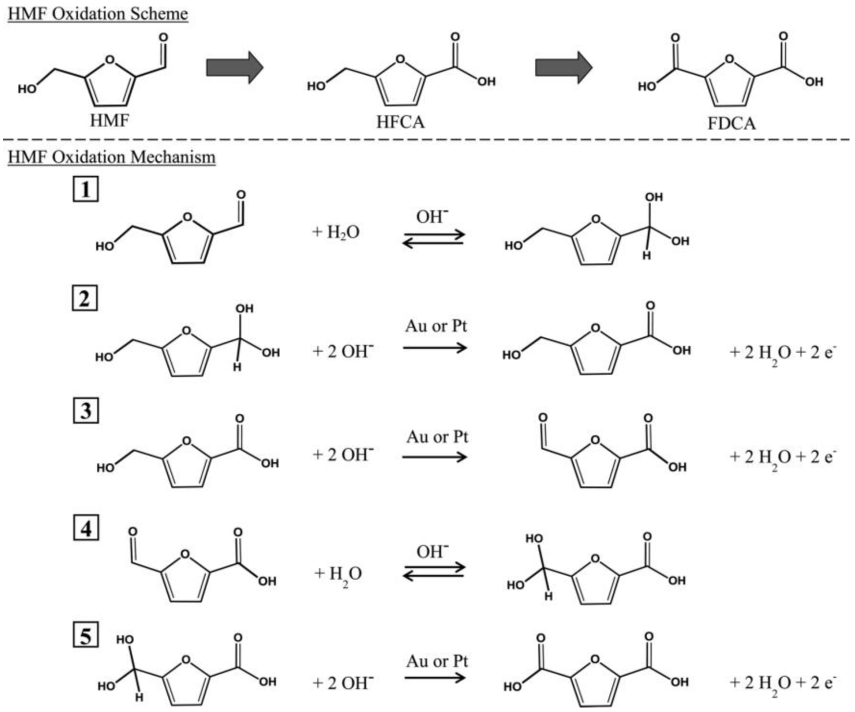

Figure 1-10 Overall reaction scheme and HMF reaction mechanism in aqueous solution in the presence of a base and Au catalyst[74].

This mechanism was previously demonstrated for other substrates such as ethanol and glycerol oxidation by Zope et al[75] (Figure 1-11).

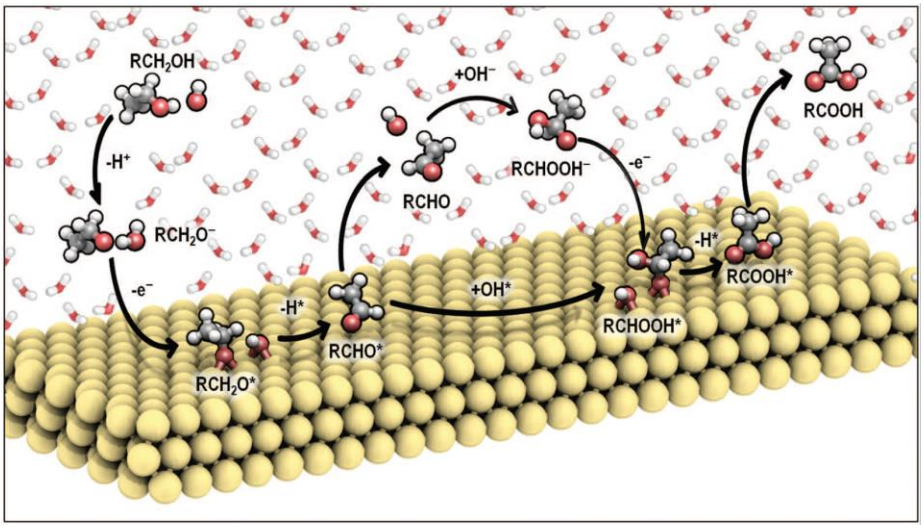

Figure 1-11 Reaction mechanism for alcohol oxidation over Au catalyst[75].

Experiments performed with $^{18}O_2$, showed that no ^{18}O was found in the obtained product (HMFCA and FDCA). However, the products selectivity decreases if the

oxygen is not insert into the reactor, giving rise to HMF degradation. Some H_2O_2 was observed in the solution and this can be explained by the formation of peroxospecies from the reaction of O_2 and water. Then, hydrogen peroxide decomposition led to the formation of surface OH^- groups which are used during the oxidation reaction. Molecular oxygen acts like an electron scavenger, removing the electrons on the catalysts surface, regenerating the hydroxide ions and thus closing the catalytic cycle[76].
The rate limiting step of the reaction is the oxidation of the alcoholic group; for this reason, HMF is quickly converted and a high yield of HMFCA could be observed even for low reaction time.

---

[1] P. Gallezot "Process options for the catalytic conversion of renewables into bioproducts"-Catalysis from renewables: from feedstock to energy production *Wiley* (2007).

[2] G. Centi, P. Lanzafane, S. Perathoner *Catal. Today* 167 (2011) 1, 14-30.

[3] F. Carvalheiro, L.C. Duarte, F.M. Girio *J. Sci. Ind. Res*. 67 (2008), 849-864.

[4] J.P.M. Sanders, J.H. Clark, G.J. Harmsen, H.J. Heeres, J.J. Heijnen, S.R.A. Kersten, W.P.M. van Swaaij, J.A. Moulijn *Chem. Eng. Process*. 51 (2012) 117-136.

[5] S. Irmak, M. Kurtulus, A. Hasanoglu, O. Erbatur *Biomass and Bioenergy* 49 (2013) 102-108.

[6] C. He, J. Zheng, K. Wang, H. Lin, J-Y. Wang, Y. Yang *Appl. Catal. B: Environ*. 162 (2015) 401-411.

[7] A. Ciftci, D.A.J.M. Ligthart. E.J.M. Hensen *Green. Chem*. 16 (2014) 853-863.

[8] J.S. Luterbacher, D.M. Alonso, J.A. Dumesic *Green Chem*. 16 (2014) 4816-4838.

[9] F.M. Gírio, C. Fonseca, F. Carvalheiro, L.C. Duarte, S. Marques, R. Bogel-Łukasik, *Bioresour. Technol*. 101 (2010) 4775-4800.

[10] A. Fukuoaka, P.L. Dhepe *Angew. Chemie* 118 (2006) 5285-5287.

[11] J.N. Chheda, G.W. Huber, J.A. Dumesic *Angew. Chem. Int. Ed*. 46 (2007) 7164-7183.

[12] J. Lewkowski *ARKIVOC* i (2001) 17-54.

[13] M. Bicker, J. Hirth, H. Vogel, *Green Chem*. 5 (2003) 280-284.

[14] M.J. Antal, W.S.L. Mok, G.N. Richards, *Carbohydrates Res*. 199 (1990) 91-109.

[15] Y. Roman-Leshkov, G.N. Chheda, J.A. Dumesic *Science* 312 (2006) 1933-1937.

[16] G.N. Chheda, Y. Roman-Leshkov, J.A. Dumesic *Green Chem*. 9 (2007) 342-350.

[17] J.B. Binder, R.T. Raines J. Am. Chem. Soc. 131 (2009) 1979-1985.

[18] X. Tong, Y. Ma, Y. Li Appl. Catal. A: general 385 (2010) 1-13.

[19] I. Agirrezaball-Telleria, I. Gandarias, P.L. Arias *Catal. Today* 234 (2014) 42-58.

[20] I. Delidovich, R. Palkovits *Catal. Sci. Technol*. 4 (2014) 4322-4329.

[21] R. A. Sheldon, *Green Chem*. 16 (2014) 950-963.

[22] A. Corma, S. Iborra, A. Velty, Chem Rev 107 (2007) 2411 -2502.

[23] M. J. Climent, A. Corma, S. Iborra, Green Chem. 16 (2014) 516-547.

[24] T. Werpy, G. Petersen, 2004 Top Value Added Chemicals From Biomass http://www1.eere.energy.gov/bioenergy/pdfs/35523.pdf

[25] F. Yang, Q. Liu, X. Bai, Y. Du, Bioresource Technol 102 (2011) 3424-3429.

[26] R. J. van Putten, J. C. van der Waal, D. De Jong, C. B. Rasrendra, H. J. Heeres, J. G. de Vries, *Chem. Rev*. 113 (2013) 1499-1597.

[27] C. Munoz de Diego, P. Shammel Wayne, A. Dam Matheus, J. M. Gruter Gerardus, WO Patent 2011/043660 (2011) assigned to Furanix Technologies BV.

[28] K. Yutake, T. Toshinari, S. Eritate, T. Komoro, US Patent 2011/092720 (2011) assigned to Canon KK.

[29] A. Shalkh, D. R. Parker, M. E. Janka, L. R. Partin, US Patent 2014/0142328 (2014) assigned to Eastman Chemical Company.

---

[30] O. Casanova, S. Iborra, A. Corma *ChemSusChem* 2 (2009) 1138-1144.

[31] P. Lanzafame, G. Centi, S. Perathoner *Catal. Today* 234 (2014) 2-12.

[32] T. Elhajj, A. Masroua,J.C. Martin, G. Descotes *Bull. Soc. Chim. Fr*. 1987 855.

[33] S.E. Davis, L.R. Houk, E.C. Tamargo, K.. Abhaya, R.J. Davis *Catal. Today* 160 (2011) 55-60.

[34] C. Moreau, R. Durand, C. Pourcheron, D. Tichit *Stud. Surf. Sci. Catal*. 108 (1997) 399-406.

[35] J. Artz, S. Mallmann, R. Palkovits *ChemSusChem* 8 (2015) 672-679.

[36] J. Chen, J. Zhong, Y. Guo, L. Chem *RSC adv*. 5 (2015) 5933-5940.

[37] Y. Wang, B. Liu, K. Huang, Z. Zhang *Ind. Eng. Chem. Res*. 53 (4) (2014) 1313-1319.

[38] J. Nie, H. Liu *J. Catal.* 316 (2014) 57-66.

[39] Y. Y. Gorbanev, S. K. Klitgaard, J. M. Woodley, C. H. Christensen, A. Riisager, *ChemSusChem*, 2 (2009) 672-675.

[40] S. E. Davis, B. N. Zope, R. J. Davis, *Green Chem*. 14 (2012) 143-147

[41] W.C. Ketchie, Y.-L. Fang, M.S. Wong, M. Murayama, R.J. Davis *J. Catal*. 250 (2007) 94-101.

[42] N. Lopez, T.V.W. Janssens, B.S.Clausen, Y. Xu, M. Mavrikakis, T. Bligaard and J.K. Norskov J. Catal. 223 (2004) 232-235.

[43] G.C. Bond, D.T, Thomson *Gold Bull*. 33 (2000) 41-50.

[44] R. Bonelli, C. Lucarelli, T. Pasini, L.F. Liotta, S. Zacchini, S. Albonetti *Appl. Catal. A General* 400 (2011) 54-60.

[45] R. Bonelli, S. Zacchini, S. Albonetti *Catalysts* 2(1) (2012) 1-23.

[46] J.Liu, G. Qin, P. Raveedran, Y. Ikushima *Chem. Eur. J*. 12 (2006) 2131-2138.

[47] C. E. Hoppe, M. Lazzari, I. Blanco, M. Quintela *Langmuir* 22 (2006) 7027-7034.

[48] Y. Xiong, I. Washio, J. Chen, H. Cai, Z. Li, Y. Xia *Langmuir* 22 (2006) 8563-8570.

[49] M. Tsuji, M. Hashimoto, Y. Nishizawa, M. Kubokava, M. Tsuji *Chem. Eur. J*. 11 (2005) 440-452.

[50] A. Lolli, S. Albonetti, L. Utili, R. Amadori, F. Ospitali, C. Lucarelli, F. Cavani *Appl. Catal. A*: *General* (2014) *doi:10.1016/j.apcata.2014.11.020*

[51] T. Pasini, M. Piccinini, M. Blosi, R. Bonelli, S. Albonetti, N. Dimitratos, J. A. Lopez-Sanchez, M. Sankar, Q. He, C. J. Kiely, G. J. Hutchings, F. Cavani, *Green Chem*. 13 (2011) 2091-2099.

[52] A. Villa, M. Schiavoni, S. Campisi, G. M. Veith, L. Prati, *ChemSusChem* 6 (2013) 609-612.

[53] S.E. Habas, H. Lee, V. Radmilovic, G.A. Samorjai, P. Yang *Nature Mater*. 6 (2007) 692-697.

[54] D. Wang, Y. Li *Adv. Mater*. 23 (2011) 1044-1060.

[55] C. Suryanarayana *Prog. Mater. Sci*. 46 (2001) 1-184.

[56] S. Albonetti, T. Pasini, A. Lolli, M. Blosi, M. Piccinini, N. Dimitratos, J. A. Lopez-Sanchez, D. J. Morgan, A. F. Carley, G. J. Hutchings, F. Cavani, *Catal. Today* 195 (2012) 120-126.

[57] S. Liu, A. Wang, T. Zhang, D.S. Su C.Y. Mou *Catal. Today* 160 (2011) 103-108.

[58] X. Wan, C. Zhou, J. Chen, W. Deng, Q. Zhang, Y. Yang, Y. Wang, *ACS Catalysis* 4 (2014) 2175-2185.

[59] A. Villa, D. Wang, D. Su, G. M. Veith, L. Prati, *Phys. Chem. Chem. Phys*. 12 (2010) 2183–2189.

[60] S. Nishimura, N. Ikeda, K. Ebitani, *Catal. Today* 232 (2014) 89–98.

[61] N. Dimitratos, F. Porta, L. Prati, A. Villa, *Catal. Letters* 99 (3-4) (2005) 181-185.

---

[62] N. Dimitratos, F. Porta, L. Prati, *Appl. Catal. A* 291 (2005) 210-214.

[63] N. Dimitratos, A. Villa, D. Wang, F. Porta, D. Su, L. Prati, *J. Catal*. 244 (2006) 113–121.

[64] J. Pritchard, M. Piccinini, R. Tiruvalam, Q. He, N. Dimitratos, J. A. Lopez-Sanchez, D. J. Morgan, A. F. Carley, J K. Edwards, C. J. Kiely, G. J. Hutchings, *Catal. Sci. Technol*. 3 (2013) 308-317.

[65] J. A. Lopez-Sanchez, N. Dimitratos, N. Glanville, L. Kesavan, C. Hammond, J. K. Edwards, A. F. Carley, C. J. Kiely, G. J. Hutchings, *Appl. Catal. A* 391 (2011) 400–406.

[66] A. Villa, M. Schiavoni, S. Campisi, G. M. Veith, L. Prati, *ChemSusChem* 6 (2013) 609-612.

[67] G. J. Hutchings, C. J. Kiely, *Acc. Chem. Res*. 46(8) (2013)1759–1772.

[68] A. A. Herzing, A. F. Carley, J. K. Edwards, G. J. Hutchings, C.J . Kiely, *Chem. Mater*. 20 (2008) 1492-1501.

[69] L. Delannoy, S. Giorgio, J. G. Mattei, C. R. Henry, N. El Kolly, C. Méthivier, C. Louis, *ChemCatChem* 5 (2013) 2707-2716.

[70] C. Bianchi, F. Porta, L. Prati, M. Rossi *Top Catal*. 13 (2000) 231-236.

[71] S. Carretin, P. McMorn, P. Johnston, K. Griffin, C.J. Kiley, G.J. Hutchings *Phys. Chem*. 5 (2003) 1329-1336.

[72] S.K. Klitgaard, A.T. DeLa Riva, S.H. Rebecka, M. Werchmeister, C.H. Christensen *Catal. Lett*. 126 (2008) 213-217.

[73] S.E. Davis, L.R. Houk, E.C. Tamargo, A.K. Datye, R.J. Davis *Catal. Today* 160 (2011) 55-60.

[74] S.E. Davis, B.N. Zope, R.J. Davis *Green Chem*. 14 (2012) 143-147.

[75] B.N. Zope, D.D. Hibbitts, M. Neurock, R.J. Davis *Science* 330 (2010) 74-77.

[76] S.E. Davis, M.S. Ide, R.J. Davis *Green Chem*. 15 (1) (2013) 17-45.

CHAPTER 2

Experimental

2.1 Introduction

The aim of this work is to develop active and stable metal supported catalysts for the oxidation reaction of 5-hydroxymethylfurfural (HMF) into 2,5-furandicarboxylic acid (FDCA) in liquid phase. At first, monometallic (Au, Pd) and bimetallic (AuCu, PdAu) metal nanoparticles with different metal molar ratio and morphology were synthesised, using a basic aqueous phase procedure which requires β-D-glucose as reducing agent and polyvinylpyrrolidone (PVP) as protective agent.

Catalysts were prepared by incipient wetness impregnation of the pre-formed sols; commercial CeO_2 and TiO_2 were used as support together with mesoporous CeO_2 synthesised with the hard template method, where SBA-15 was used as template.

After the impregnation step, catalysts were dried and the effects of the following pre-treatments were investigated:

- Calcination 300°C
- Washing in reaction conditions: in autoclave, water basic solution (0.3 M NaOH), 10 bar O_2, 70°C, 240 min
- Washing in reaction conditions and calcination 300°C

Metal nanoparticles and supported catalysts were characterised using the following techniques:

- ✓ DLS (Dynamic light scattering) to measure the hydrodynamic diameter of the particles
- ✓ XRD (X-Ray Diffraction) to study the type of active phase formed and to evaluate crystallite size

- ✓ HRTEM (High Resolution Transmission Electron Microscopy) to study the type of active phase formed and to evaluate particle size distribution.
- ✓ XRF (X-Ray Fluorescence) to estimate the SiO_2 content in the mesoporous cerium oxide, which remained after the preparation if the template was not completely removed and to verify the metal reduction during nanoparticles synthesis
- ✓ Porosimetry and surface area analysis using the BJH and BET methods
- ✓ TGA (Thermogravimetric Analysis) and DTA (Differential Thermal Analysis) to evaluate the quantity of organic matter, coming from nanoparticles synthesis, on the catalysts surface
- ✓ TPO/R (Temperature Programmed Oxidation/Reduction) to study catalysts redox behaviour.

Every prepared catalyst was used in the oxidation reaction of HMF to FDCA. Products formation was estimated using HPLC analysis. The reaction mixture was also analysed by means of XRF to test catalysts leaching. Au, Pd, PdAu both in form of alloy and in form of core-shell were use unsupported to carry on some catalytic test for the investigation of the reaction mechanism.

2.2 Chemicals and materials

In Table 2-1 are reported all the chemicals and the materials used for catalysts preparation and for catalytic tests.

Compound	Physical State	MW (g/mol)	Purity (%)	Chemical Comapany
Polyvinylpirrolidone (PVP 25K) (C_6H_9NO)$_n$	White powder	114.1	-	Sigma-Aldrich
NaOH	Pellets	40.0	99.00	Sigma-Aldrich
$HAuCl_4 * 3H_2O$	Yellow powder	393.8	99.99	Sigma-Aldrich
$CuSO_4 * 5H_2O$	Light blue powder	249.7	99.50	Carlo Erba
$PdCl_2$	Brown powder	177.3	≥ 99,99	Sigma-Aldrich
D-(+)-glucosio ($C_6H_{12}O_6$)	White powder	180.0	99,90	Fluka
CeO_2 – Ceria 90	White powder	172.1	-	Evonik
CeO_2 – Ceria 60	White powder	172.1	-	Evonik
TiO_2 – DT 51	White powder	79.9	-	Millennium
$Ce(NO_3)_3 * 6 H_2O$	White powder	434.2	> 99,0	Fluka
Ethanol	Colourless liquid	46.0	> 99,80	Sigma-Aldrich
Pluronic 123	Colourless powder	Average M_n 5800	-	Sigma-Aldrich
HCl	Colourless liquid	36.5	37%	Sigma-Aldrich
TEOS	Colourless liquid	208.3	99,99	Sigma-Aldrich
5-hydroxymethylfurfural (HMF)	Yellow powder	126.1	98,00	Alfa Aesar
5-hydroxymehty-2-furancarboxylic acid (HMFCA)	White powder	142.1	99,99	Toronto Research Chemicals
5-formyl-2-furancarboxylic acid (FFCA)	Grey powder	140.1	99,99	Toronto Research Chemicals
2,5-diformylfuran (DFF)	Yellow powder	124.1	99,99	Toronto Research Chemicals
2,5-furandicarboxylic acid (FDCA)	Brown powder	156.1	99,99	Toronto Research Chemicals
2,5-bishydroxymethylfuran (BHMF)	White powder	128.1	99,99	Toronto Research Chemicals

Table 2-1 Chemicals and materials used for the research project.

2.3 Metal nanoparticles synthesis and characterisation

The necessary quantity of polyvinylpyrrolidone (PVP) used as a nanoparticle stabilizer was added to a solution of NaOH in 90 mL of water. The solution was then heated to 95°C with the traditional heating system as showed in Figure 2-1.

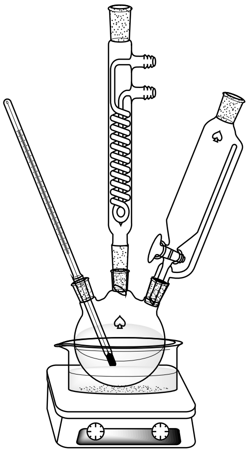

Figure 2-1 Equipment used for nanoparticles synthesis.

At this temperature, β-D-glucose and 10 mL of an aqueous solution containing the metal precursors ($HAuCl_4$, $CuSO_4*5H_2O$, $PdCl_2$) in the desired ratio were added and stirred for 2.5 min. In order to prepare monometallic sols only the salt of the desired metal was added, while for bimetallic alloyed samples both salts were dissolved together (Figure 2-2).

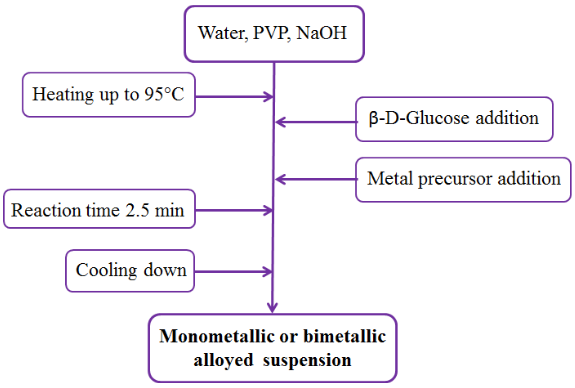

Figure 2-2 Procedure for the synthesis of monometallic and bimetallic alloyed nanoparticles.

On the contrary, for the preparation of core-shell structures Au@Pd (Au core) and Pd@Au (Pd core) the metal precursors were added one after the other. Monometallic nanoparticles have to be prepared and these will be the seed for nucleation of the second metal. In order to favour $PdCl_2$ complete dissolution, some drops of HCl were used.

The procedure is described in diagram below (Figure 2-3).

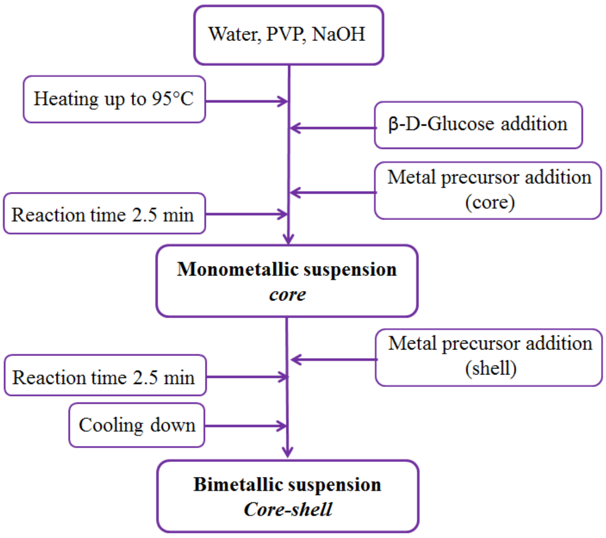

Figure 2-3 Procedure for the synthesis of core-shell nanoparticles.

The metal concentration was fixed at 0.005 M for all the prepared samples. The molar ratio among PVP, β-D-glucose, NaOH, and metals was optimized for each gold and copper content[1,2,3]. Starting from these values it was possible to obtain the right amount of reagents even for sample containing Pd. Glucose and PVP amounts were optimised to obtain small particles with both monometallic and bimetallic sols, thus requiring a significantly higher quantity of PVP and glucose for bimetallic systems to foster particle nucleation instead of particle growth. In Table 2-2 and Table 2-3 the list of the AuCu and PdAu prepared samples is reported together with the optimal reagents/metal molar ratio.

Metal suspensions	mol % [Cu^{2+}]	mol % [Au^{3+}]	[PVP]/ [Cu^{2+}]+[Au^{3+}]	[NaOH]/ [Cu^{2+}]+[Au^{3+}]	[glucose]/ [Cu^{2+}]+[Au^{3+}]
Au	0	100	2.75	8.00	2.00
Au_3Cu_1	75	25	5.81	10.50	4.50
Au_1Cu_1	50	50	8.88	13.00	7.00
Au_1Cu_3	25	75	11.94	15.50	9.50
Cu[3]	100	0	15.00	18.00	12.00

Table 2-2 Molar composition and reagents/metal ratio for each AuCu synthesised suspension.

Metal suspensions	mol % $[Pd^{2+}]$	mol % $[Au^{3+}]$	[PVP]/ $[Pd^{2+}]+[Au^{3+}]$	[NaOH]/ $[Pd^{2+}]+[Au^{3+}]$	[glucose]/ $[Pd^{2+}]+[Au^{3+}]$
Pd	100	0	5.50	8.00	2.00
Pd_3Au_1	75	25	4.81	8.00	2.00
Pd_1Au_1	50	50	4.12	8.00	2.00
Pd_1Au_3	25	75	3.44	8.00	2.00
Pd_1Au_6	14	86	3.14	8.00	2.00
$Au_6@Pd_1$	14	86	3.14	8.00	2.00
$Pd_1@Au_6$	14	86	3.14	8.00	2.00
Pd_1Au_9	10	90	3.02	8.00	2.00
Au	0	100	2.75	8.00	2.00

Table 2-3 Molar composition and reagents/metal ratio for each PdAu synthesised suspension.

Before use, the as-prepared sols were concentrated and washed with distilled water using 50 KDa Amicon Ultra filters (Millipore) to eliminate the excess PVP and other reagents dissolved in the aqueous media. The filtered solution obtained from the concentration step was analysed with XRF to see if there was any traces of cationic metals; thanks to this technique it was possible to calculate the yield of the metal reduction reaction.

2.3.1 Analytical methods

Some characterisation, such as DLS, XRD and HRTEM were carried on the synthesised samples.

DLS analysis

The measurement of the hydrodynamic diameter of the particles was performed with the DLS techniques, using the Zetasizer Nanoseries (Malvern Instruments). From the measure it is possible to obtain a value for the average diameter, the curve of the particle size distribution and the PDI value (Polydispersive Index). The Polydispersive Index gives an idea of how far is the particle size from the medium value. It is usually a number between 0 and 1 and the smaller the number, the more monodisperse is the curve. Before the analysis, samples were diluted in water (10 drops of metal suspension in 10 mL of water).

XRD analysis

XRD analysis were performed on the metal suspension to observe the type of active phase formed and the crystallite size. XRD measurements were carried out at room temperature with a Bragg/Brentano diffractometer (X'pertPro PANalytical) equipped with a fast X’Celerator detector, using a Cu anode as the X-ray source (Kα, λ=1.5418 Å). For AuPd sols, diffractograms were recorded in the range 35-44°2θ, counting for 1000 s every 0.1° 2θ step. This made it possible to evaluate the coherence length of the Pd crystalline domain through a single-line profile fitting of the reflection at 2θ 40.4°, as well as to check the Au characteristic reflection at 2θ 38.2°. Crystallite size values were calculated using the Scherrer equation. The lattice parameter values were calculated from the (111) peak of the face-centred cubic (fcc) nanoparticles. Before the analysis, the sols were deposited dropwise onto a glass sampleholder and dried at 120°C. Several deposition allowed to obtain more concentrated samples.

HRTEM analysis

Nanoparticle suspensions were also examined by high resolution transmission electron microscopy (HR-TEM) using a TEM/STEM FEI TECNAI F20, which uses a high-angle annular dark field (HAADF) imaging mode at 200kV and with an EDS PV9761N SUTW energy dispersive X-ray spectrometer (EDX) for X-ray microanalysis. The suspensions were diluted in water and treated for 30 minutes with ultrasounds. Then, they were dispersed on a holey carbon film.

2.4 Synthesis of mesoporous CeO_2 with the hard template method

Highly ordered mesoporous CeO_2 has been prepared by the hard template method using SBA-15 as a structure-directing agent. Leaching with NaOH and thermal treatment at 500°C allowed the removal of inorganic template, resulting in the formation of long-range ordered CeO_2.

2.4.1 Synthesis and characterization of mesostructured silica SBA-15

Mesoporous silica SBA-15 was prepared under hydrothermal conditions as previously reported by Zhao et al[4]. In a typical synthesis, 4 g of Pluronic 123 were added to 120 g of HCl (2M) and 30 g of bi-distilled water. After 15 h under stirring at 35 °C, 8.5 g of TEOS were added and the solution was maintained at 35 °C for 24 h under stirring. The resulting gel was then transferred into a stainless-steel autoclave and kept at 100 °C for

24 h under static conditions. The obtained suspension was filtered and the recovered solid was washed with distilled water, dried at 40 °C overnight and finally calcined in air at 550 °C for 5.

2.4.2 Synthesis of mesoporous CeO_2

The prepared SBA-15 mesostructured silica was used as template in the synthesis of CeO_2 supports. 7.6 g of $Ce(NO_3)_3 \cdot 6H_2O$ were dissolved in 25 cm^3 of ethanol. 1 g of SBA-15 was then added to 15 cm^3 of the obtained solution and the suspension was stirred at room temperature for 1 h. Next, the solvent was evaporated at 60 °C overnight and the impregnation step was then repeated with the aim of completely filling the SBA-15 pores. The resulting solid was subsequently transferred in a furnace and calcined at 500 °C for 3 h to decompose the nitrates into the corresponding oxides. Removal of the SBA-15 template was then carried out by leaching with a solution (2M) of NaOH at 50 °C. Finally, the resulting material was washed up to pH 7 with distilled water, dried at 60 °C for 12 h and then calcined at 500 °C under static conditions for 3 h. The resulting material was named CeO_2_a. Further CeO_2 supports, named CeO_2_b and CeO_2_c, were also obtained by repeating the leaching process and the following steps of washing, drying and calcination for one or two more times, respectively. In Table 2-4 is reported a list of the prepared supports.

Sample	Number of template removal cycles*
CeO_2_a	1
CeO_2_b	2
CeO_2_c	3

Table 2-4 CeO_2 prepared with different template elimination procedure.

***Each cycle consisted in leaching process and it is followed by steps of washing, drying and calcination.**

2.5 Supported catalyst preparation and characterisation

All catalysts were prepared by the immobilization of preformed monometallic and bimetallic colloids on CeO_2 (VP AdNano 90 and VP AdNano 60, Evonik), mesoporous CeO_2 prepared with the hard template method and TiO_2 (DT51 Millennium Chemicals) surfaces. For all the samples, the impregnation solvent was evaporated by thermal treatment at 120°C. Some samples were calcined at 300°C and washed in reaction conditions. The total metal loading was maintained at 1.5 wt% for each catalyst. For bimetallic catalysts the Au:Cu ratio varied from 1:0 to 1:3 on a molar basis, while Pd:Au ratio varied from 1:0 to 0:1. In Table 2-5 are listed all the catalysts prepared using commercial supports and mesoposous CeO_2.

Catalysts	**Metal suspensions**	**Support**	**wt % Cu or Pd**	**wt % Au**
Au-CeO_2	Au	CeO_2 Evonik	0	1.5
Au_3Cu_1-CeO_2	Au_3Cu_1		1.34	0.16
Au_1Cu_1-CeO_2	Au_1Cu_1		1.14	0.36
Au_1Cu_3-CeO_2	Au_1Cu_3		0.76	0.74
Au-CeO_2_a	Au	CeO_2_a	0	1.5
Au-CeO_2_b	Au	CeO_2_b		
Pd-TiO_2	Pd	TiO_2 Millennium	1.5	0
Pd_3Au_1-TiO_2	Pd_3Au_1		0.93	0.57
Pd_1Au_1-TiO_2	Pd_1Au_1		0.53	0.97
Pd_1Au_3-TiO_2	Pd_1Au_3		0.23	1.27
Pd_1Au_6-TiO_2	Pd_1Au_6		0.12	1.38
Pd_1Au_9-TiO_2	Pd_1Au_9		0.08	1.42
Au-TiO_2	Au		0	1.5
Au_3Cu_1-TiO_2	Au_3Cu_1		1.34	0.16
Au_1Cu_1-TiO_2	Au_1Cu_1		1.14	0.36
Au_1Cu_3-TiO_2	Au_1Cu_3		0.76	0.74

Table 2-5 List of prepared catalysts.

2.5.1 Analytical methods

Mesoporous supports and catalysts were characterized in detail by BET analysis, XRD, HR-TEM, TGA, and TPO/TPR. Mesoporous supports were characterised by porosimetry (BJH method) and XRF, XRD.

BET analysis and porosimetry

Catalyst surface areas were measured by N_2 physisorption apparatus (Sorpty 1750 CE instruments) and the single-point BET analysis method, in which samples were pre-treated under vacuum conditions at 120°C.

Textural analysis was carried out with an ASAP 2020 analyzer (Micromeritics) by determining the nitrogen adsorption/desorption isotherms at -196 °C. Before analysis, samples were heated overnight under vacuum up to 250 °C (heating rate, 1 °C min^{-1}).

XRF analysis

XRF analysis on the mesoporous support were carried on to verify the amount of silica residual using a Panalytical Axios Advanced X-Ray Fluorescence Diffractometer equipped with a Rh anode as the X-ray source. The measurements were performed under vacuum. Sample were grinded and mixed with an organic wax (300 mg sample, 100 mg wax) before being pelletized.

XRD analysis

XRD measurements were carried out at room temperature with a Bragg/Brentano diffractometer (X'pertPro PANalytical) equipped with a fast X'Celerator detector, using a Cu anode as the X-ray source (Kα, λ=1.5418 Å). All catalysts were analyzed in the region of 10-80° 2θ, counting for 20 sec at each 0.05° step. However, for the evaluation of the metal crystallite size for the CeO_2 supported catalysts, a second acquisition was performed in the 2θ range 36-46°, counting for 400 sec at each 0.03 step. In fact, the coherence length of the Au crystalline domains was evaluated through the single-line profile fitting of the reflection at 2θ 38.2°. Crystallite size values were calculated using the Scherrer equation from the full width at half maximum intensity measurements. On the contrary, for the evaluation of the metal crystallite size of Pd-TiO_2 containing sample, a second acquisition was performed in the 40-46° 2θ range, counting for 1500 s at each 0.08° 2θ step. For catalysts with a high Au content, crystallite size values were calculated using the Au reflection peak at 2θ 44.3°. It was not possible to calculate crystallite sizes on the main Pd reflection peaks (2θ 40.3 and 46.9°) because of the presence of anatase peaks in the same position.

Mesoporous cerium oxides were analysed in the 2θ region 20-65°, counting for 20 s at each 0.05° step. Small angle XRD analysis was performed on a Seifert X3000 diffractometer with a θ-θ Bragg-Brentano geometry with Cu-Kα wavelength (λ=1.5418 Å). Samples were analyzed in the 0.8°-2.5° 2θ range, counting for 20 s at each 0.01° step.

HRTEM analysis

Transmission Electron Microscopy (TEM) observations were made using a FEI Tecnai F20 TEM equipped with a Schottky emitter and operating at 200 keV. The instrument is equipped with a Fischione High Angle Annular Dark Field Detector (HAADF) for Scanning Transmission Electron Microscopy (STEM) investigations and with an Energy Dispersive X-Ray Spectrometer (EDX) for X-rays microanalysis. Samples were ground in a mortar and treated with ultrasounds in isopropyl alcohol. A droplet of the resulting finely dispersed suspension was evaporated at room temperature and under atmospheric pressure on a holey carbon film.

Thermal analysis (TGA/DTA)

To verify the behaviour of different samples under thermogravimetric analysis, TGA was obtained using a TA SDT Q 600 analyser while heating the sample in air (100 mL/min) from 25°C to 600°C with a speed of 10°C/min.

TPR/TPO analysis

The oxidation behaviour of different samples was studied via Temperature Programmed Oxidation using a Thermoquest TPDRO instrument under 5% O_2/He or 5% H_2/Ar flow (20 ml/min). The temperature was raised from 60 to 650°C with a heating rate of 10°C/min followed by an isothermal step at 650°C for 30 min. CeO_2 based samples were pre-treated in oxidising conditions 5% O_2/He for 30 min at temperature of which it has been treated (120°C for the dried and 300°C for the calcined).

2.6 Catalytic tests

The oxidation of HMF was carried out using an autoclave reactor of 100 mL capacity, equipped with a mechanical stirrer (0–600 rpm) and measurement tools for temperature and pressure. The reactor was charged with an aqueous solution (25 mL distilled water) containing the appropriate amount of 5-hydroxymethylfurfural, base (NaOH) and catalyst (HMF/metal molar ratio = 100). NaOH sodium hydroxide was always loaded in excess with respect to HMF (HMF/NaOH 1:4 for Au and AuCu samples, HMF/NaOH 1:2 for Pd and PdAu samples). The autoclave was purged 3 times with O_2 (5 bar) and then pressurized at 10 bar. The temperature was generally increased to 70ºC and the reaction mixture was stirred at approximately 400 rpm for 4 h. However, NaOH content and different temperatures were studied and optimised for each catalyst. Initial time (time zero) for the reaction was taken when the set point temperature was reached (after 15 min of heating). At the end of the reaction, the reactor was cooled down to room temperature.

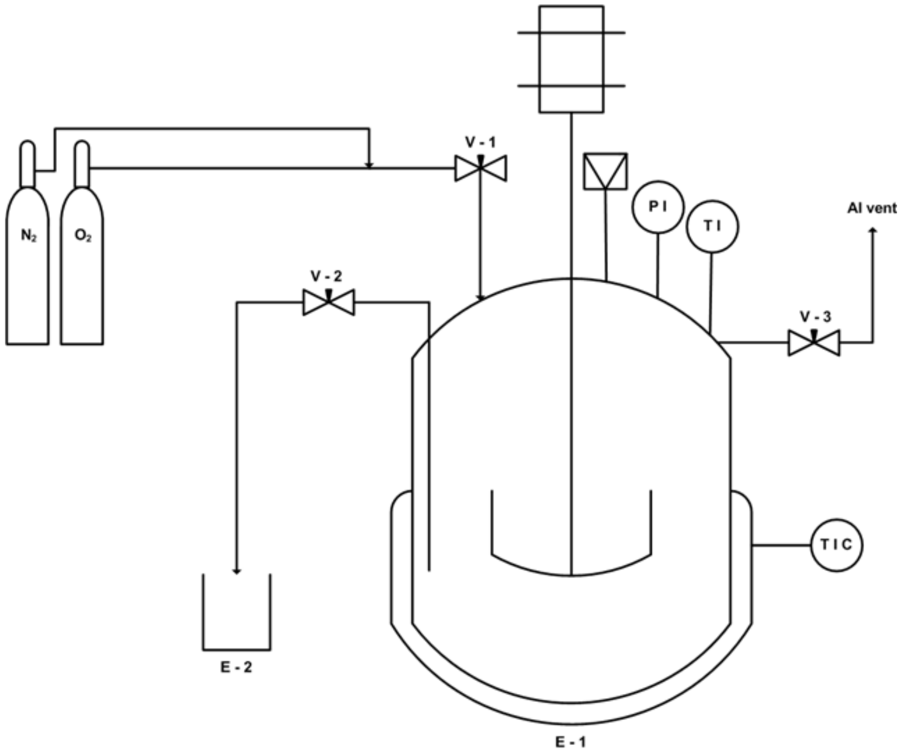

Figure 2-4 Simplified representation of the autoclave.

2.6.1 Analytical method

At the end of the catalytic test, the solution was filtered. When the nanoparticles were used unsupported, they have been separated using the Millipore UltraCell filter of 30 kDa for the core-shell sols and the 50 kDa for all the others. The latter were centrifuged at 1100 turns/min for 30 minutes. This procedure was repeated four times, adding water each time to the filter in order to wash it, avoiding the possibility of having some products trapped on it. Then, 4 mL of water were added to an aliquot of the reaction solution (1 mL) before analysis with an Agilent Infinity 1260 liquid chromatograph equipped with a DAD detector and an Aminex HPX-87H 300 x 7.8 mm column using a 0.005 M H_2SO_4 solution as mobile phase. The compound identification was achieved by calibration using reference commercial samples. Each sample is detected at its own maximum absorbance wavelength, as indicated in Table 2-6.

Compound	Wavelength (nm)
HMF	284
DFF	284
FFCA	284
HMFCA	251
FDCA	264
BHMF	223

Table 2-6 Maximum absorbance wavelength for the calibrated compound.

Below typical chromatograms are reported (Figure 2-5), where each compound has its own retention time with the exception of FDCA and BHMF.

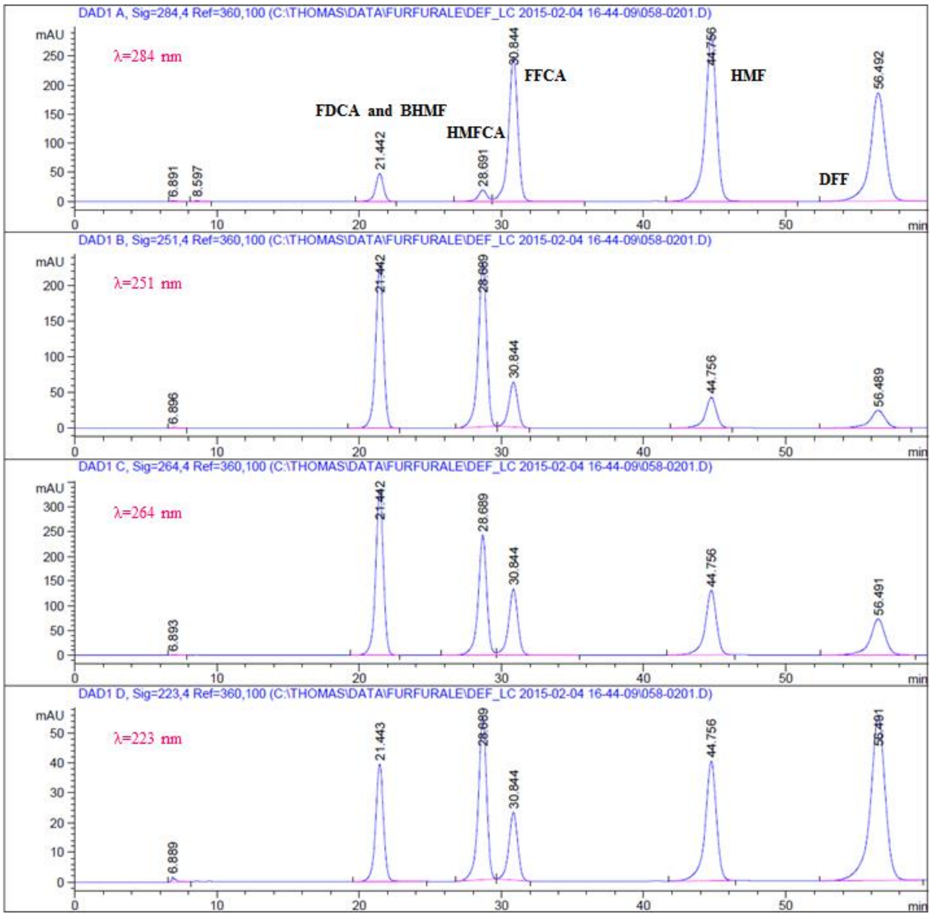

Figure 2-5 Typical chromatograms displaying the retention time of the compounds and the wavelength at which they are acquired.

These two compounds have the same retention time (21 minutes); fortunately they have different maximum adsorbance as showed in Table 2-6 and BHMF do not absorb at 264 nm. This means that, having a DAD detector it is possible to acquire at the same time both analytes at different wavelengths.

---

[1] M. Blosi, S. Albonetti, G. Baldi, F. Gatti, M. Dondi, *Dyes Pigments* 94 (2) (2012) 355-362.

[2] S. Albonetti, M. Blosi, F. Gatti, A. Migliori, L. Ortolani, V. Morandi , G. Baldi, M. Dondi *Stud. Surf. Sci. Catal*. 175 (2010) 621-624.

[3] M. Blosi, S. Albonetti, S. Ortelli, A. L. Costa, L. Ortolani, M. Dondi, *New J. Chem*. 38 (2014) 1401-1409.

[4] D. Zhao, Q. Huo, J. Feng, B.F. Chmelka, G.D. Stucky J. Am. Chem. Soc 120 (1998) 6024-6036.

CHAPTER 3

Conversion of 5-hydroxymethylfurfural to 2,5-furandicarboxylic acid over Au-based catalysts: optimisation of active phase and metal-support interaction.

This chapter was previously published as *S. Albonetti, A. Lolli, V. Morandi, A. Migliori, C. Lucarelli, F. Cavani "Conversion of 5-hydroxymethylfurfural to 2,5-furandicarboxylicacid over Au-based catalysts: Optimization of active phase and metal–support interaction" Appl. Catal B 163 (2015) 520–530.*

3.1 Introduction

In the present part of the work, a series of Au and Au-Cu-containing catalysts based on different carriers such as TiO_2 and CeO_2 were studied in order to increase the activity and selectivity in 5-hydroxymethylfurfural oxidation, optimizing the interaction both between the metals and with the support. The results obtained demonstrated the high activity in HMF oxidation of monometallic gold supported on ceria and titania. Nevertheless, although gold particle size on both supports was comparable, Au/CeO_2 showed significantly higher activity than Au/TiO_2, thus corroborating the theory that not only the gold particle size, but also the support, plays a key role in aqueous phase HMF oxidation. Indeed, pre-made uniform nanoparticles, used for catalyst preparation, were surface-bounded by poly(N-vinyl-2-pyrrolidone) (PVP)– the stabilizer used during nanoparticle synthesis – whose presence was proved to prevent the interaction of active phases with CeO_2, worsening the catalytic activity of both monometallic and bimetallic systems. The pre-treatment of the prepared catalysts was necessary to activate the materials, by maximizing the contact between the metal and the support and thus suggesting an important role of ceria defects on 5-hydroxymethylfurfural oxidation (HMF) to 2,5-furandicarboxylic acid (FDCA).

3.2 Catalyst characterisation

The surface area and average Au crystal size for the prepared catalysts are listed in Table 3-1.

Catalyst	Total metal loading (% wt.)	Gold content (% wt.)	Copper content (% wt.)	Surface Area (m^2/g)	Au crystallite size (nm)*
CeO_2	-	-	-	89	-
Au-Ce	1.5	1.5	-	85	6.0
Au_3Cu_1-Ce	1.5	1.34	0.16	62	5.0
Au_1Cu_1-Ce	1.5	1.14	0.36	53	5.0
Au_1Cu_3-Ce	1.5	0.76	0.74	49	5.0
TiO_2	-	-	-	83	-
Au-Ti	1.5	1.5	-	74	6.5
Au_3Cu_1-Ti	1.5	1.34	0.16	72	5.0
Au_1Cu_1-Ti	1.5	1.14	0.36	64	5.0
Au_1Cu_3-Ti	1.5	0.76	0.74	60	5.0

Table 3-1 Structural parameters and chemical composition of Au and Au-Cu supported on CeO_2 and TiO_2. Legend:* estimated from XRD

Surface areas similar to supports were obtained in the case of gold supported on TiO_2 and CeO_2, thus indicating that gold nanoparticle deposition did not lead to a significant change in the texture of supporting materials. Conversely, the impregnation with bimetallic Au/Cu sols indicated that the deposition somewhat affects the textural properties of ceria and titania, while samples with the highest Cu/Au metal ratio showed a significant reduction in the surface area. This is probably due to the presence of a higher organic content in bimetallic systems. As a matter of fact, the organic layer surrounding metal nanoparticles may occlude the oxide porosity, thus leading to a decrease in the surface area. To confirm this hypothesis, the as-synthesized materials were characterized by Thermogravimetric Analysis (TGA) and Differential Thermal Analysis (DTA) (Figure 3-1A and Figure 3-1B). The TGA curves of the as-synthesized ceria-supported samples (Figure 3-1A) show two distinct weight losses; i) a lower weight loss between 50 and 150°C, due to the physically adsorbed water, and ii) a higher weight loss, in the temperature range of 200–300°C, which is associated with an exothermal process (Figure 3-1B) ascribable to the burning-off of the adsorbed poly(N-vinyl-2-pyrrolidone) (PVP) in the sample. Indeed, the decomposition of PVP has been reported to occur at higher temperatures (400-600°C) in the absence of active metals[1,2], but between 200°C and 450°C in the presence of noble metals such as Pt[3].

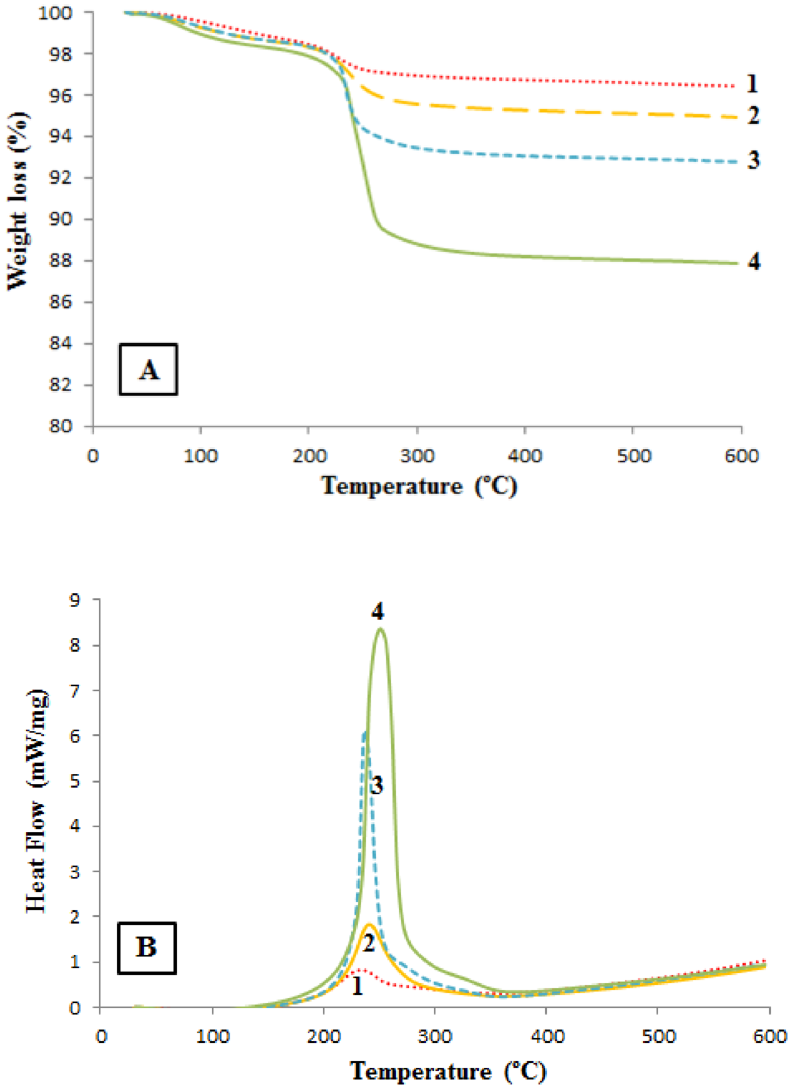

Figure 3-1 Thermogravimetric analysis (A) and differential thermal analysis (B) in air of CeO_2-supported catalysts with different Au:Cu atomic ratios. Legend: (1) Au-Ce; (2) Au_3Cu_1-Ce; (3) Au_1Cu_1-Ce; (4) Au_1Cu_3-Ce.

The observed catalyst's weight loss in TG analysis increased from approximately 2 wt.% to 10 wt.% by increasing the Cu content in the materials (Table 3-2).

Catalyst	T (°C)	Weight loss (%)
Au-Ce	236	1.9
Au_3Cu_1-Ce	240	3.1
Au_1Cu_1-Ce	236	5.4
Au_1Cu_3-Ce	250	9.7
Au-Ti	312	2.0
Au_3Cu_1-Ti	310	3.5
Au_1Cu_1-Ti	320	5.5
Au_1Cu_3-Ti	301	9.8

Table 3-2 Weight loss and PVP decomposition temperature of the Au and Au-Cu supported on CeO_2 and TiO_2.

During metal sol preparation, the weight ratios of PVP to total metals varied from 2.8 to 12, while the metal loading was always equal to 1.5 wt. %; therefore, the observed increase in the weight loss may be attributed mainly to the highest amount of PVP present over samples with the highest copper content. These results are confirmed by the comparison of the weight loss observed for TiO_2-supported materials (Table 3-2) prepared using the same preformed sols[4], which show exactly the same trend. In addition, the exothermicity associated with the PVP decomposition significantly increased by increasing the Cu content in the active phase (Figure 3-1B); this trend explains the decrease observed in the surface area of the catalysts with high copper content. Moreover, the data in this table show that the temperature of PVP combustion depends on the support, thus indicating that ceria promotes PVP decomposition.

Figure 3-2 shows XRD patterns for gold and gold/copper catalysts at different metal ratios. This analysis revealed the presence of diffraction peaks related to the CeO_2 phase in the cubic crystal structure of fluorite-type, while no peaks related to gold species were evidenced using standard XRD acquisition procedures, thus suggesting that very small gold and gold/copper nanoparticles were formed: a fact which is consistent with the previous findings[5]. However, when a more accurate XRD acquisition was used, a small broad peak at about 38.2° 2θ was evidenced, which was attributed to metallic gold and/or the Au/Cu alloy. The average diameters of the metallic particles, estimated from this peak by Scherrer's equation, are given in Table 3-1. Very small Au particles were obtained in all samples.

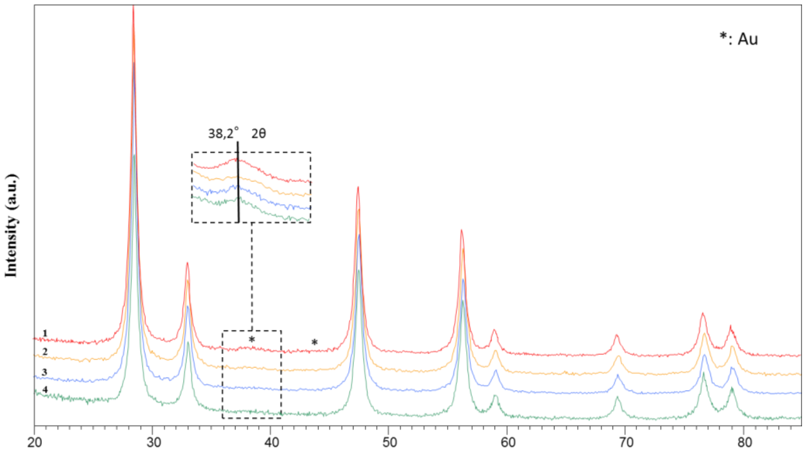

Figure 3-2 XRD patterns of CeO_2-supported catalysts with different Au:Cu atomic ratios. 1) Au-Ce; 2) Au_3Cu_1-Ce; 3) Au_1Cu_1-Ce; 4) Au_1Cu_3-Ce. In the insert: magnification of the reflection at 2θ 38,2° which was used to evaluate the Au crystal size.

Gold and gold/copper species over CeO_2 were investigated using high-resolution TEM imaging. Figure 3-3A and Figure 3-3B show some representative TEM images of the Au- and Au/Cu-supported catalysts and the corresponding size distribution histograms. Dispersed agglomerates include ceria particles with a mean diameter of 10-15 nm.

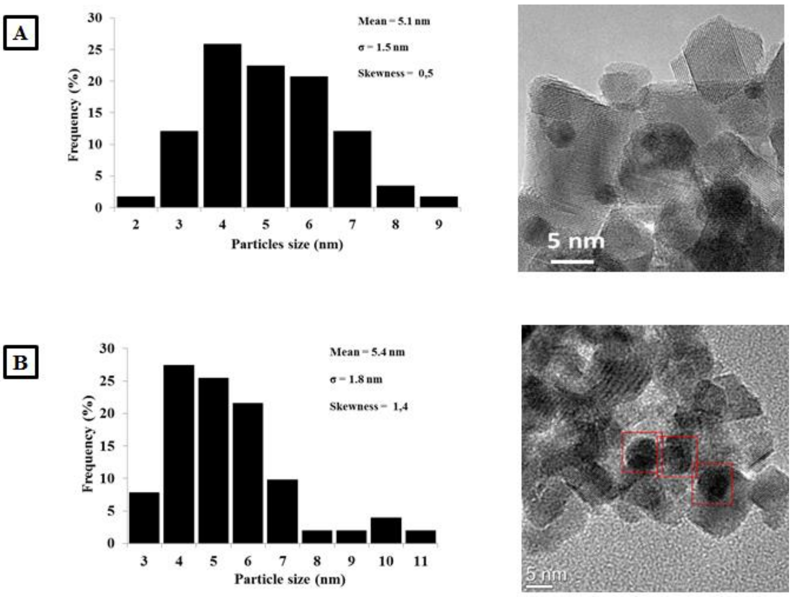

Figure 3-3 Representative TEM images of the Au- and Au/Cu-supported catalysts. (A) Au-Ce sample dried at 120°C and (B) Au_3Cu_1-Ce sample dried at 120°C.

Gold and gold/copper nanoparticles are embedded in the ceria network. This study reveals a significant homogeneity in the size distribution of Au and Au/Cu particles supported on TiO_2 and CeO_2. Both metals are in close contact with the supports, and dark field images (not shown) confirm that the metallic nanoparticles are evenly distributed. Au and Au/Cu nanoparticles are present in an almost spherical shape with very narrow diameter distribution (5-6 nm), thus confirming the results obtained from XRD.

3.3 Catalytic tests

3.3.1 HMF conversion in blank experiments

Preliminary experiments have been devoted to blank tests, by reacting HMF in an aqueous solution with HMF:NaOH ratio of 1:4, at 70°C and ambient pressure, both under air and under N_2, in the absence of any catalytic system (Figure 3-4).

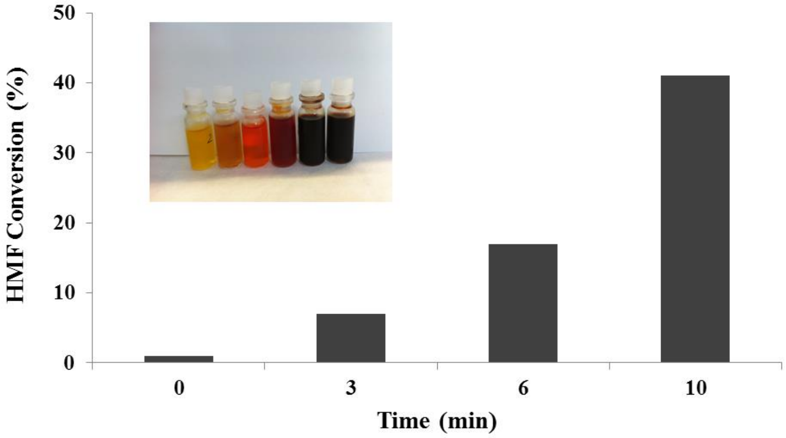

Figure 3-4 Effect of reaction time on HMF degradation. Reaction conditions: no catalyst, no O_2 pressure, temperature 70°C, ambient pressure, HMF:NaOH 1:4 molar ratio.

These experiments made it possible to verify that no oxidation occurred under these conditions; however, as already reported in our previous work[6] and in the recent Vuyyuru paper[7], a significant amount of 5-hydroxymethylfurfural was degraded in these basic conditions. Figure 3-4 shows 40% of HMF conversion at 70°C already after 10 minutes, without the formation of any detectable oxidation products. The reaction mixture turned from colorless to yellow and then to red with the reaction time. After 30 minutes, HMF was totally converted and the solution became brownish. The formed degradation products were soluble in water at high pH (pH= 13), but they were insoluble in acidic conditions. In fact, when some drops of HCl were added, the formation of a black precipitate was observed. In these reaction conditions, aldol condensation should not be possible due to the absence of species with alpha hydrogen; therefore, the mechanism should be different from that obtained in acidic conditions[8]. However, even if these degradation products are formed with a different reaction pathway, they behave like humins, which are formed in acidic conditions. Indeed, Piccolo et al.[9] have treated some organic matter in basic conditions by using NaOH and obtained the precipitation of some humic acids by lowering the pH with HCl to the value of 1.

Generally speaking, humins have coiled conformations which are cross-linked by weak forces such as Van der Waals bonds, but when the pH is lowered, both the formation of intermolecular hydrogen bonds and the rearrangement of the conformation are observed. It is probable that the HMF degradation products, obtained in basic conditions, are similar to humins and are arranged in coil conformations; at low pH values, however, these aggregates become insoluble in water and tend to precipitate, due to their rearrangement.

Scientific literature extensively reports the positive effects of the addition of homogeneous bases on the performance of HMF oxidation. In reality, the rate of HMF oxidation depends significantly on the presence of NaOH, and the base seems to promote the formation of 5-hydroxymethyl-2-furancarboxylic acid (HMFCA), which can be further oxidized by the metal catalyst[10]. However, in the absence of an active catalyst, the basic environment leads to the formation of by-products that cannot be easily identified. Therefore, it is important to develop active catalysts that rapidly oxidize HMF and intermediate products, thus avoiding their fast degradation in reaction conditions.

3.3.2 As-prepared samples: effect of the active phase composition

It has been reported that the oxidation of HMF to FDCA over gold-based catalysts comprises two steps: i) the aldehyde oxidation to form HMFCA, and ii) the oxidation of alcohol to FDCA, through the formation of 5-formyl-2-furancarboxylic acid (FFCA) as the intermediate (Scheme 3-1)[11,12,13,14].

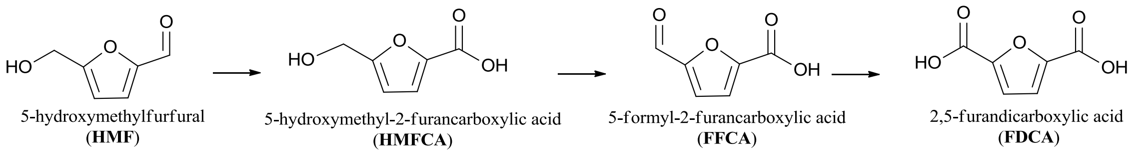

Scheme 3-1 The reaction scheme in HMF oxidation to FDCA.

According to previous works, the formation of HMFCA via the hemiacetal[15] is a very fast reaction and is strongly influenced by the amount of base and reaction temperature, while the subsequent transformation of the HMF hydroxyl group is the rate-limiting step[14]. Furthermore, the formation of 2,5diformylfuran (DFF) has sometimes been observed, mainly in the absence of a base and with metals other than gold[16].

Firstly, the effect of Au:Cu ratios over CeO_2-supported materials was studied, for a total metal loading of 1.5% wt. (Figure 3-5). Results indicate that pure ceria support is inactive in the oxidation, forming very small amounts of HMFCA and by-products derived from HMF degradation. Conversely, the oxidation of HMF over Au and Au/Cu samples resulted in the formation of both HMFCA and FDCA. FFCA was observed only in low reaction time tests, whereas DFF was never formed.

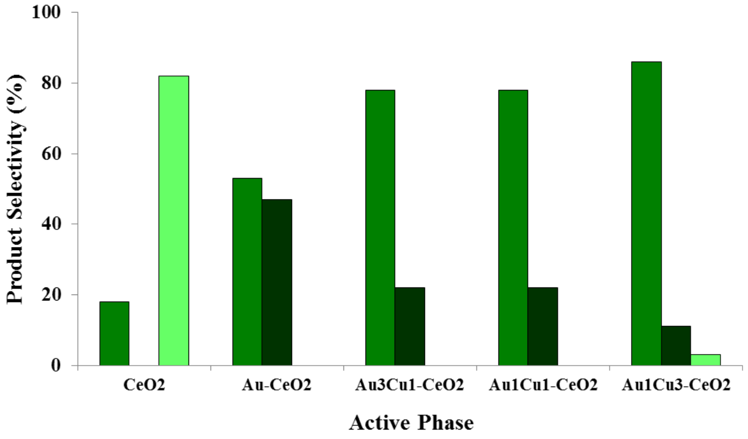

Figure 3-5 Product selectivity on CeO_2-supported catalysts at different Au:Cu atomic ratios. Results are given at total conversion of HMF. Reaction conditions: temperature 70°C, reaction time 240 min, O_2 pressure 10 bar, HMF:Metal:NaOH molar ratio 1:0.01:4. Legend: 🟩HMFCA, ■FDCA, 🟩by-products.

For all samples, after the 4 h reaction HMF conversion was always complete, but considerable differences were seen among catalysts in terms of product selectivity. In particular, the selectivity toward FDCA decreased significantly for Cu-containing samples as compared to monometallic catalyst, due to the slower oxidation of HMFCA. TOF data – calculated as moles of formed FDCA produced referred to reaction time (4h) and Au moles – turned out to be equal to 12.9 h^{-1}, 7.4 h^{-1} and 11.4 h^{-1} for Au-Ce, Au_3Cu_1-Ce, and Au_1Cu_1-Ce, respectively.

These results are very different from those observed with titania-supported materials[6], where the presence of Cu in the active phase led to a considerable increase in catalytic performance as compared to Au-based materials. In particular, the comparison of the effect of Cu content using TiO_2 and CeO_2 supports (Figure 3-6) indicates that the monometallic Au-Ce sample was the most active ceria-supported catalyst, while for titania-supported materials higher activity was observed with bimetallic systems. Indeed, the use of a CeO_2 support seems to depress the positive effect of Cu, observed in the case of TiO_2-supported catalysts.

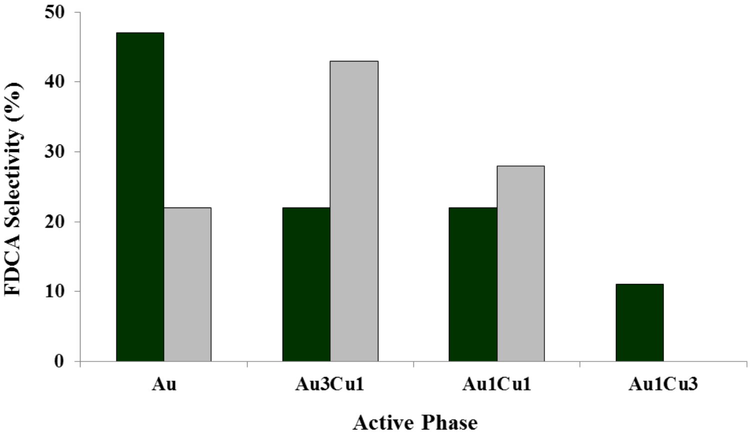

Figure 3-6 Comparison of FDCA selectivity on CeO_2- and TiO_2-supported catalysts at different Au:Cu atomic ratios. Results are given at total conversion of HMF. The only products observed were FDCA and HMFCA. Reaction conditions: temperature 70°C, reaction time 240 min, O_2 pressure 10 bar , HMF:Metal:NaOH molar ratio 1:0.01:4. Legend: ■CeO_2 ■TiO_2.

To discuss the reasons for the different behavior shown by CeO_2 and TiO_2, it must be reported that Au supported on ceria is very active in the oxidation of a variety of molecules[17,18]. In general, CeO_2 is known as an excellent redox support owing to its superior physicochemical properties as compared to conventional supports, due to the high number of oxygen vacancies and the easy Ce^{4+}/Ce^{3+} redox transition, with both significant oxygen mobility and storage capacity. Corma and co-workers showed that Au/CeO_2, especially in catalysts with nanocrystalline CeO_2 support, is particularly effective for the oxidation of alcohols to the corresponding aldehyde[19]. These catalysts were shown to be more active than the supported Pd catalysts available at that time[20]. Corma and Iborra[14] later showed that a similar catalyst was effective for the oxidation of HMF but reusable only to a limited extent.

The role of the CeO_2 support in gas phase reactions was reported to be correlated to its capacity either to facilitate oxygen transfer to the metal in order to stabilize cationic Au, or to activate molecular oxygen[21]. Moreover, several works[22,23,24,25,26] have demonstrated that all these events, i.e., oxygen mobility, activation of O_2, and cationic Au formation system are strongly dependent on Au-CeO_2 interfacial interaction.

In this work, the synthesis of Cu-containing nanoparticles required a considerable quantity of capping agent to control the growth of particles during preparation; this led to significantly larger amounts of organics around Cu-containing nanometals, which may prevent the proper interaction between the active phase and CeO_2, thus influencing the reactivity. As a matter of fact, the comparison of TPO profiles for monometallic and bimetallic samples (Figure 3-7) indicates that the bimetallic catalyst contains a significantly higher quantity of organics than the monometallic one.

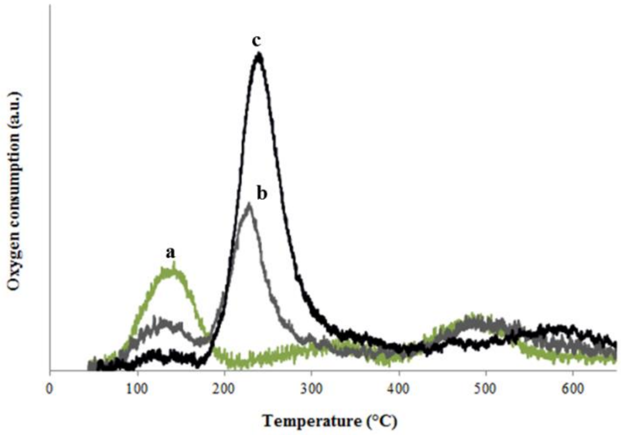

Figure 3-7 TPO analysis of CeO_2 as is (a), Au-Ce (b) and Au_3Cu_1-Ce (c) -supported catalysts.

This is also confirmed by TG analysis, with the main combustion step shown at 230-240°C, while the first small peak at 150°C is ascribable to the desorption of CO_2 from the sample. This last signal is also present in the analysis of the CeO_2 support alone.

Due to the above-mentioned phenomena, and because a proper interaction between the active phase and the support appears to be necessary in order to maximize the efficiency of these catalysts, we concluded that the greater amount of capping agent in Au/Cu bimetallic systems might be detrimental for the catalytic activity, being responsible in the end for the significant differences seen between TiO_2- and CeO_2-based systems. Indeed, the nanoparticle size effect on the activity could be ruled out because the size of the preformed nanoparticles was very similar for all catalysts regardless of the type of support, as demonstrated by XRD and TEM analysis.

In conclusion, the activity of TiO_2-supported catalysts seems to be more influenced by the nature of the nanoparticle species. Conversely, the activity of CeO_2-supported systems is mainly influenced by the interaction between Au and ceria; in this case, bimetallic nanoparticles were less active.

3.3.3 As-prepared samples: effect of reaction temperature and time

Catalytic experiments were also performed with the Au_3Cu_1-Ce catalyst by varying the reaction temperature (Figure 3-8), while the activity was compared with the performance shown with the TiO_2 supported system containing the same active phase. A strong effect of temperature was observed on product distribution. The results obtained confirmed that the studied catalysts display a very high activity for the oxidation of the aldehydic functionality of HMF, forming a high quantity of HMFCA at low temperature also. Nevertheless, the oxidation of the primary alcohol side chain, which is necessary to form FDCA via intermediate (FFCA), is more demanding and proceeds at a significant rate at temperatures higher than 80°C. In both catalysts, after a 4-hour reaction at 95°C, a selectivity of FDCA higher than 90% was achieved. By-products were not detected under the reported conditions and HMF was exclusively oxidized to HMFCA and then to FDCA.

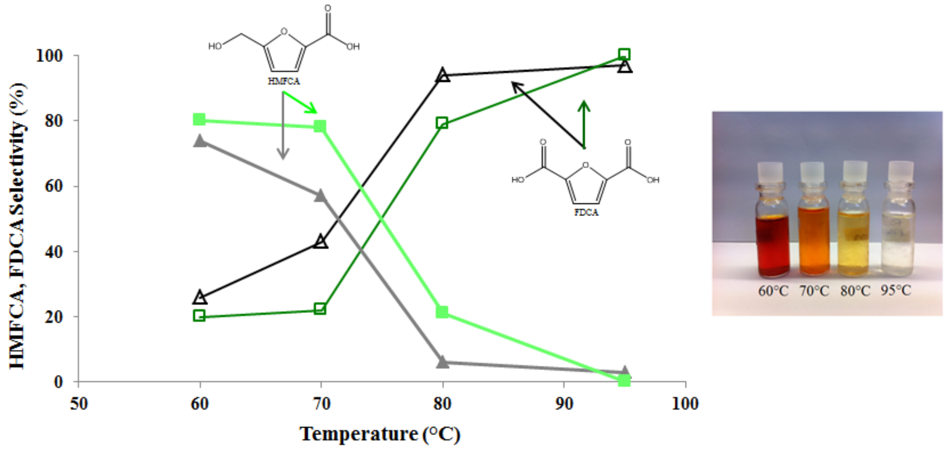

Figure 3-8 HMFCA (closed symbols) and FDCA (open symbols) selectivity as a function of reaction temperature for Au_3Cu_1-Ce (■,□) and Au_3Cu_1-Ti (▲,△) catalysts. Results are given at total conversion of HMF. The only products observed were FDCA and HMFCA. Reaction conditions: reaction time, 240 min, O_2 pressure 10 bar, HMF:Metal:NaOH molar ratio 1:0.01:4. The insert shows the final mixture after reaction at different temperatures with Au_3Cu_1-Ti.

A typical profile of products is shown in Figure 9, where HMF conversion and selectivities are plotted as a function of reaction time with the Au-Ce catalyst, at 95°C.

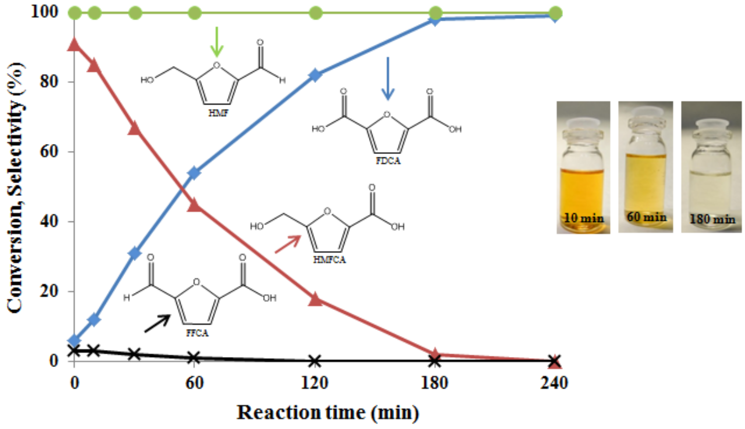

Figure 3-9 HMF conversion and product selectivity as a function of reaction time. Catalyst Au-Ce. Reaction conditions: temperature 95°C, O_2 pressure 10 bar, HMF:Metal:NaOH molar ratio 1:0.01:4. Legend: HMF conversion (●), HMFCA selectivity (▲), FFCA selectivity (×), FDCA selectivity (♦). Initial time (time zero) for the reaction is when the temperature of 95°C was reached (after 15 min heating from a.t). The insert shows the final mixture after reaction at different times.

In these conditions, the complete conversion of HMF was obtained as soon as the reaction mixture reached the temperature of 95°C. Since neither HMFCA nor 2,5-

dihydroxymethylfurfural was formed in the absence of a catalyst, the presence of the Cannizzaro reaction may be ruled out[27]. A very low amount of FFCA was seen during the initial stage of the reaction, but it rapidly converted into FDCA. Indeed, the rate-determining step for FDCA production is the oxidation of the HMF hydroxymethyl group[14]. Other by-products (e.g. DFF) were not formed, and after 4-hr reaction a very pure FDCA solution was obtained (Figure 3-10).

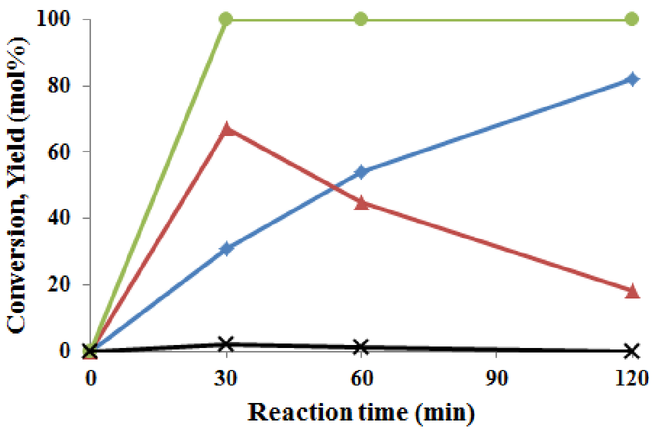

Figure 3-10 Time course of product distribution. Legend: HMF conversion (●), FDCA yield (♦), HMFCA yield (▲), FFCA yield (×).

3.3.4 Catalyst stability and reusability

Since catalysts based on supported Au were reported to lose activity quickly, due to Au leaching and/or active phase blocking by competitive adsorption, the stability of the Au/CeO_2 and Au-Cu/CeO_2 catalysts was carefully studied. Figure 3-11 and Figure 3-12 show the results of the reusability studies using Au-Ce (Figure 3-11) and Au_3Cu_1-Ce (Figure 3-12). Unexpectedly, both monometallic and bimetallic catalysts showed a rapid increase in activity after repeated catalytic tests. Similar trends were not observed in the case of TiO_2-supported materials[6,5]. In fact, in our previous papers we reported that with monometallic TiO_2-supported catalysts a rapid decline in activity was seen, while bimetallic Au/Cu materials were highly stable and resistant to poisoning. Since metal leaching during HMF oxidation was excluded by chemical analysis (XRF analysis revealed that no Au, Cu, or Ce species were dissolved in the reaction mixture), the unusual activation effect seen may be attributable to a modification of the interaction between the surface of the nanoparticles and CeO_2 during the reactivity experiments.

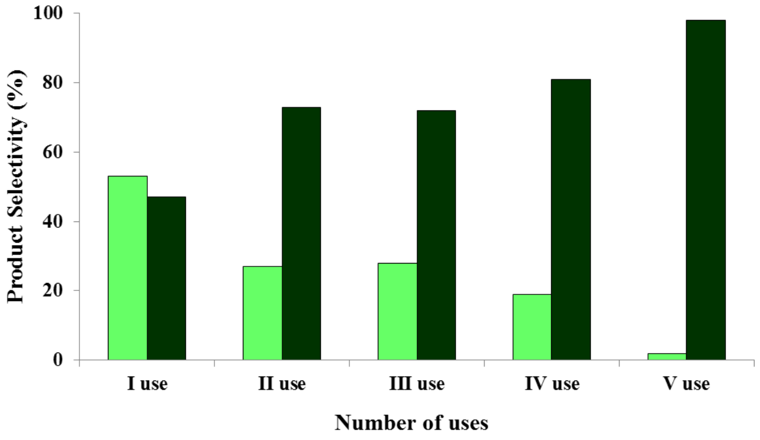

Figure 3-11 Reusability study for the oxidation of HMF using Au-Ce catalyst. HMFCA (🟩) and FDCA (■) selectivities are given at total conversion. Reaction conditions: temperature 70°C, reaction time 240 min, O_2 pressure 10 bar, HMF:Metal:NaOH molar ratio 1:0.01:4.

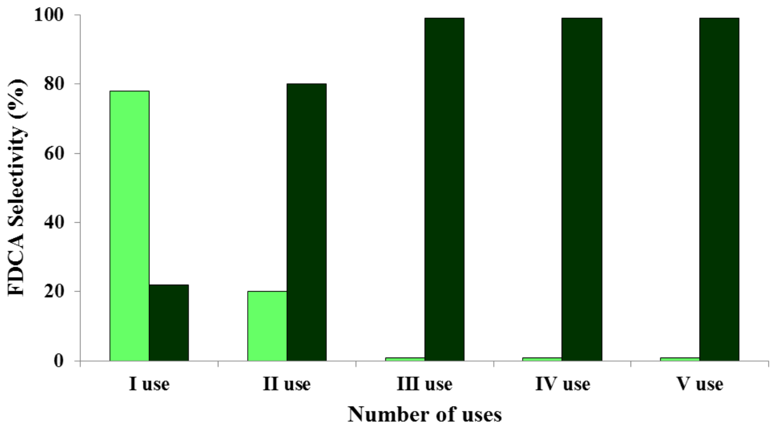

Figure 3-12 Reusability study for the oxidation of HMF using Au_3Cu_1-Ce catalyst. HMFCA (🟩) and FDCA (■) selectivities are given at total conversion. Reaction conditions: temperature 70°C, reaction time 240 min, O_2 pressure 10 bar, HMF:Metal:NaOH molar ratio 1:0.01:4.

As already discussed, it is known that the changes brought about either by the support on metal particles or vice versa are mainly restricted to atoms either at the interface or at the perimeter of the nanoparticles, where reactants can interact simultaneously with both the oxidic support and the metal catalyst. Moreover, reducible supports, such as CeO_2, can provide activated oxygen[28] and stabilize cationic gold[29]. These functions have been ruled out in gold-based catalysts when the latter are used in gas-phase reactions[30]. However, the capability of Au to activate CeO_2 is strongly improved by the interaction between the latter and metal particles, and this cooperative effect may be hindered by the presence of the residual capping agent (PVP) used.

On the other hand, it is likely that the removal of the capping agent takes place during reactions, thus increasing the support-nanoparticle interaction and leading to an increased activity during repeated uses. In order to verify this hypothesis, an in-depth study of the effect of the capping agent removal on Au and Au/Cu catalysts was performed.

3.3.5 Treated catalysts:effect of capping agent removal

Capping ligands such as surfactants and polymers are widely used for the synthesis of nanometals to control their size and shape[31]. Moreover, it has also been found that the ligands chemisorbed on the nanoparticles can hinder the reagents' access to the active surface[32,33,34,35]. PVP is among the most commonly used capping ligands in the chemical synthesis of nanometals. The wrapping of PVP around metal nanoparticles results in a metallic core-porous PVP shell architecture with a coordination of the carbonyl group and nitrogen atom of the pyrrolidone ring with the nanoparticle. Chemisorbed ligands were found to poison the catalytic activity of metals by lowering the accessibility of reactants to the metal surface[36]; moreover, it was observed that PVP interaction with metal nano-crystals is accompanied by the charge transfer[37]. This interaction can modify the structure of metal colloids, sometimes with beneficial effects on the catalytic performance[38]. Indeed, Baumer's work reports a number of benefits that such ligand shells may have for heterogeneous catalysis, including the tuning of strong metal-support interaction (SMSI) effects[39].

Previous results obtained by our research group [23, 31] demonstrated that the PVP presence over Au and Au/Cu TiO_2-supported catalysts does not prevent their activity in HMF oxidation. However, the catalysis over CeO_2-supported samples seems to indicate an important effect of the capping agent on both Au-CeO_2 and Au/Cu-CeO_2 catalysts; therefore, further experiments were conducted on these materials in order to investigate their catalytic behavior after removal of the PVP stabilizer.

Various studies have reported on the difficulties encountered during the removal of the residual capping agent from nanoparticles[40,41]. Various strategies, such as chemical and thermal treatments of catalysts[42,43,44], may be used. We tested two different treatments with the aim of obtaining surface-clean Au and Au/Cu species over CeO_2: i) catalyst washing in autoclave using reaction conditions (T=70°C, 4h, 10 bar of oxygen pressure, with Metal:NaOH molar ratio equal to 0.01:4), but in the absence of HMF, and ii) thermal treatment at T=300°C. The results obtained are summarized in Table 3-3.

Entry	**Sample**	**Treatment**	ϕ_{FDCA} **(%)**	Φ_{HMFCA} **(%)**	d_{XRD} **(nm)**
1	Au-Ce	As is (dried 120°C)	47	53	6.0
2	Au-Ce	Washed in reaction conditions	92	8	6.5
3	Au-Ce	Thermal treated 300°C	91	9	7.2
4	Au_3Cu_1-Ce	As is (dried 120°C)	22	78	5.0
5	Au_3Cu_1-Ce	Washed in reaction conditions	22	78	6.0
6	Au_3Cu_1-Ce	Thermal Treated 300°C	41	59	21.0
7	Au_3Cu_1-Ce	Washed in reaction conditions and thermal treated 300°C	71	29	11.0

Table 3-3 Comparison of the selectivity (ϕ) of the reaction products obtained with treated and untreated catalysts. For all reactions, HMF conversion was complete. Reaction conditions: Temperature = 70°C, reaction time 240 min, O_2 pressure 10 bar, HMF:Metal:NaOH molar ratio 1:0.01:4.

The washing treatment of the Au-Ce sample in reaction conditions significantly boosted the activity; indeed, FDCA selectivity over this sample increased from 47% (Table 3-3, entry 1) to 92% (Table 3-3, entry 2). Gold-supported nanoparticles retained their dimension and TPO analysis confirmed that the catalyst surface was clean.

Similar results (FDCA selectivity 92%) were obtained by decomposing the capping agent through thermal treatment. TG and TPO analysis demonstrated the decomposition of PVP at this temperature. Nevertheless, the average size of gold nanoparticles, as evaluated by XRD and TEM on the calcined sample, underwent a slight increase, from 6 to 7.2 nm. This is not surprising, since Au nanoparticles are frequently seen to sinter after the thermal treatment carried out to remove organic ligands[34]; however, the low exothermicity associated with this treatment, due to the relatively low PVP content, made it possible to limit the particle growth.

The reported results indicate that the trend observed during repeated Au-Ce sample use is related to the PVP removal during reaction, and that the metal-CeO_2 interface plays a pivotal role in the oxidation of HMF.

The same treatments were carried out with the bimetallic catalyst Au_3Cu_1-Ce. The results obtained (Table 3-3, entries 4 and 5) indicate that the simple washing of the catalyst did not improve the catalytic activity at all, while the obtained FDCA selectivity remained 22% after this treatment. As previously reported, it must be pointed out that Cu-containing nanoparticles were prepared with a higher PVP amount, due to the difficulty in controlling the particle growth in preformed Au/Cu sols; therefore this high PVP content seems to be more difficult to remove. Moreover, the affinity of PVP with Cu/Au nanoparticles might be higher, due to the ability of PVP to form complex compounds with Cu[44].

Zhang and co-workers recently studied the removal of PVP on Au nanoparticles using $NaBH_4$ in water[45]; they demonstrated that the hydride derived from sodium borohydride has a higher binding affinity to nanoparticles than PVP. Moreover, a redox cycle was shown to remove PVP from nanoparticles[3]. These results might explain the different activation obtained by treating Au/Cu samples in reaction conditions either with HMF (during re-use tests) or without HMF (Table 3-3, entry 5); in fact, HMF oxidation may foster the displacement of PVP from the nanoparticle surface, thus inducing a higher metal-CeO_2 interaction while significantly increasing FDCA formation.

TPO analysis on Au_3Cu_1-Ce samples after pre-treatment in reaction conditions (Figure 3-13) confirmed the incomplete removal of PVP from the catalyst surface. Although the TPO signal is significantly lower than that of the Au_3Cu_1-Ce sample before treatment – thus indicating that the washing procedure is effective in removing most of the PVP – the treatment might not completely eliminate the PVP located at the interface between Au and CeO_2, thus limiting the metal-support interaction.

Very different results were obtained after the thermal treatment of the Au_3Cu_1-Ce catalyst at 300°C in air. In this case, the thermal treatment completely decomposed the stabilizer, which resulted in a significantly increased FDCA selectivity; the latter increased from 22% (Table 3-3, entry 4) to 41% (Table 3-3, entry 6). However, the very high exothermicity entailed with PVP combustion strongly conditioned the average size of Au/Cu nanoparticles, which showed a considerable sintering phenomenon. In this case, the heat developed during the thermal treatment was higher than that for Au-supported catalysts, because a higher PVP content was used to synthesize Au/Cu nanoparticles. Indeed, the particle size increased from 5 to 21 nm, thus making it difficult to discriminate – in the observed FDCA yield increase effect – among various effects, i.e. the influence of particle size, phase segregation, and metal-oxide interface. As a matter of fact, the activity in alcohol oxidation was reported to be affected by particle size; the optimum particle size was shown to be around 3-5 nm[46,47,48].

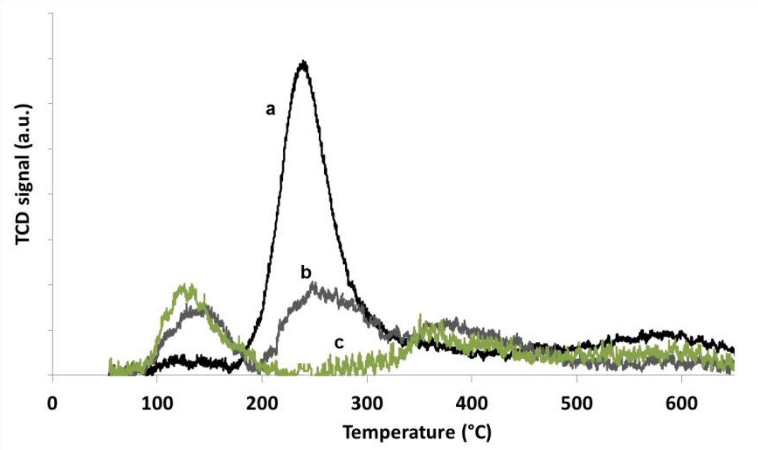

Figure 3-13 TPO analysis of Au_3Cu_1-Ce catalysts. Legend: (a) untreated Au_3Cu_1-Ce; (b) Au_3Cu_1-Ce washed in reaction conditions; (b) Au_3Cu_1-Ce washed in reaction conditions and then calcined at 300°C.

Nevertheless, our data demonstrate that large Au particles (size > 20 nm) are also able to oxidize HMF with high selectivity, if a suitable interaction with the ceria support is guaranteed. These data confirm some recently reported results on the conversion of aromatic alcohols[49] over unsupported bulk Au; those results showed that the interaction between the gold surface and the aromatic ring enhances the overall efficiency of the active site even in the presence of large particles.

In order to distinguish between the effect of particle size and that derived from PVP removal, the decomposition of PVP was also obtained by calcination of the Au_1Cu_3-Ce sample at 300°C after washing in reaction conditions. The lower exothermicity, due to the lower stabilizer content, made it possible to control the particle size growth, which increased just to 11 nm, instead of the 21 nm for the unwashed sample. This two-stage decomposition of PVP significantly boosted the catalyst activity, while the FDCA selectivity increased from 41% (Table 5-1, entry 6) to 71% (Table 3-3, entry 7), thus confirming the significant effect of the active phase particle size on catalytic performance.

The mechanism of HMF reaction is still a matter of debate. Davis and co-workers[50] demonstrated the important role of hydroxyls for the liquid phase oxidation of alcohols catalyzed by Au; they suggested that the role of O_2 in aqueous media is an indirect one, which does not involve incorporation into the acid products, but rather regenerates hydroxide ions, by removing the electrons from the Au surface[51]. However, no comments are reported in literature regarding the possible role of CeO_2. Our results indicate that the metal-CeO_2 interface plays a pivotal role, similarly to what is observed in gas-phase reactions. Since the rate-controlling step of the reaction appears to be the oxidation of HMFCA[20], it may be suggested that ceria acts as an oxygen (or hydroxyl) pump, by releasing and adsorbing the oxidizing species through the Ce^{+4}/Ce^{+3} redox process, as also suggested by Corma and co-workers[52]. Nevertheless, this effect is observed only in the presence of a close contact between metal and support, thus suggesting an important role of ceria defects induced by the metal presence[53].

3.4 Conclusions

The use of preformed metal nanoparticles with well-defined size and composition supported over titania or ceria was used to explore the role of the metal–support interaction in the oxidation of HMF over Au and Au/Cu catalysts. The deposition of preformed nanoparticles is not support-dependent[54], a fact that made it possible to investigate the support effect on the activity and selectivity in HMF oxidation to FDCA. The results obtained demonstrate that CeO_2 is the most effective support for obtaining active and selective catalysts for FDCA synthesis. However, pre-made uniform nanoparticles, used for catalyst preparation, were surface-bound by poly(N-vinyl-2-pyrrolidone) (PVP), the organic capping agents used for nanoparticle synthesis, and the presence of this stabilizer hindered the chemical interaction between the active phase and CeO_2. Indeed, pre-treatment of catalysts was necessary in order to remove the PVP, enable the interaction between ceria and metal nanoparticles at the interface, and ultimately activate the catalyst, events which led to the enhancement of the catalytic performance.

---

[1] E. Bayrakdar, T. Gürkaynak Altınçekiç, M. A. Faruk Öksüzömer, *Fuel Process. Technol*. 110 (2013) 167-175.

[2] C. Kim, H. Lee, *Catal. Comm*. 10 (2009) 1305-1309.

[3] R. M. Rioux, H. Songa, M. Grass, S. Habas, K. Niesz, J. D. Hoefelmeyer, P. Yang, G. A. Somorjai, *Top. Catal*. 39 (2006) 167-174.

[4] L. M. Rossi, L. L. R. Vono, M. A. S. Garcia, T. L. T. Faria, J. A. Lopez-Sanchez, *Top Catal.* 56 (2013) 1228-1238.

[5] S. Albonetti, T. Pasini, A. Lolli, M. Blosi, M. Piccinini, N. Dimitratos, J. A. Lopez-Sanchez, D. J. Morgan, A. F. Carley, G. J. Hutchings, F. Cavani, *Catal. Today* 195 (2012) 120-126.

[6] T. Pasini, M. Piccinini, M. Blosi, R. Bonelli, S. Albonetti, N. Dimitratos, J. A. Lopez-Sanchez, M. Sankar, Q. He, C. J. Kiely, G. J. Hutchings, F. Cavani, *Green Chem*. 13 (2011) 2091-2099.

[7] K. R. Vuyyuru, P. Strasser, *Catal. Today* 195 (2012) 144-154.

[8] K. R. S. Patil, C. R. F. Lund, *Energy and Fuels* 25 (2011) 4745-4755.

[9] A. Piccolo, P. Conte, A. Cozzolino, *Eur. J. Soil Sci*. 50 (1999) 687-694.

[10] S. E. Davis, B. N. Zope, R. J. Davis, *Green Chem*. 14 (2012) 143-147.

[11] A. Shalkh, D. R. Parker, M. E. Janka, L. R. Partin, *US Patent* 2014/0142328 (2014) assigned to Eastman Chemical Company.

[12] C. Moreau, M. N. Belgacem, A. Gandini, *Top. Catal*. 27 (2004) 11-30.

[13] J. Cai, H. Ma, J. Zhang, Q. Song, Z. Du, Y. Huang, J. Xu, *Chem. Eur. J*. 19 (2013) 14215-14223.

[14] O. Casanova, S. Iborra, A. Corma, *ChemSusChem*. 2 (2009) 1138-1144.

[15] N. K. Gupta, S. Nishimura, A. Takagaki, K. Ebitani, *Green Chem*. 13 (2011) 824-827.

[16] M.A. Lilga, R. T. Hallen, J. Hu, J. F. White, M.J. Gray, *US* 2010/0152470 (2010) assigned to Battelle Memorial Institute.

[17] R. Si, M. Flytzani-Stephanopoulos, *Angew. Chem. Int. Ed*., 47 (2008) 2884-2887.

[18] J. L. He, T. Xu, Z. H. Wang, Q. H. Zhang, W. P. Deng, Y. Wang, *Angew. Chem. Int. Ed.* 51 (2012) 2438-2442.

[19] A. Abad, P. Concepción, A. Corma, H. García, *Angew. Chem. Int. Ed*. 44 (2005) 4066-4069.

[20] K. Mori, T. Hara, T. Mizugaki, K. Ebitani, K. Kaneda, *J. Am. Chem. Soc*. 26 (2004) 10657-10666.

[21] M. Cargnello, P. Fornasiero, R. J. Gorte, *Catal. Lett*. 142 (2012) 1043-1048.

[22] P. Lakshmanan, F. Averseng, N. Bion, L Delannoy, J.-M Tatibouët, C. Louis, *Gold Bulletin* 46 (2013) 233-242.

[23] V. V. Pushkarev, V. I. Kovalchuk, J. L. d'Itry, *J. Phys Chem B* 108 (2004) 5341-5348.

[24] C. Li, K. Domen, K.Maruya, T. Onishi, *J. Catal*. 123 (1990) 436-442.

[25] C. Oliva, G. Termignone, F. P. Vatti, L. Forni, A. V. Vishniakov, *J. Mater. Sci*. 31 (1996) 149-158.

[26] D. Martin, D. Duprez, *J. Phys. Chem*. 100 (1996) 9429–9438.

[27] S. Subbiah, S. P. Simeonov, J. M. S. S. Esperança, L. Paulo N. Rebelo, C. A. M. Afonso, *Green Chem*. 15 (2013) 2849-2853.

[28] L. Kundakovic, M. Flytzani-Stephanopoulos, *J. Catal*., 179 (1998) 203-221.

---

[29] M. Wang, F. Wang, Ji. Ma, M. Li, Z. Zhang, Y. Wang, X. Zhang, J. Xu, *Chem. Commun*. 50 (2014) 292-294

[30] M. J. Beier, T. W. Hansen, J-D. Grunwaldt, *J. Catal*. 266 (2009) 320-330.

[31] Y. N. Xia, Y. J. Xiong, B. Lim, S. E. Skrabalak, *Angew. Chem. Int. Ed*. 48 (2009) 60-103.

[32] A. Villa, D. Wang, D. S. Su, L. Prati, *ChemCatChem* 1 (2009) 510-514.

[33] G. A. Somorjai, H. Frei, J. Y. Park, *J. Am. Chem. Soc*. 131 (2009) 16589-16605.

[34] H. Tsunoyama, N. Ichikuni, H. Sakurai, T. Tsukuda, *J. Am. Chem. Soc*. 131 (2009) 7086-7093.

[35] C. Evangelisti, N. Panziera, A. D’Alessio, L. Bertinetti, M. Botavina, G. Vitulli, *New J. Catal*. 272 (2010) 246-252.

[36] A. Quintanilla, V. C. L. Butselaar-Orthlieb, C. Kwakernaak, W. G. Sloof, M. T. Kreutser, F. Kapteijn, *J. Catal*. 271 (2010) 104-114.

[37] Y. Borodko, S. M. Humphrey, T. D. Tilley, H. Frei, G. A. Somorjai,, *J. Phys. Chem. C* 111 (2007) 6288-6295.

[38] K. Chen, H. Wu, Q. Hua, S. Chang, W. Huang *Phys. Chem. Chem. Phys*. 15 (2013) 2273-2277.

[39] P. Sonstrom, M. Baumer, *Phys. Chem. Chem. Phys*. 13 (2011), 19270-19284.

[40] S. O. Blavo, E. Qayyum, L. M. Baldyga, V. A. Castillo, M.D. Sanchez, K. Warrington, M. A. Barakat, J.N. Kuhn, *Top. Catal*. 56 (2013) 1835-1842.

[41] Z. Niu, Y. Li, *Chem. Mater*. 26 (2014) 72-83.

[42] L. R. Baker, G. Kennedy, J. M. Krier, M. Van Spronsen, R. M. Onorato, G. A. Somorjai, *Catal Lett* 142 (2012) 1286-1294.

[43] J. A. Lopez-Sanchez, N. Dimitratos, C. Hammond, G. L. Brett, L. Kesavan, S. White, P. Miedziak, R. Tiruvalam, R. L. Jenkins, A. F. Carley, D. Knight, C. J. Kiely, G. J. Hutchings, *Nature Chem*. 3 (2011) 551-556.

[44] S. Fernandes, H.-S. Kim, R. Hatti-Kaul, *Protein Expres. Purif*. 24 (2002) 460-469.

[45] S. M. Ansar, F. S. Ameer, W. Hu, S. Zou, C. U. Pittman, D. Zhang, *Nano Lett*. 13 (2013) 1226-1229.

[46] W. C. Ketchie, Y-L Fang, M. S. Wong, M. Murayama, R. J. Davis, *J. Catal*. 250 (2007) 94-101.

[47] F. Li , Q. H. Zhang Y. Wang, *Appl. Catal. A* 334 (2008) 217-226.

[48] S. E. J. Hackett, R. M. Brydson, M. H. Gass, I. Harvey, A. D. Newman, K. Wilson, *Angew. Chem. Int. Ed*. 46 (2007) 8593-8596.

[49] H. Guo, A. Al-Hunaiti, M. Kemell, S. Rautiainen, M. Leskela, T. Repo, *ChemCatChem* 3 (2011) 1872-1875.

[50] M. S. Ide, R. J. Davis, *Acc. Chem. Res*. 47 (2014) 825–833.

[51] B. N. Zope, D. D. Hibbitts, M. Neurock, R. J.Davis, *Science* 330 (2010) 74-78.

[52] O. Casanova, S. Iborra, A. Corma, *J. Catal.* 265 (2009) 109-116.

[53] H.-F. Li, N. Zhang, P. Chen, M.-F. Luo, J.-Q. Lu, *Appl. Catal. B* 110 (2011) 279-285.

[54] N. F. Zheng, G. D. Stucky, *J. Am. Chem. Soc*. 128 (2006) 14278-14280.

CHAPTER 4

Ceria HT

The work in this chapter was the basis for the publication A. Lolli, F. Cavani, R. Amadori, S. Albonetti, M.G. Cutrufello, E. Rombi "Hard template preparation of Au/CeO_2 mesoporous catalysts and their activity for the selective oxidation of 5-hydroxymethylfurfural to 2,5-furandicarboxylic acid" in preparation.

4.1 Introduction

Highly ordered mesoporous CeO_2 has been prepared by a hard template method using SBA-15 as a structure-directing agent. Leaching with NaOH and thermal treatment at 500°C allowed the removal of inorganic template, resulting in the formation of long-range ordered CeO_2. Nevertheless, small amount of silica was present in the final oxides. The resulting CeO_2 samples were utilised as support for Au nanoparticles and the prepared catalysts were tested in the selective oxidation of 5-hydroxymethylfurfural to 2,5-furandicarboxylic acid.

4.2 CeO_2 synthesis and characterization

Mesoporous CeO_2 has been prepared by the hard template method with the procedure previously described. This nanocasting process allows to replicate the morphology of the SBA-15 template in a reverse form. The calcination of mesoporous silica impregnated with the cerium salt leads to the formation of crystalline ceria inside the SBA-15 pores; then the silica framework can be dissolved by NaOH treatment. The removal of silica template, which probably has oxygen linkages with ceria, may produce structural defects. Moreover, the further calcination of the solid after the leaching step was reported[1] to have a positive effect on the crystallinity and stability of material; nevertheless, high temperature treatment may also cause a significant decrease in the number of corner and edge sites[1,2] as well as in the concentration of oxygen vacancies[3], whose presence can positively affect the catalytic activity. The pivotal role of the template-leaching process in the formation of the mesostructured CeO_2 support has been thoroughly investigated by performing a different number of template-removal cycles, as reported in Table 4-1.

Therefore, since template-leaching processes play a pivotal role in the formation of the mesostructured CeO_2 support, different number of template-removal cycles were performed and deeply investigated, as it has been summarized in Table 4-1.

Sample	**Number of template-removal cycles***	**Surface area (m^2/g)**	**V_p (cm^3/g)**	**SiO_2 (wt%)**
CeO_2_a	1	121	0.314	2.6
CeO_2_b	2	113	0.318	1.8
CeO_2_c	3	103	0.304	1.9
commercial CeO_2	-	53	-	-

Table 4-1 Procedure for template elimination (SBA-15), textural features, and residual SiO_2 content of the synthesized mesoporous CeO_2 supports.

***Each cycle consisted in leaching process and following steps of washing, drying and calcination.**

Wide angle XRD patterns of the synthesized CeO_2 materials (Figure 4-1) show peaks at 2θ values of 28.6, 33.1, 47.5, and 56.4°, ascribable to the (111), (200), (220), and (311) reflection lines of the face-centered cubic-phase fluorite-type structure of cerium oxide [PDF card 98-009-5649], which indicate the formation of well crystallized materials irrespective of the template-removal and/or calcination conditions used during the synthesis. The size of CeO_2 nanoparticles, calculated by the Scherrer equation, is in the range 8-10 nm for all samples. The commercial sample also shows the typical reflection peaks of cerium oxide, which, however, appear narrower, indicating a higher value of the mean particles size (18 nm).

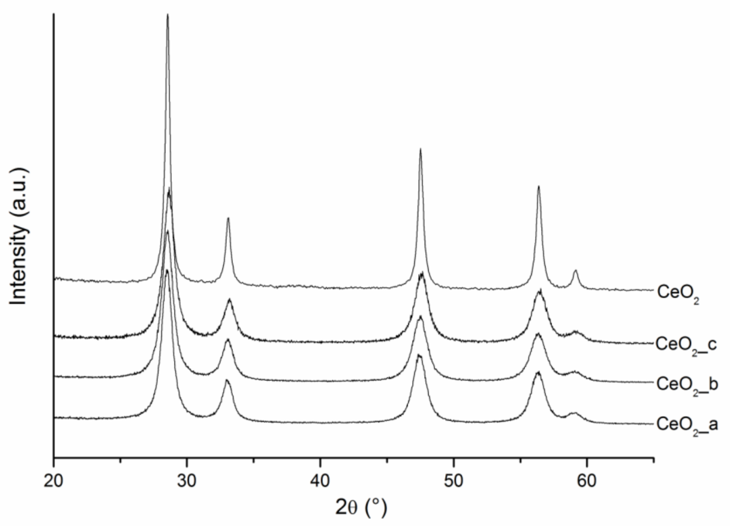

Figure 4-1 WAXRD patterns of the mesoporous supports (CeO$_2$_a, CeO$_2$_b, CeO$_2$_c) and the commercial oxide (CeO$_2$).

Low angle XRD results for CeO$_2$_a and CeO$_2$_b are shown in Figure 4-2. Three signals, which can be indexed as the (100), (110), and (220) reflections characteristic of the 2-D hexagonal (*P6mm*) structure, can be observed in the diffraction patterns of both samples, indicating that the original mesostructure of the SBA-15 template is replicated.

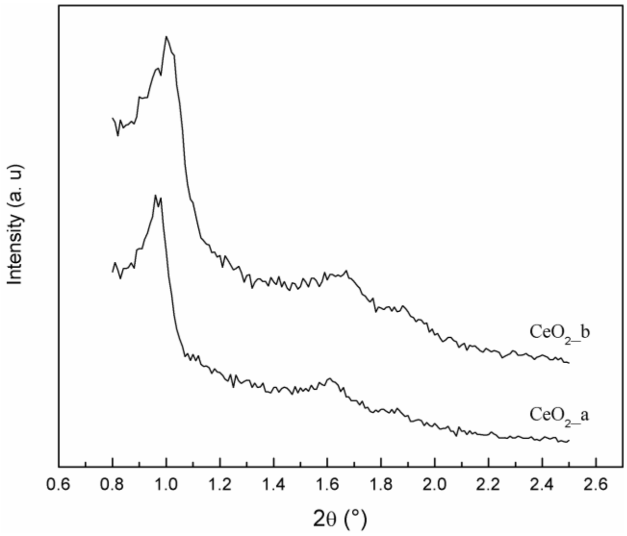

Figure 4-2 LAXRD patterns of the mesoporous sample CeO$_2$_a and CeO$_2$_b.

The low angle X-ray diffraction pattern of SBA-15 in Fig. S1 shows three well-resolved peaks ascribable to (1 0 0), (1 1 0), and (2 2 0) reflections typical of the 2-D hexagonal (*P6mm*) structure.

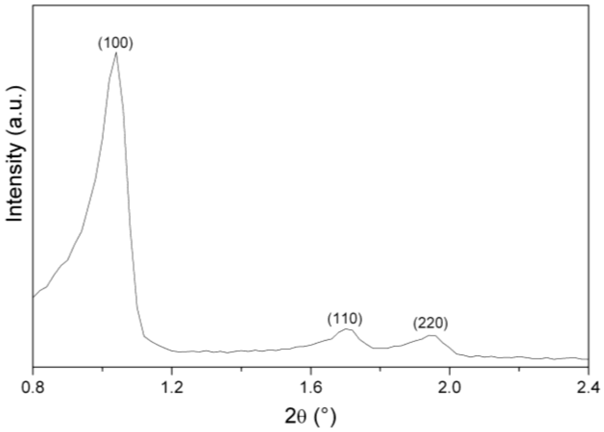

Figure 4-3 Low angle X-ray diffraction of SBA-15 silica template

The N_2 adsorption-desorption isotherms and the pore size distribution curves of the CeO_2 supports are reported in Figure 4-4. All samples exhibit a type IIb isotherm[4] with a hysteresis loop typical of mesoporous solids (Figure 4-4 a-c). Surface area, S.A., and pore volume, V_p, were calculated from the BET equation. The BJH method was applied to the desorption branch of the isotherms to obtain the pore size distribution curves (Figure 4-4 e-g).

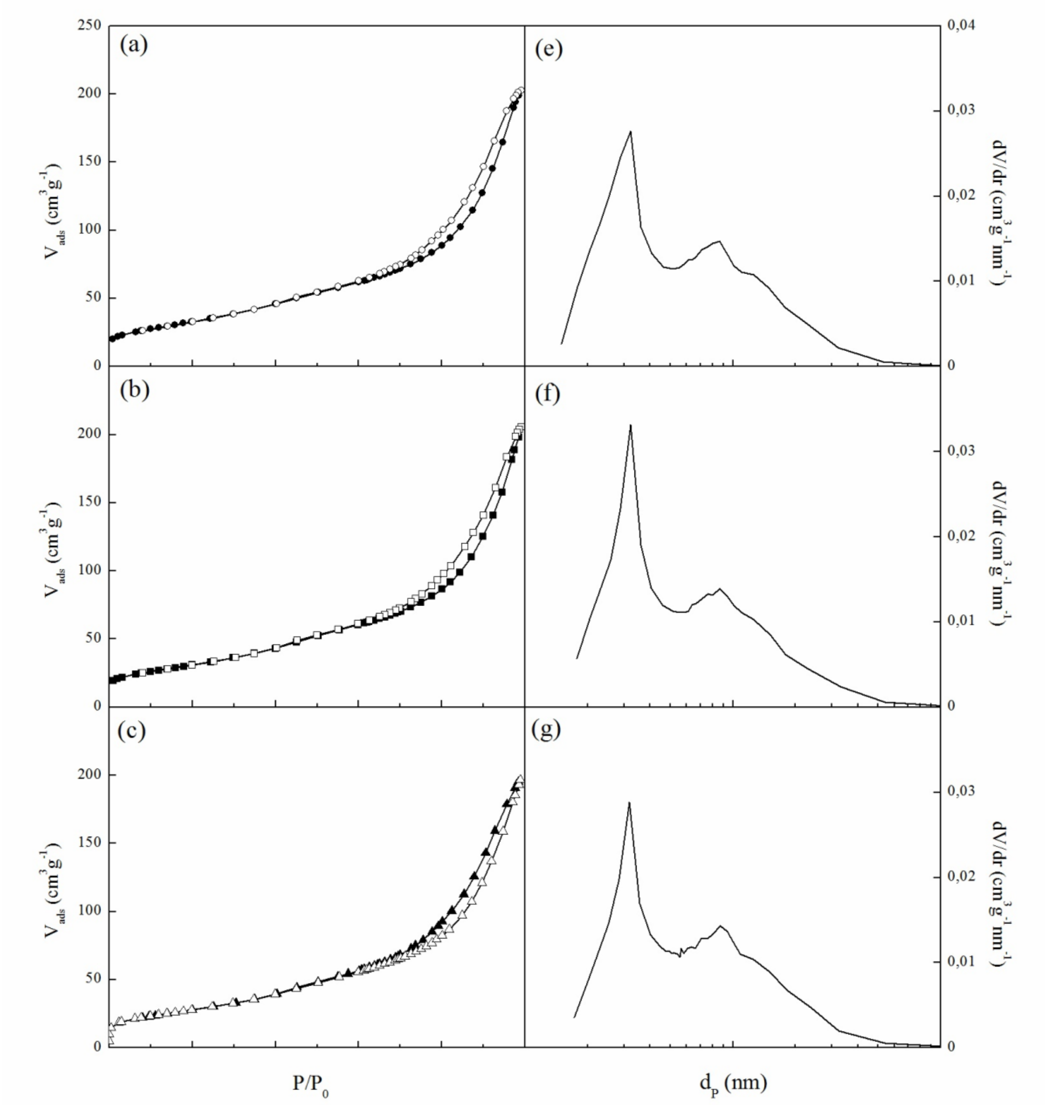

Figure 4-4 N_2 Adsorption/desorption isotherms (a-c) and pore size distribution (d-f) of the mesoporous materials. Legend: (a,d) CeO_2_a, (b,f) CeO_2_b, (c,g) CeO_2_c.

The textural results are summarized in Table 4-1. The hard-templated CeO_2 supports exhibit surface area values in the range 103-121 m^2/g, much higher than that of the commercial cerium oxide (53 m^2/g). The obtained S.A. values are comparable with those reported in the literature (ca. 100 m^2/g) for mesoporous ceria nanocasted from SBA-15[5,6]. These values seem to slightly decrease with the increase in the number of template-removal cycles. All the hard-templated samples show a bimodal distribution of the pores size, with a first peak centred at ca. 3.2 nm and a second broad peak centred at ca. 9 nm. The pore size value of 3.2 nm is consistent with the pore wall thickness of the parent SBA-15 which seems to suggest that the materials are replicas of the topological structure of the template, in agreement with the low angle XRD results. Nitrogen physorption results are reported in (Figure 4-5a), which shows a type IV isotherm with an H1 hysteresis loop at high relative pressures, typical of SBA-15. A surface area of 820 m^2/g and a pore volume of 1.18 cm^3/g were calculated from the BET equation. The BJH method was applied to the desorption branch of the isotherm to obtain the pore size distribution curve (Figure 4-5b) which appears quite narrow and centred at 6.2 nm, in agreement with the TEM results. The internal architecture of SBA-15 is clearly visible in the TEM image shown in Figure 4-6, which confirm the highly ordered 2-D hexagonal regularity. The ordered arrays of silica channels have a mean diameter of *ca.* 6-7 nm with a wall thickness of about 3 nm.

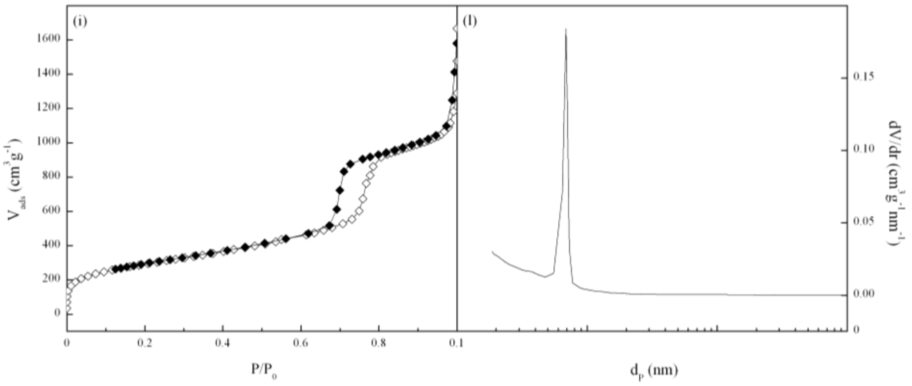

Figure 4-5 Nitrogen adsorption-desorption isotherm and pore size distribution (inset) of SBA-15.

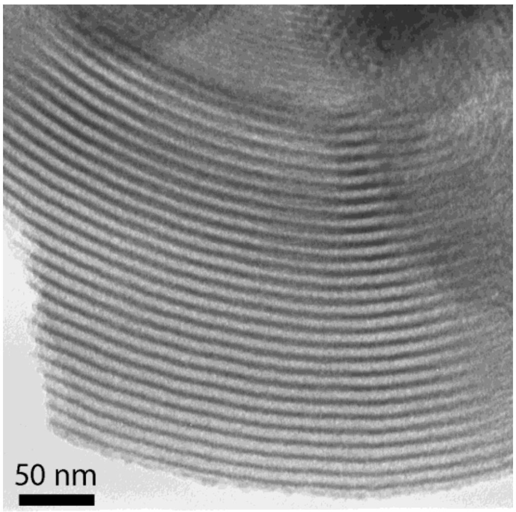

Figure 4-6 TEM image of the SBA-15 silica template.

However, the presence of the second contribution, indicative of the presence of larger pores with a broad size distribution, suggests that the structure of the obtained materials is partially disordered. TEM images of the CeO_2_a (Figure 4-7) and CeO_2_b (Figure 4-8) actually show that structural collapse has occurred to some extent during (or after) the leaching process.

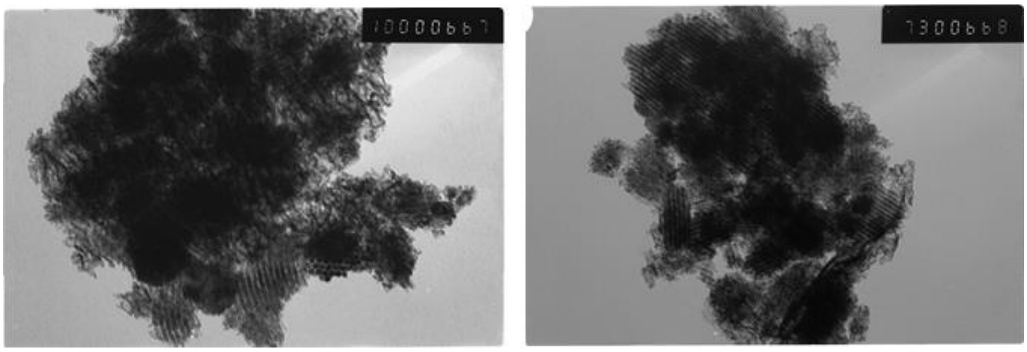

Figure 4-7 HRTEM images of the sample CeO_2_a. scala!

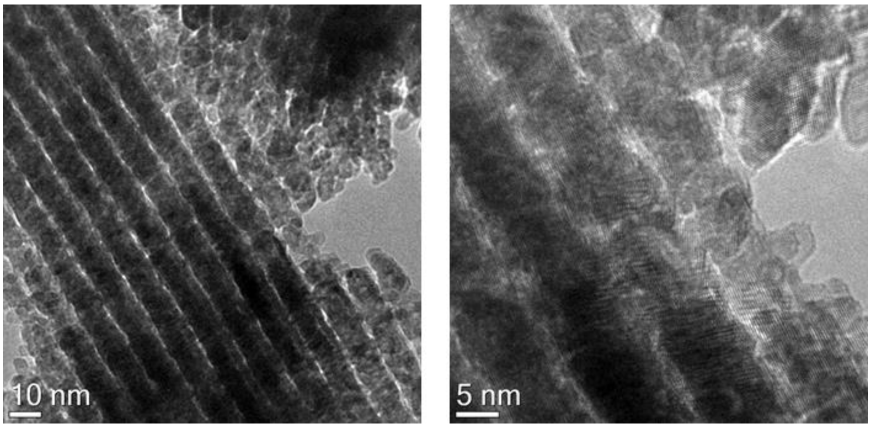

Figure 4-8 HRTEM images of the sample CeO_2_b.

XRF analyses have been performed on the prepared ceria supports to check the presence of residual silica, which may have a detrimental effect on catalytic activity by promoting gold sintering[7]. The results show that small amounts of the silica template remain in all the synthesised samples, suggesting that the complete removal of the template is very demanding. The obtained results are in agreement with those reported in the literature on similar materials[8]. By repeating twice the template-removal process it is possible to reduce the residual amount of silica, which however remains constant after a further leaching-calcination cycle.

4.3 Au supported catalysts

Gold nanoparticles were deposited onto CeO_2_a and CeO_2_b; the CeO_2_c support (which exhibits structural and textural properties as well as residual silica content very similar to those of CeO_2_b) was not further considered. Au/CeO_2 catalyst supported on commercial ceria (Au/CeO_2) was also prepared for comparison.

Catalysts surface area and gold particle size are reported in Table 4-2. The surface area of all mesostructured materials is close to 110 m^2/g, indicating that gold deposition does not significantly affect this parameter which remains quite high for all samples. The slight increase in the S.A. could be observed because of the elimination of PVP, which surrounded the nanoparticles and may occlude oxide porosity.

Sample	Surface Area (m^2/g)	d_{XRD} (nm)	d_{HRTEM} (nm)
Au/CeO_2_a dried 120 °C	110	8	-
Au/CeO_2_a calcined 300 °C	113	14	13
Au/CeO_2_b dried 120 °C	-	8	6
Au/CeO_2_b calcined 300 °C	108	8	7
Au/CeO_2 dried 120 °C	53	6	5
Au/CeO_2 calcined 300 °C	60	7	7

Table 4-2 Catalysts surface area and gold particle size from XRD and HRTEM analysis for the prepared catalyst.

Metal particles size was determined both using XRD analysis and from HRTEM images. These techniques gave the same results and highlighted the existing correlation between gold particle size and SiO_2 content for mesoporous materials. In fact, these catalysts had generally bigger particles if compared to the commercial one. Furthermore, mesoporous CeO_2 oxide with higher SiO_2 content (Au-CeO_2_a) showed an increase in the particle size of the calcined catalyst. Therefore, silica can promote gold sintering during calcination leading to a catalyst which has gold nanoparticles of 14 nm. Despite of the fact that mesoporous catalysts were characterised by bigger gold particle size with respect to the commercial support, 8 nm particles are still interesting from the catalytic point of view[14]**Errore. Il segnalibro non è definito.**. XRD patterns (Figure 4-9) shows clearly the presence of bigger particles in the sample Au-CeO_2_a calcined, while sample Au-CeO_2_b seems to be more similar to the commercial catalysts. Even in this case, the larger reflection peaks belonging to the mesoporous support highlighted the presence of smaller particles.

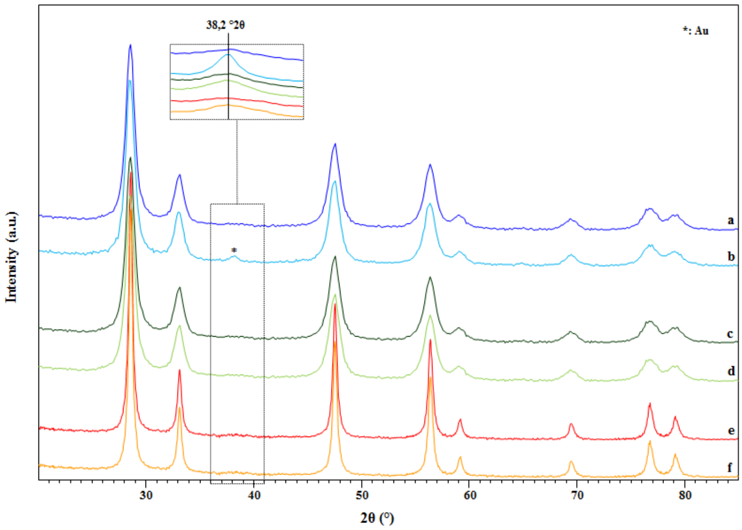

Figure 4-9 XRD patterns of the dried and calcined supported catalyst. Inset: magnification of the reflection at 2θ 38.2° which was used to evaluate Au crystal size. Legend: a) Au-CeO_2_a dried, b) Au-CeO_2_a calcined, c) Au-CeO_2_b dried, d) Au-CeO_2_b calcined, e) Au-CeO_2 dried, Au-CeO_2 calcined.

HRTEM images and particle size distribution of Au-CeO_2_a calcined at 300°C reported in Figure 4-10 highlighted that this sample is characterized by greater nanoparticle size. The distribution of the average particle diameter was evenly distributed in the range 4-24 nm, meaning that Au nanoparticles were not homogeneous in size.

Nevertheless, the preparation of a catalyst with a support containing a lower amount of silica did not lead to particle growth during the calcination step. In Figure 4-11 and Figure 4-12 HRTEM images of Au-CeO_2_b dried and calcined are reported. The distribution profile changed moving from the dried to the calcined sample. The first one is characterized by an even wide distribution in the range 2-11 nm, while the second one is characterized by a Gaussian-like profile in the range 3-10 nm. It is possible to notice only a negligible increase of particle size simply taking into account that the fraction of nanoparticles with average diameter of 2 nm disappeared after the calcination step. Thus, in this case, particle growth is not enhanced and metal nanoparticles have basically the same average diameter even after the calcination treatment.

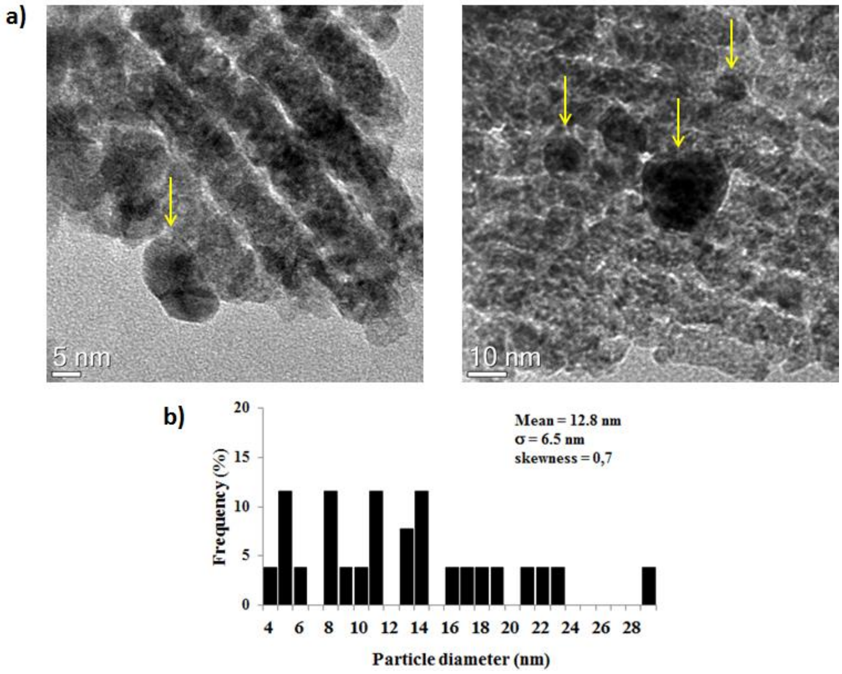

Figure 4-10 a) HRTEM images of Au-CeO$_2$_a calcined; b) Particle size distribution.

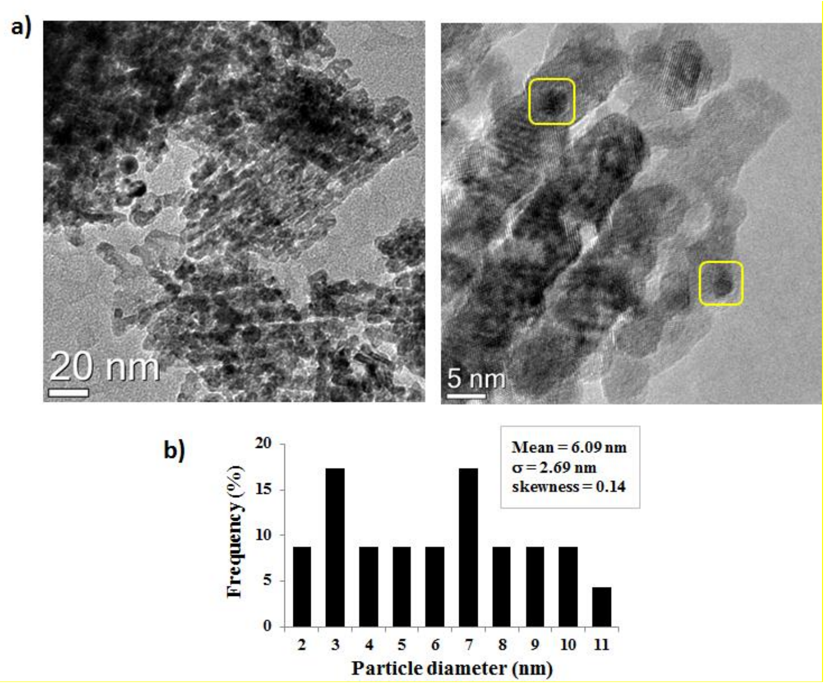

Figure 4-11 a) HRTEM images of Au-CeO$_2$_b dried; b) Particle size distribution.

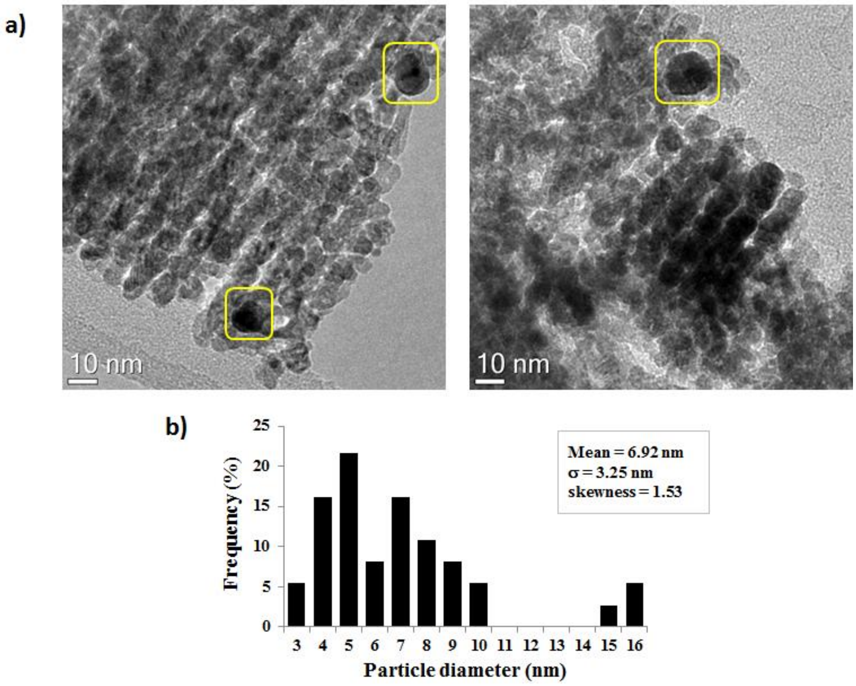

Figure 4-12 a) HRTEM images of Au-CeO_2_b calcined 300°C; b) Particle size distribution.

The preparation of the gold supported catalysts by impregnation of preformed nanoparticles permitted to preserve the mesoporous morphology of the ceria support, keeping high the surface area. This is confirmed by TEM observations: micrographs (Figure 4-10, Figure 4-11, Figure 4-12) clearly showed the ordered rod-like morphology of the materials. Presumably, only a small fraction of gold nanoparticles could have been inserted inside the CeO_2 channels, namely 2-3 nm particles, since cerium oxide pore diameter was very small. Most of the pores had a diameter of 3.2 nm, while the rest was characterized by an average dimension of 9 nm (Figure 4-4), meaning that the majority of particles should have been inside the larger pores or on the surface of mesoporous structure. Comparing the images of the mesoporous catalysts with those of the commercial support (Figure 4-13) a very different morphology could be observed. The commercial sample is not characterized the channel structure typical for the cerium oxide made with the hard template technique. Particle size distribution of the dried and calcined catalysts highlighted that the calcination process led only to a very small increase in nanoparticle dimensions, confirming once again the great influence that SiO_2 has on this systems. Particle size distribution of Au-CeO_2_b dried catalyst is wider and very different from the distribution of the dried commercial sample; this behavior may be due to the presence of silica which enhance particle growth even during the impregnation step.

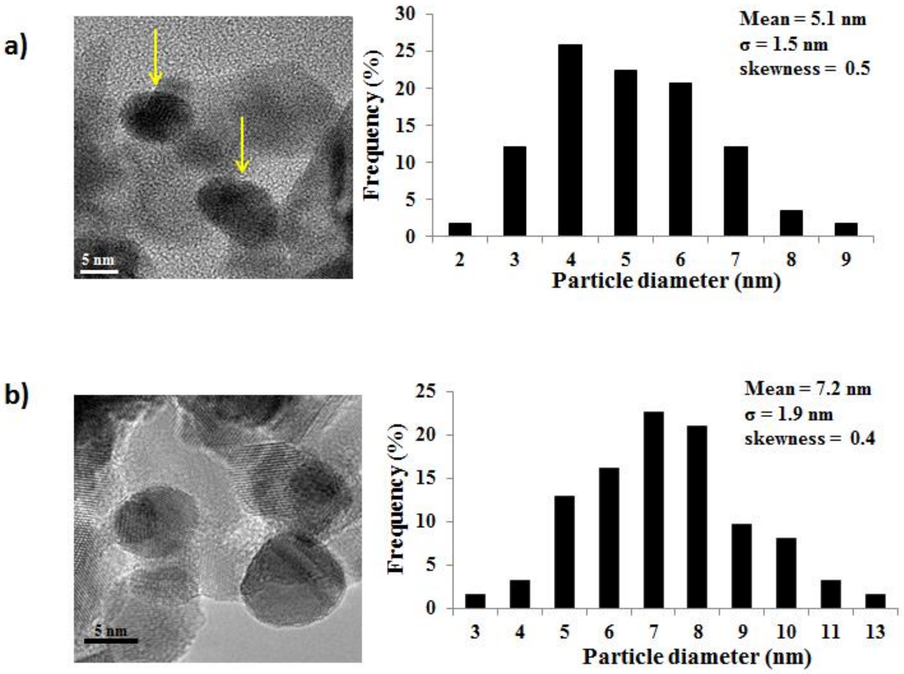

Figure 4-13 a) HRTEM image and particle size distribution of Au-CeO$_2$ dried; b) HRTEM image and particle size distribution of Au-CeO$_2$ calcined 300°C.

It is very well known that the presence of gold can increase the oxygen storage capacity of reducible oxides, such as CeO$_2$, favoring superficial Ce^{4+} reduction.Thus, the chemical effects of gold doping on mesoporous ceria were investigated with TPR technique. H$_2$-TPR profile of selected dried catalysts are present in Figure 4-14.

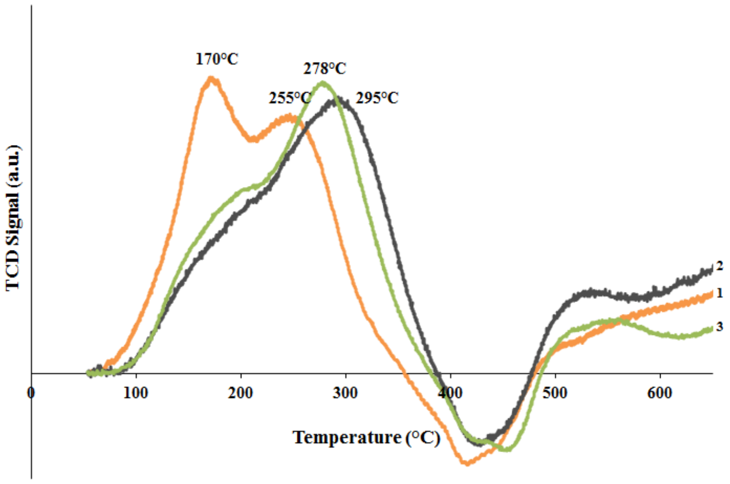

Figure 4-14 TPR profiles of the dried catalysts: 1) Au-CeO$_2$, 2) Au-CeO$_2$_a, 3) Au-CeO$_2$_b.

Typically, the TPR profile of pristine CeO_2 is characterized by reduction peaks at 450-500°C and 800°C which can be ascribed to the surface capping oxide ions and the bulk oxygen, respectively[9,10,11]. In all gold containing sample profiles, intense peaks of reduction at low temperature can be observed, which can be attributed to the reduction of surface cerium atoms. This confirms that gold deposition on ceria leads to the formation of highly reducible ceria species in agreement with literature data, which report that gold can cause a decrease in the strength of the surface Ce–O bonds adjacent to gold atoms, thus leading to a higher surface lattice oxygen mobility and therefore to a higher reactivity of these oxygen species[12]. Remarkable effects on ceria reducibility were observed using every kind of support. All these materials started to be reduced at 100°C and they are characterized basically by two broaden peaks which correspond to different Ce^{4+} species. The reduction temperature is strictly correlated to the interaction of these sites with gold; it decreases with the increase in the metal-support ineraction[12,13]. The profiles of mesoporous samples (Au-CeO_2_a and Au-CeO_2_b) showed similar onset temperature, broaden peaks with a shoulder and lower reduction temperature with respect to the bare support. However, the temperature of the main reduction peak was higher than that obtained with the commercial support. This behaviour could be related to the presence of silica that avoids a proper interaction between gold and ceria, increasing the Ce^{4+} reduction temperature. As a matter of fact, the main reduction peak for the sample Au-CeO_2_a is present at 295°C, while for sample Au-CeO_2_b the typical reduction temperature takes place at 278°C. Nevertheless, it has also to be taken into account that not only was the TCD signal due to hydrogen consumption but it could also be produced by the release of the organic stabilizer (polyvinylpirrolidone) that surrounded the nanoparticles. Indeed, TGA-DTA thermal analysis made on these samples demonstrated that PVP is decomposed at 236°C[14]. In our previous work, it was also observed a CO_2 release during TPO analysis at the same temperature. For these reasons, peak area could not correspond to the exact number of moles of Ce^{4+} reduced. Lastly, in dried samples, a negative peak around 400°C was observed.

The study of the redox properties of the calcined catalysts (Figure 4-15) allowed to avoid the contribution to the TCD signal due to PVP decomposition. The calcined samples displayed narrower peaks and did not show the presence of a negative peak around 400°C; since the calcined samples are different from the dried only because PVP is no more present, the presence of the negative peak could be attributed to a release due to PVP decomposition in the reducing atmosphere. Nevertheless, the mesoporous samples still have a higher reduction temperature than the commercial ones, caused by the presence of silica; greater amount of SiO_2 corresponded to a shift of the reduction peak to higher temperature. Thus, the reduction profiles obtained for calcined mesoporous catalysts confirmed that the degree of interaction between the metals dispersed on the surface and ceria depends on the amount of silica on the support. The commercial sample was still characterized by two peaks which are caused by the different kind of cerium atoms on the surface, which is however narrower than that obtained with the dried catalyst. Besides, all the samples are characterized by a broaden peak in the range 500-520°C, where the reduction of surface Ce^{4+} atoms usually takes place in pristine CeO_2. Probably, this peak is due to the reduction of Ce^{4+} sites which are not directly in contact with gold.

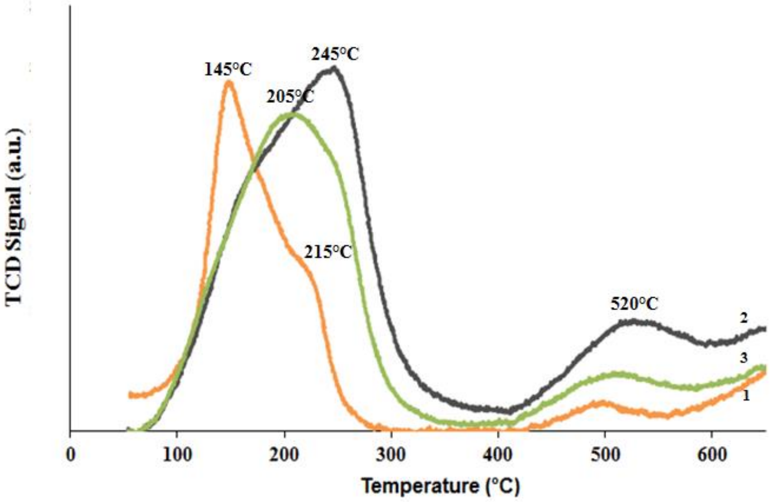

Figure 4-15 TPR profiles of the calcined catalysts: 1) Au-CeO_2, 2) Au-CeO_2_a, 3) Au-CeO_2_b.

4.4 Catalytic properties

Au-CeO_2_a and Au-CeO_2_b were used in the liquid phase oxidation of 5-hydroxymehtylfurfural (HMF) to 2,5-furandicarboxylic acid (FDCA) in order to compare the catalytic behaviour due to different SiO_2 content. The reaction follows the general pathway that has been already proposed in literature[15] and which is reported in Scheme 4-1.

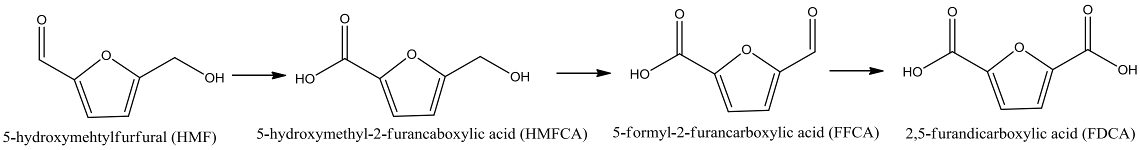

Scheme 4-1 General reaction pathway for HMF oxidation.

FDCA formation passes first through the formation of the first intermediate 5-hydroxymethl-2-furancarboxilic acid (HMFCA), resulted from the oxidation of the aldehydic group of HMF. HMFCA is slowly converted to 5-formylfurancarboxilic acid (FFCA) which reacts very fast to form FDCA. As a matter of fact, in our reaction conditions FFCA is never present in the final reaction mixture. Results obtained with the dried catalysts are reported in Figure 4-16, while those obtained with the calcined samples are shown in Figure 4-17. HMF conversion was always complete in each catalytic test; as a matter of fact, the strong basic environment promotes the conversion of this substrate.

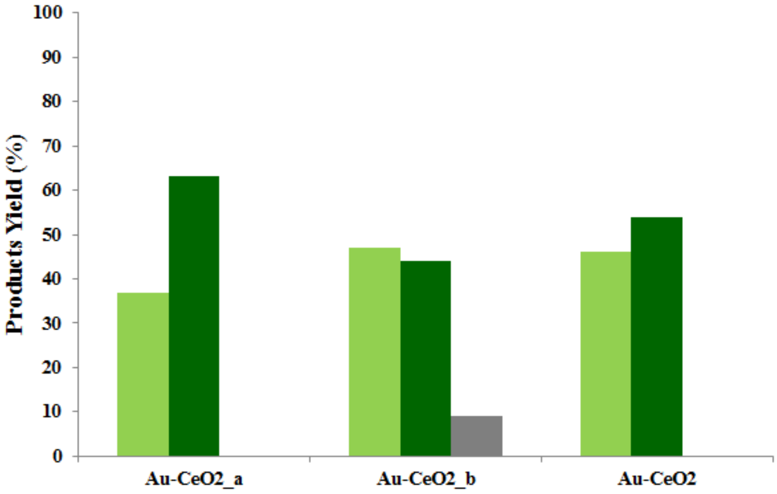

Figure 4-16 Products yield obtained with the dried catalysts. Reaction conditions: 70°C, 10 bar O_2, HMF:metal:NaOH molar ratio 1:100:4, 240 minutes. Results are given at total conversion of HMF. Legend: 🟩 FDCA yield, 🟩HMFCA yield, ■By-products yield.

Despite of the fact that the synthesized catalysts were shown to be very active for the oxidation of HMF, their performances were influenced by the presence of silica.

For this reason, sample Au-CeO$_2$_b has been found out to be more active than Au-CeO$_2$_a. In fact, the both had the same particle size (8nm), confirming that in this case the predominant effect is not Au nanoparticle diameter. Moreover, the catalytic activity of this dried mesoporous catalysts was very similar to the commercial one and FDCA yield was about 47% for both systems. Au-CeO$_2$_b sample gave exactly the same product distribution as the Au-CeO$_2$ except from the by-products formation. By-products yield is calculated considering the carbon loss obtained in each reaction and it is generally an indication of a catalyst that is not very active. In fact these by-products are formed from HMF degradation, which can only happen when the catalyst cannot suddenly catalyse its oxidation. HMF degradation is very common in the presence of a base even at ambient temperature and it is a parallel pathway of the oxidation process. In fact, if the oxidation is not catalysed, only by-products can be seen in the final dark brownish reaction mixture. Au-CeO$_2$_b was characterised by nanoparticles of the same dimensions as the Au-CeO$_2$ and this did not modify the catalytic activity. Using a high surface area cerium oxide with a mesoporous controlled morphology, it was not possible to observe an increase in the catalytic activity because the presence of silica had a negative predominant effect. Even with a ordered morphology, catalyst performance can be deeply influenced from gold-support interaction, which is still the most important feature in this kind of materials.

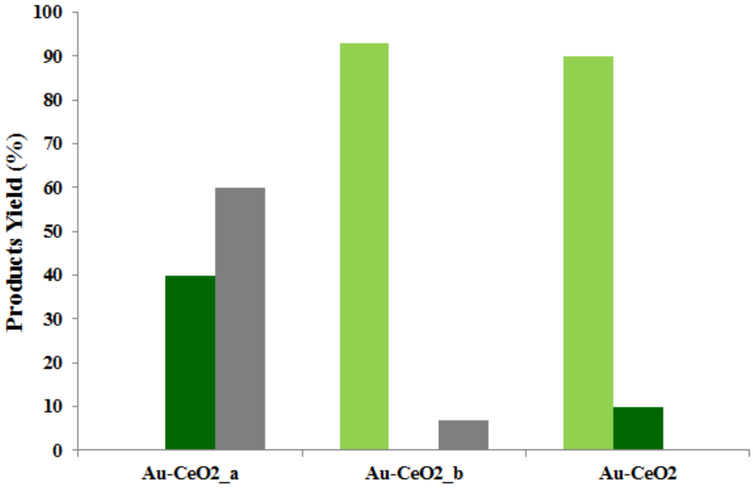

Figure 4-17 Products yield obtained with the calcined catalysts. Reaction conditions: 70°C, 10 bar O_2, HMF:metal:NaOH molar ratio 1:100:4, 240 minutes. Results are given at total conversion of HMF. Legend: ■ FDCA yield, ■HMFCA yield, ■By-products yield

The calcined catalysts (Figure 4-17) should display better performances since the capping agent that surrounded the nanoparticles (PVP) had been removed. In fact, a general increase in the FDCA formation can be observed, except for Au-CeO_2_a. For this sample, nanoparticle size must be taken into consideration. After the calcination process, in the presence of a greater amount of silica, gold sintering was favoured leading to a significant decrease in the catalytic activity. On the contrary, considering Au-CeO_2_b for which gold particle size remained unchanged even after calcination, FDCA yield increased. This behaviour has already been described in our previous work, for the Au-CeO_2 commercial sample[14]. The calcination aroused PVP removal, leaving the bare nanoparticle free to interact both with the substrate and with support. In literature it is reported that cerium oxide can be easily reduced releasing oxygen and creating superficial vacancies. This aspect is enhanced by the elimination of any substance that can interfere within metal and support such as PVP and SiO_2[16].

It has also been possible to correlate the catalytic activity with catalyst reduction temperature. Figure 4-18 shows that the catalysts which were able to produce a higher FDCA yield, were characterised by a lower reduction temperature. This behaviour could easily be correlated to the presence of silica on the support since it can avoid the proper metal-support interaction which is the most important aspect for these type of catalysts, decreasing CeO_2 redox properties and so its role in the oxidation reaction.

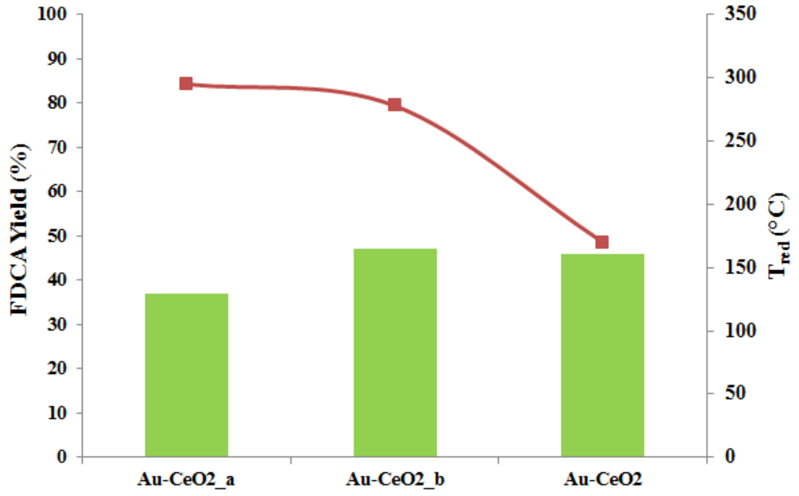

Figure 4-18 FDCA yield and reduction temperature for the prepared catalysts.Reaction conditions: 70°C, 10 bar O_2, HMF:metal:NaOH molar ratio 1:100:4, 240 minutes. Results are given at total conversion of HMF. Legend: 🟩 FDCA yield, ■HMFCA yield, ■By-products yield

Using the most active catalyst (Au-CeO_2_b dried), catalytic tests with different reaction time were performed. These tests were not carried on with the calcined sample, which gave better results because differences in the reaction mechanism could be more easily seen in the presence of a less active catalyst, which converts slowly the intermediates. The data reported in Figure 4-19 showed that the mechanism for FDCA formation is the one that is generally reported in literature (Scheme 4-1).

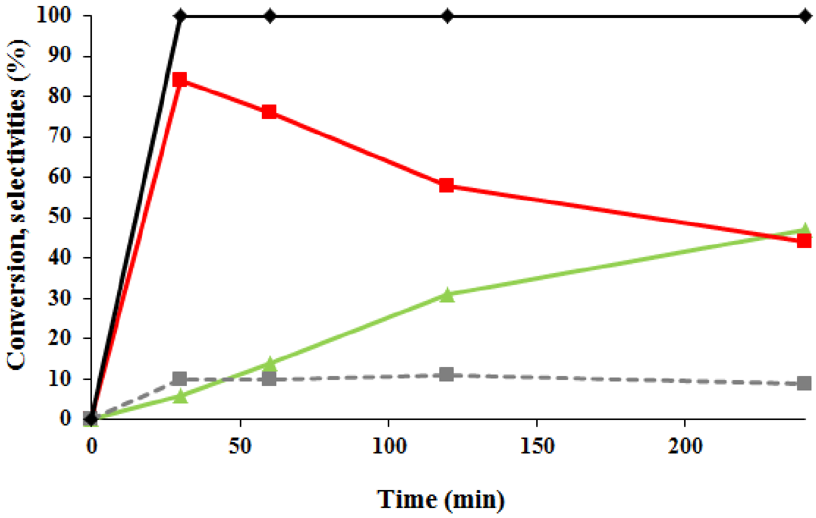

Figure 4-19 Time on line performed withAu-CeO_2_b dried 120°C. Reaction conditions: 70°C, 10 bar O_2, HMF:metal:NaOH molar ratio 1:100:4. Legend: ♦HMF conversion, ■ HMFCA selectivity, ▲FDCA selectivity, ■By-products selectivity.

HMF was suddenly converted and the formation of 2,5-furandicarboxilic acid (FDCA) passed through 5-hydroxymehtyl-2-furan carboxylic acid (HMFCA), which is a reaction intermediate since it decreased with time. These data suggested that HMF is rapidly transformed into HMFCA, while the rate determining step for FDCA production is the alcohol oxidation. Even though this catalyst was the most active, a certain amount of by-products was found out. The quantity of these by-products did not increase with time, confirming that they were formed by HMF degradation at the beginning of the reaction.

4.5 Conclusions

The reported procedure allowed the synthesis of cerium oxide with a controlled morphology, characterised by highly ordered mesoporous channels, small crystallites and high surface area. These materials were used as support for the preparation of Au supported catalyst and were found to be very active in the liquid phase oxidation of HMF to FDCA. However, the most predominant effect was due to the presence of silica, which remained on the surface of the oxide after the preparation of CeO_2 using SBA-15 as hard template. The positive effect which may be occurred in the presence of high surface area, small crystallites size, surface defects was overcome by the presence of SiO_2, which avoided a proper Au-support interaction.

---

[1] F. Ying, S. Wang, C.-T. Au S.-Y. Lai *Microporous Mesoporous Mater*. 142 (2011) 308-315.

[2] Y.J. Wang, J.M. Ma, M.F. Luo, P. Fang, M. He J. *Rare Earths* 25 (2007) 58-62.

[3] W. Yuejnan, M. Jingnieng, L. Mengfei, F. Ping, H. Mai J. *Rare Earths* 25 (2007) 58-62.

[4] F. Rouquerol, J. Rouquerol, K. Sing, Adsorption by powders and porous solids, Principles, metodolgy and applications, Academic Press, London (1999), ch. 13 pp. 440-441.

[5] Y. Wang, Y. Wang, J. Ren, Y. Mi, F. Zhang, C. Li, X. Liu, Y. Guo, Y. Guo, G. Lu, J. *Solid State Chem*. 183 (2010) 277–284.

[6] S. Abdollahzadeh-Ghom, C. Zamani, T. Andreu, M. Epifani, J.R. Morante, *Appl. Catal. B: Environ.* 108– 109 (2011) 32– 38.

[7] M. Blosi, S. Albonetti, S. Ortelli, A.L. Costa, L. Ortolani, M. Dondi *New J. Chem*. 38 (2014) 1401-1409.

[8] C. Gennequin, M. Lamallem, R. Cousin, S. Siffert, F. Aissi, A. Aboukais *Catal. Today* 122 (2007) 301-306.

[9] A. Trovarelli, G. Dolcetti, C. De Leitenburg, J. Kaspar, P. Finetti, A. Santoni, *J. Chem Soc. Faraday Trans*. 88 (1992) 1311-1319.

[10] S. Scirè, P.M. Riccobene, C. Crisafulli *Appl. Catal. B Environ.* 101 (2010) 109-117.

[11] S. Mandal, C. Santra, K. K. Bando, O. O. James, S. Maity, D. Mehta, B. Chowdhury *J. Mol. Catal. A: Chemical* 378 (2013) 47–56.

[12] S. Scirè, S. Minicò, C. Crisafulli, C. Satriano, A. Pistone *Appl. Catal. B Environ*. 40 (2003) 43-49.

[13] S. Scirè, P.M. Riccobene, C. Crisafulli *Appl. Catal. B Environ*. 101 (2010) 109-117.

[14] S. Albonetti, A. Lolli, V. Morandi, A. Migliori, C. Lucarelli, F. Cavani *Appl. Catal. B Environ*. 163 (2015) 520-530.

[15] S. E. Davis, B. N. Zope, R. J. Davis *Green Chem*. 14 (2012) 143-147.

[16] A. Corma, H. Garcia *Chem. Soc. Rev*. 37 (2008) 2096-2126.

CHAPTER 5

Study of the role of Pd-Au active phase composition in the reaction mechanism for 5-hydroxymethylfurfural (HMF) oxidation to 2,5-furandicarboxylic acid (FDCA)

Part of this chapter was previously published as *A. Lolli, S. Albonetti, L. Utili, R. Amadori, F. Ospitali, C. Lucarelli, F. Cavani "Insights into the reaction mechanism for 5-hydroxymethylfurfuraloxidation to FDCA on bimetallic Pd–Au nanoparticles" Appl. Catal. A: General (2014) doi:10.1016/j.apcata.2014.11.020*

5.1 Introduction

The aim of this part of the work is to synthesize monometallic (Pd, Au) and bimetallic (Pd-Au) nanoparticles in form of alloy and core-shell with different metal molar ratio, using the procedure previously described. $PdCl_2$ and $HAuCl_4$ have been used as metal precursors, PVP (polivinypyrrolidone) and β-D-glucose were used as stabilising and reducing agent respectively. Sodium hydroxide was added at the aqueous solution in order to promote the reducing power of the sugar. In Scheme 5-1 are reported the redox reaction that occur in nanoparticles formation.

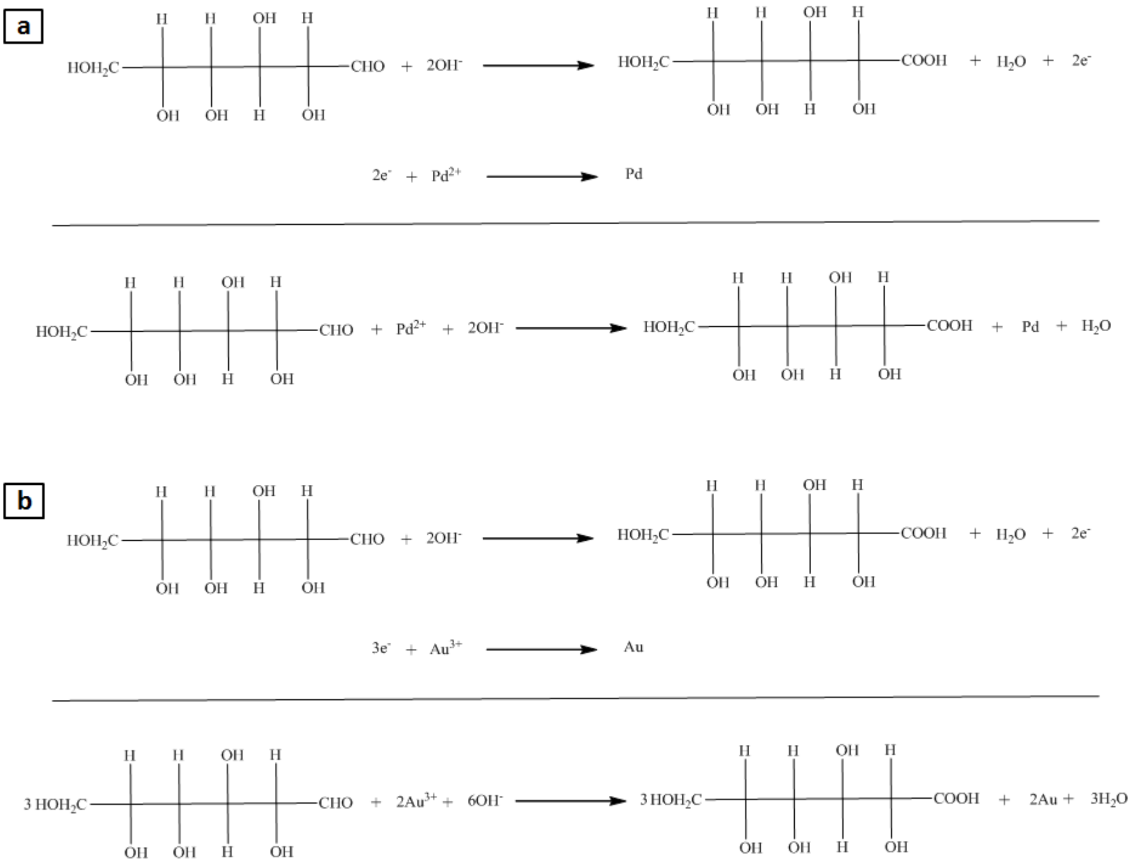

Scheme 5-1 Redox reaction for metal nanoparticles formation.

The preformed nanoparticles were characterised and then deposited onto TiO_2 using the incipient wetness impregnation method. The catalysts were dried, calcined at 300°C and characterised with different techniques (e.g. XRD, HRTEM, TGA-DTA and surface area measurements).

Catalytic tests for 5-hydroxymethylfurfural (HMF) oxidation to 2,5-furandicarboxylic acid (FDCA) have been carried on and the following aspects were carefully investigated:

- influence of active phase composition in the catalytic activity
- the effect of the calcination on the supported catalysts
- influence of the active phase morphology in the reaction mechanism .

5.2 Nanoparticles synthesis

Monometallic palladium and gold nanoparticles were synthesized with the procedure previously described. An aqueous solution containing PVP and NaOH was heated up to

95°C. Once the temperature had been reached, glucose together with the solution of metal precursor ($PdCl_2$ or $HAuCl_4$) was added and the resulted solution was vigorously stirred. Some drops of HCl were added to this solution in order to increase the solubility of the Pd salt. It took 2.5 minutes to reduce the metal cations and after this time the solution in the round bottom flask was cooled down.

Bimetallic nanoparticles in form of alloy and core-shell were also prepared. In order to prepare alloy metal nanoparticles, the metal salts were dissolved together and added after glucose in the heated round bottom flask. Since the amount of glucose, PVP and NaOH had been already optimised for gold[1,2,3], the quantity of reagents that was necessary to synthesize Pd nanoparticles was studied. For bimetallic particles, an average value was set for each palladium and gold content.

Core-shell nanoparticles were prepared from a monometallic system (Au or Pd), synthesized following the previous strategy, which had been used as seed for the nucleation of the second metal. In order to form the shell structure, the second metal was added once the nanoparticles of the first metal were formed. The quantity of organic reagents and base was the same as that used for bimetallic systems.

5.2.1 Monometallic nanoparticles

The necessary quantity of reagents to form gold nanoparticles had been already studied. In Table 5-1 the molar ratio between PVP, NaOH and glucose is reported.

Nanoparticles sol	$[PVP]/ [Au^{3+}]$	$[NaOH]/[Au^{3+}]$	$[Glucose]/[Au^{3+}]$
Au	2.75	8.00	2.00

Table 5-1 Molar ratio between PVP, NaOH, glucose and gold.

At first, palladium nanoparticles were synthesized using the same molar ratio as gold. However, the obtained results were not entirely satisfactory (Table 5-2 and Figure 5-1). The obtained sample (Pd-1) was too much polydisperse and three main peaks could be observed in the distribution curve. At this point, the optimization of the amount of reagents was studied. In order to synthesise small nanoparticles with a narrow Gaussian distribution, PVP and glucose amount were increased since palladium can be more difficultly reduced with respect to gold. In fact its reduction potential is 0.987 V, while that of gold is 1.498 V. In Table 5-2 the amount of reagents for each synthesis is reported together with Dynamic Light Scattering (DLS) analysis results of the obtained suspension. Polidispersive Index (PDI) is also reported because it shows how large the Gaussian curve is; the higher the PDI value, the broader the curve.

Sample	n_{PVP}/n_{Pd}	n_{NaOH}/n_{Pd}	$n_{Gluc.}/n_{Pd}$	$d_{average}$ (nm) and relative percentage	PDI
Pd-1	2.75	8	2	3 (3%); 12 (56%); 112 (20%); 331 (21%)	0.42
Pd-2	5.50	8	2	10 (79%); 164 (21%)	0.32
Pd-3	5.50	8	4	14 (65%); 342 (35%)	0.29

Table 5-2 Reagents/metals molar ratio, particle size distribution and PDI values from DLS analysis of each of the synthesised Pd suspensions.

Since nanoparticles obtained using the same reagent molar ratio as for gold synthesis (Pd-1) had a broad population distribution and big particle size, the amount of PVP was increased (Sample Pd-2) and a narrower population distribution was observed. In this case, particle size is mainly concentrated around the value of 10 nm, even though a second population was detected. Finally, the amount of glucose has been increased. This changement, did not bring any further improvements since the quantity of small nanoparticles decreased down to 65% in intensity and the bigger nanoparticles not only they increased in number, but also they almost doubled in size. DLS distribution curve are reported in Figure 5-1.

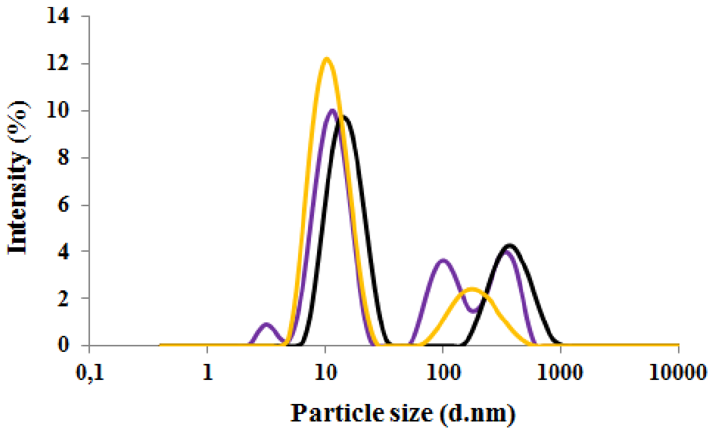

Figure 5-1 DLS analysis for preliminary optimisation of Pd nanoparticles synthesis express in Intensity. Legend: (-) Pd-1, (-) Pd-2, (-) Pd-3.

The reported curves highlighted the differences existing between the samples. Sample Pd-1 curve have four main peaks; it has to be said the a great amount of bigger nanoparticles is present since the area of the third and of the fourth peak is quite wide. Pd-2 and Pd-3 have similar results but for the latter the second peak is shifted to grater values.

The distribution curve express in volume is also reported (Figure 5-2) because the intensity distribution can emphasize the quantity of bigger particles at the expense of the smallest ones.

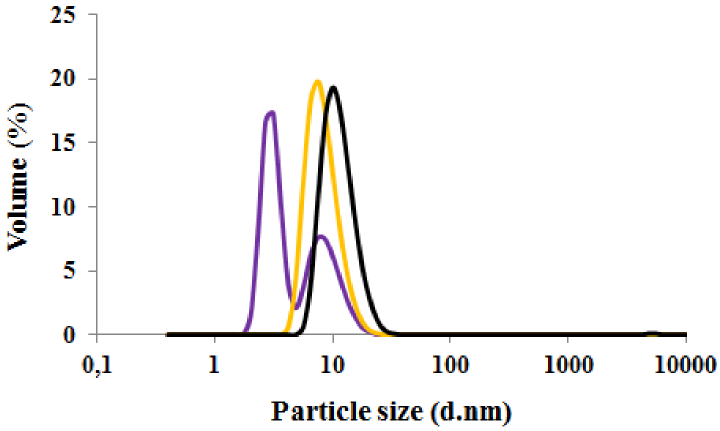

Figure 5-2 DLS analysis for preliminary optimisation of Pd nanoparticles synthesis express in Volume. Legend: (-) Pd-1, (-) Pd-2, (-) Pd-3.

As a result, this distribution curves are narrower and shifted to smaller particle size value. The narrowest curve and the smallest particle size value was obtained with sample Pd-2. Pd-3 was characterised by a low PDI but the Gaussian distribution peak maximum was shifted to a higher value. On the contrary, Pd-1 had a particle size distribution which gave very interesting results express in terms of volume. Particles seemed to be very small; however, taking into account the results expressed in terms of intensity, the population distribution range was very wide and the sample was not uniform.

To sum up, sample Pd-2 gave the best results in terms of particle size distribution and its amount of reagents was then utilised to prepare bimetallic sample.

5.2.2 Bimetallic Pd-Au nanoparticles

For bimetallic sample, the amount of reagents used for particles size synthesis was strictly correlated to the moles of Pd and Au that were present in each sample. In fact, several suspension with different molar metal ratio had been prepared. The list of the synthesised suspensions together with the molar ratio between the reagents and the metals are reported in Table 5-3.

Metal suspensions	mol % $[Pd^{2+}]$	mol % $[Au^{3+}]$	[PVP]/ $[Pd^{2+}]+[Au^{3+}]$	[NaOH]/ $[Pd^{2+}]+[Au^{3+}]$	[glucose]/ $[Pd^{2+}]+[Au^{3+}]$
Pd	100	0	5.50	8.00	2.00
Pd_3Au_1	75	25	4.81	8.00	2.00
Pd_1Au_1	50	50	4.12	8.00	2.00
Pd_1Au_3	25	75	3.44	8.00	2.00
Pd_1Au_6	14	86	3.14	8.00	2.00
$Au_6@Pd_1$	14	86	3.14	8.00	2.00
$Pd_1@Au_6$	14	86	3.14	8.00	2.00
Pd_1Au_9	10	90	3.02	8.00	2.00
Au	0	100	2.75	8.00	2.00

Table 5-3 Reagents/metals molar ratio for the prepared metal suspensions.

The molar ratio between reagents and the total metal content are given by the weighted average between the optimised ratio of the monometallic samples. The lowest possible quantity of HCl was used for $PdCl_2$ solubilisation in order to decrease the ionic strength of the solution. For samples with high gold content, no HCl was utilised since the pH of the solution had been already lowered by the dissolution of $HAuCl_4$.

After the preparation, nanoparticle suspensions were centrifuged in the Millipore filter and then the filtered solution was characterised by XRF analysis to check if the reduction of the metal precursors occurred. From this analysis, neither palladium nor gold were found, meaning that the reduction of metal cations was completed.

5.3 Catalysts preparation

Catalyst were prepared depositing onto TiO_2 the nanoparticles impregnation by means of the incipient wetness impregnation. Before impregnation, nanoparticle suspensions were concentrated using the Millipore filters, so that the excess of reagents could be easily removed. All catalyst were prepared using a metal loading of 1.5% and they were dried at 120°C overnight. Some of them were also calcined at 300°C to further remove the stabilising agent PVP that remains on the sample after the synthesis and to study the influence of the catalyst thermal treatment in the morphology of the catalysts and in the catalytic activity. Prepared catalysts are reported in Table 5-4.

Catalysts	Metal suspensions	Support	wt % total metal loading	wt % Pd	wt % Au
Pd-TiO_2	Pd	TiO_2	1,5	1,5	0
Pd_3Au_1-TiO_2	Pd_3Au_1			0,93	0,57
Pd_1Au_1-TiO_2	Pd_1Au_1			0,53	0,97
Pd_1Au_3-TiO_2	Pd_1Au_3			0,23	1,27
Pd_1Au_6-TiO_2	Pd_1Au_6			0,12	1,38
Pd_1Au_9-TiO_2	Pd_1Au_9			0,08	1,42
Au-TiO_2	Au			0	1,5

Table 5-4 Catalysts composition.

Supported catalysts with core-shell nanoparticles were not prepared; these suspensions were only used as unsupported to study the influence of the morphology in reaction mechanism during catalytic tests.

5.4 Characterization of preformed nanoparticles and supported catalysts[4]

The preparation of monometallic Pd and Au and bimetallic Pd-Au systems with different molar ratios and different morphologies led to the formation of small and stable particles. The resulting dispersions had a brownish colour, with intensity depending on the composition and Pd content.

All the synthesised suspensions were characterised with the DLS analysis. Not only were compared the samples in terms of intensity but also in terms of volume, which can reveal more efficiently the smallest fraction. Polydispersive Index (PDI) was also evaluated because it is an useful parameter that express the homogeneity of the system. The average diameters and PDI values are reported in Table 5-5. For bimodal samples at high Pd content relative percentage of each peak is shown.

Metal suspensions	$d_{average}$ Intensity (nm)	$d_{average}$ Volume (nm)	PDI
Pd	12 (79%) ; 198 (21%)	8	0.32
Pd_3Au_1	18 (82%) ; 280 (18%)	12	0.19
Pd_1Au_1	19 (83%) ; 348 (17%)	13	0.19
Pd_1Au_3	20	14	0.18
Pd_1Au_6	21	13	0.18
Au_6@Pd_1	24	19	0.25
Pd_1@Au_6	18	12	0.29
Pd_1Au_9	23	14	0.19
Au	21	16	0.20

Table 5-5 Average diameter, relative percentages and PDI of the prepared suspensions.

It is also possible to compare these sample with the following graphs, which show the average hydrodynamic diameters in intensity (Figure 5-3) and in volume (Figure 5-4).

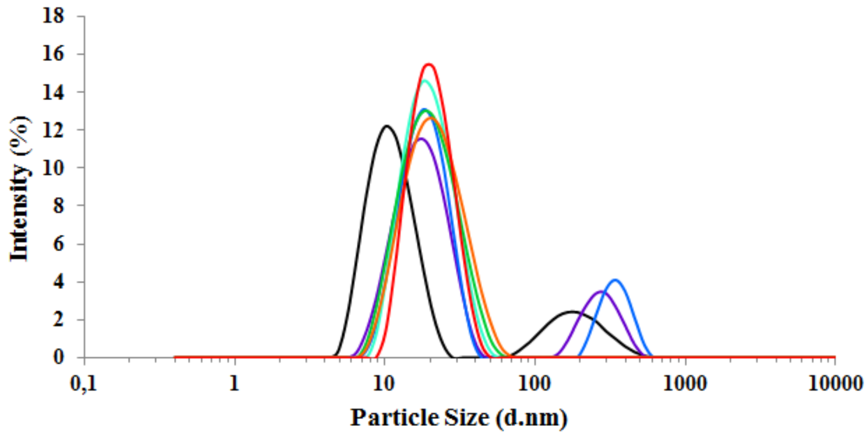

Figure 5-3 Average hydrodynamic diameter expressed in Intensity for the synthesised suspensions. Legend: (-) Pd, (-) Pd_3Au_1, (-) Pd_1Au_1, (-) Pd_1Au_3, (-) Pd_1Au_6, (-) Pd_1Au_9, (-) Au.

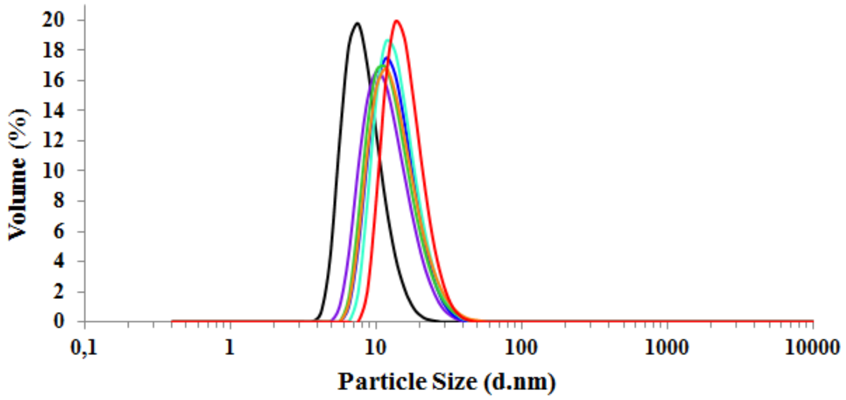

Figure 5-4 Average hydrodynamic diameter expressed in Volume for the synthesised suspensions. Legend: (-) Pd, (-) Pd_3Au_1, (-) Pd_1Au_1, (-) Pd_1Au_3, (-) Pd_1Au_6, (-) Pd_1Au_9, (-) Au.

Monometallic Pd-based sample and the suspensions at high Pd content (Pd_3Au_1, Pd_1Au_1) are characterised by a bimodal curve in intensity; however, the data reported quantifying the volume of particles in each sample show a narrow and monomodal distribution. This means that the number of aggregates is definitely scarce. PDI index has the same value for every sample except for the bimodal ones, thus indicating the presence of a population with a wide range size distribution. Core-shell sample with Pd in the core ($Pd_1@Au_6$) displayed an hydrodynamic diameter very similar to the Pd_1Au_6

alloy and smaller than the sample Au$_6$@Pd$_1$ (Figure 5-5 and Figure 5-6). As a matter of fact, nanoparticles with gold in the core have bigger dimensions; this is due to the fact that Au nanoparticles, used as nucleation seed, were greater than the Pd, leading to the formation of final particles with greater dimensions.

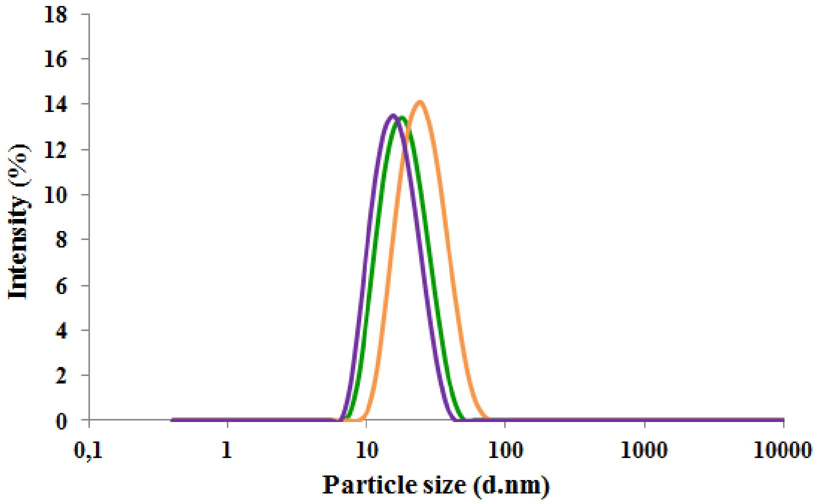

Figure 5-5 Average hydrodynamic diameter expressed in Intensity for the synthesised bimetallic suspensions with a metal molar ratio Pd:Au 1:6. Legend: Pd$_1$@Au$_6$ (-), Pd$_1$Au$_6$ (-), Au$_6$@Pd$_1$ (-).

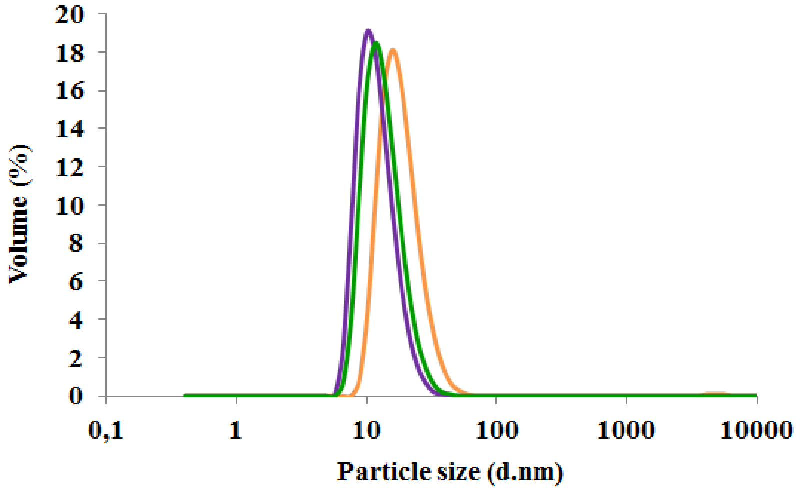

Figure 5-6 Average hydrodynamic diameter expressed in Volume for the synthesised bimetallic suspensions with a metal molar ratio Pd:Au 1:6. Legend: Pd$_1$@Au$_6$ (-), Pd$_1$Au$_6$ (-), Au$_6$@Pd$_1$ (-).

Moreover, the suspension were analysed by XRD in order to observed the different phases and to estimate crystallite size using the Debye-Sherrer equation. In Table 5-6 crystallite size are reported. They highlight the correlation between dimension and metal composition. The smallest sample are the monometallic Pd (4 nm) and those with high Pd content; increasing the gold content, an increase in the particle size could be observed. However, the sample with the biggest particle size is $Au_6@Pd_1$, because it is formed by Pd nucleation of preformed Au seeds which have an average dimension of 5 nm.

Metal suspensions	**Crystallite size (nm)**
Pd	4
Pd_3Au_1	4
Pd_1Au_1	5
Pd_1Au_3	5
Pd_1Au_6	5
$Au_6@Pd_1$	6
$Pd_1@Au_6$	5
Pd_1Au_9	5
Au	5

Table 5-6 Crystallite size for synthesised nanoparticles suspension.

In Figure 5-7 XRD the obtained diffractograms were reported. Every sample displayed a very broad peak, characteristic of samples with small particle size. This behaviour is emphasised for the monometallic Pd, confirming once again that it is the sample with the smallest particles size, as already seen for DLS analysis. The X-ray diffraction analysis of the bimetallic nanoparticles showed a significant shift of the main reflection when the Pd content was increased in the samples. The binary phase diagram of the Pd-Au system indicates that Au and Pd should exhibit a complete reciprocal solubility. Thus, the observed shift in the 2θ value is consistent with the incorporation of Pd into the Au lattice, indicating that bimetallic nanoparticles have a high degree of alloying.

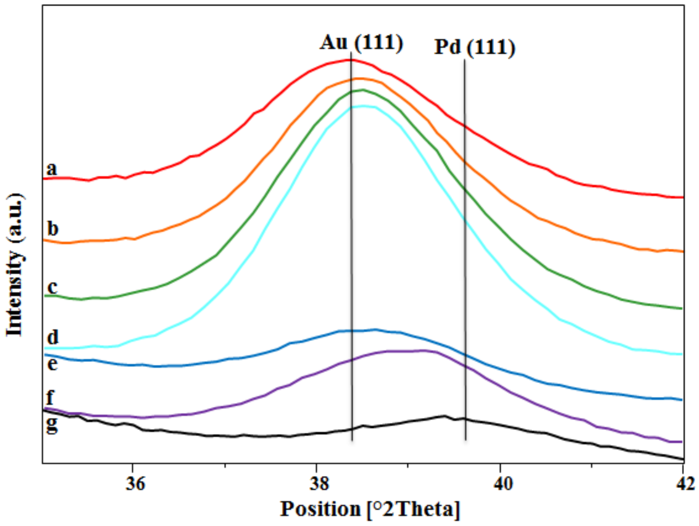

Figure 5-7 XRD diffractogram for the synthesised suspensions. Legend: a) Au, b) Pd_1Au_9, c) Pd_1Au_6, d) Pd_1Au_3, e) Pd_1Au_1, f) Pd_3Au_1, g) Pd.

As far as core-shell structure are concerned, a shift in the maximum peak from 38.4 to 38.7°2θ could be observed, passing from sample Au_6@Pd_1 to sample Pd_1@Au_6 because XRD analysis is particularly sensitive for the metal phase that is present in the core[5]. The maximum peak for the alloyed sample is 38.5°2θ, confirming that it has not the same crystalline structure as the core-shell samples.

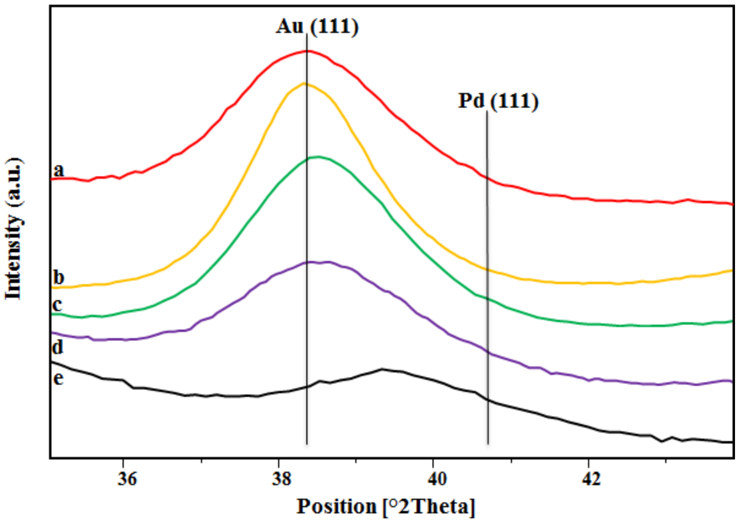

Figure 5-8 XRD diffractograms for comparison between the core-shell suspensions Au_6@Pd_1 (Au core) (b), Pd_1@Au_6 (Pd core) (d), the alloy Pd_1Au_6 (c) and the monometallic suspensions Au (a), Pd (e).

Lattice parameters were calculated for each sample and are reported in figure Figure 5-9 as a function of Pd content.

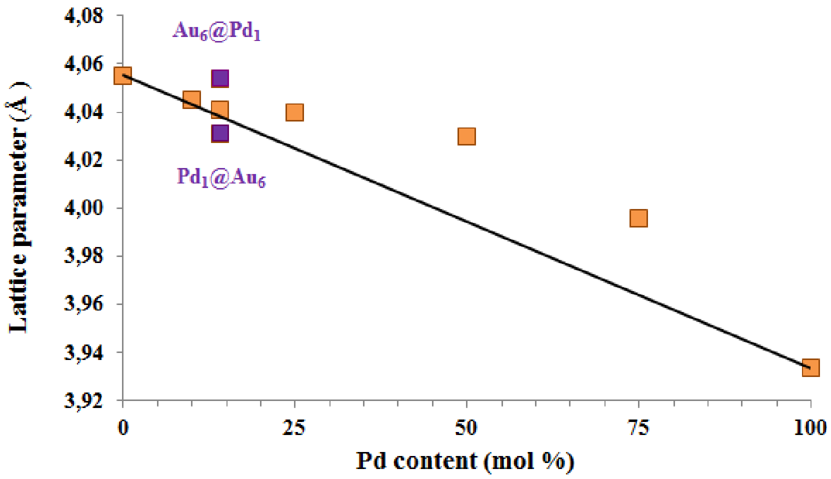

Figure 5-9 Lattice parameter as function of metal composition for the prepared samples.

From this graph it is evident that only samples with high gold content obey to the Vegard's law, that is to say that there is a linear correlation between metal composition and the crystalline structure of the cell. Pd_3Au_1 (75% mol Pd) Pd_1Au_1 (50% mol Pd) are very far from linearity; this may be due probably to a phase segregation. Au rich particle might be more homogeneous than Pd rich particle. Comparing the results obtained for core-shell particles, it is evident that they are not an homogeneous alloy, which may be an indication of the formation of a core-shell structure. Furthermore, lattice parameter of $Au_6@Pd_1$ is more similar to Au, while $Pd_1@Au_6$ lattice parameter clearly resembles to Pd because XRD results are more influenced by the core phase. It is also very interesting to notice that none of them is similar to the lattice parameter of the alloy.

Prepared sols were characterized by TEM. Some representative images and particle size distributions are presented in Figure 5-10 and Figure 5-11.

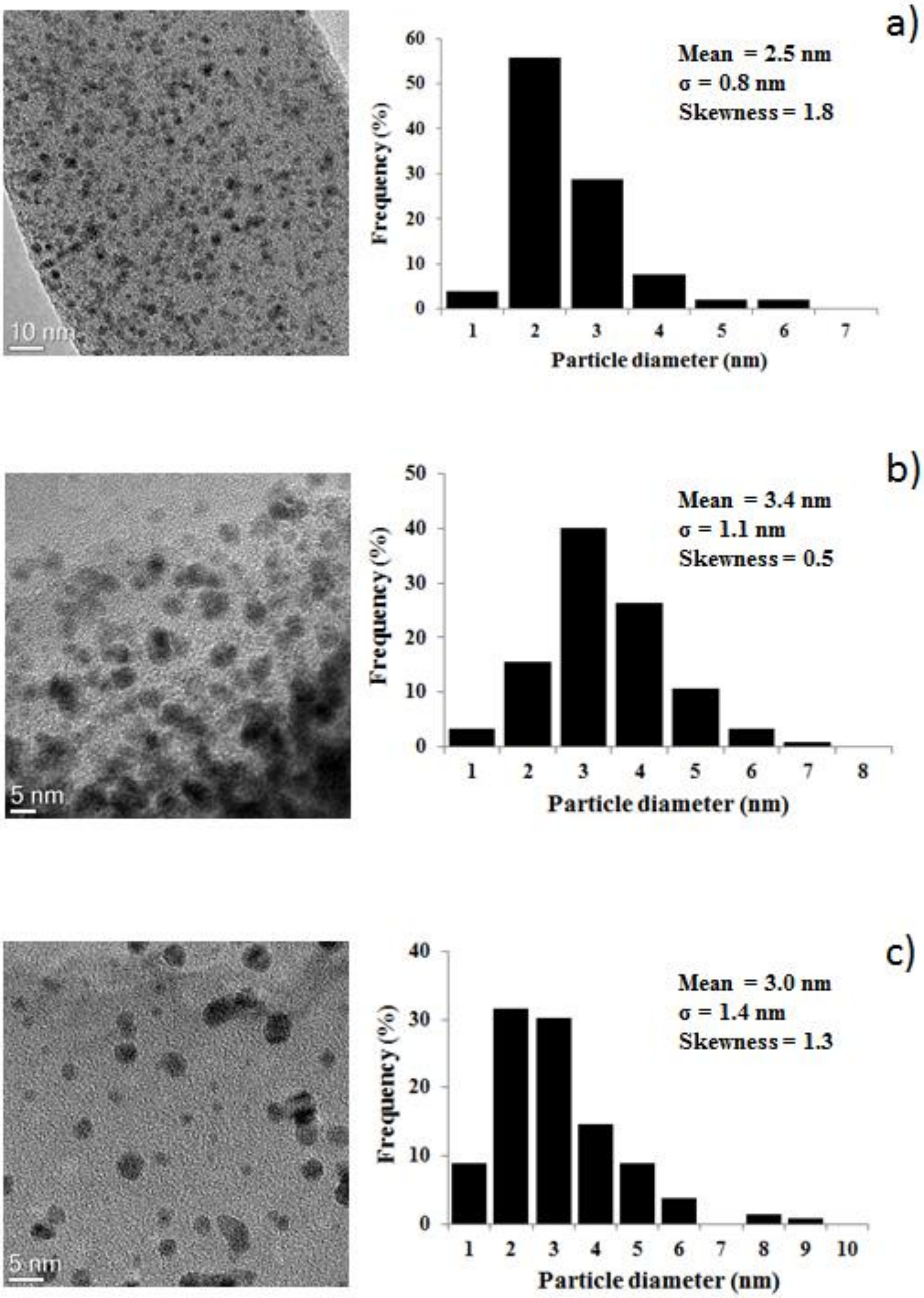

Figure 5-10 TEM images and particle size distributions of the samples: a) Pd, b)Pd_3Au_1, c)Pd_1Au_1.

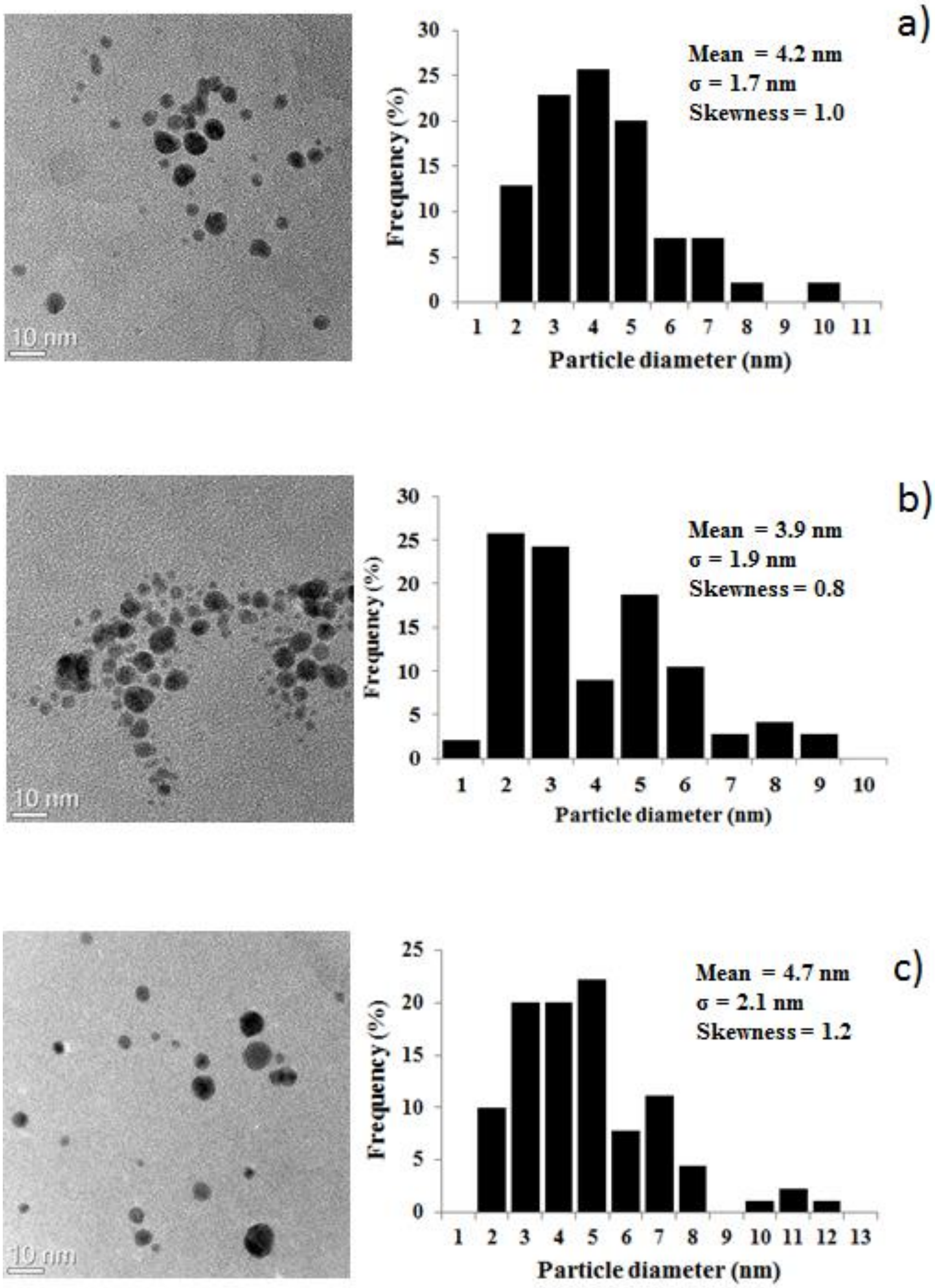

Figure 5-11 TEM images and particle size distributions of the samples: a) Pd_1Au_3, b) Pd_1Au_6, c) Au.

Nanoparticles showed a spherical morphology with a mean particle size ranging from 2.5 nm to 5 nm, depending on the sample composition (Table 5-7). Indeed, TEM measurements demonstrate that the Au sol has larger particles and a broader particle size distribution as compared to the Pd-Au and monometallic Pd sols, suggesting that the addition of Pd to Au decreases particle dimensions.

Metal suspensions	**d $_{XRD}$ (nm)**	**d $_{TEM}$ (nm)**
Pd	4	2.5
Pd_3Au_1	4	3
Pd_1Au_1	5	3
Pd_1Au_3	5	4
Pd_1Au_6	5	4
Au	5	5

Table 5-7 Average diameters of metallic nanosols estimated from XRD and TEM analysis.

PVP-protected Pd-Au nanoparticles with core-shell morphology were also synthesized, in order to investigate on the mechanism of FDCA formation when an active phase that preferentially expose either Pd or Au atoms is used. The microstructure of the prepared $Pd_1@Au_6$ (Pd core) and $Au_6@Pd_1$ (Au core) core-shell catalysts was investigated using TEM, STEM, and EDX to confirm the distribution of metals within bimetallic particles. Figures 3, 4 and 5 show TEM images and particle size distribution of core-shell and alloyed samples, and the compositional mappings of Pd and Au.

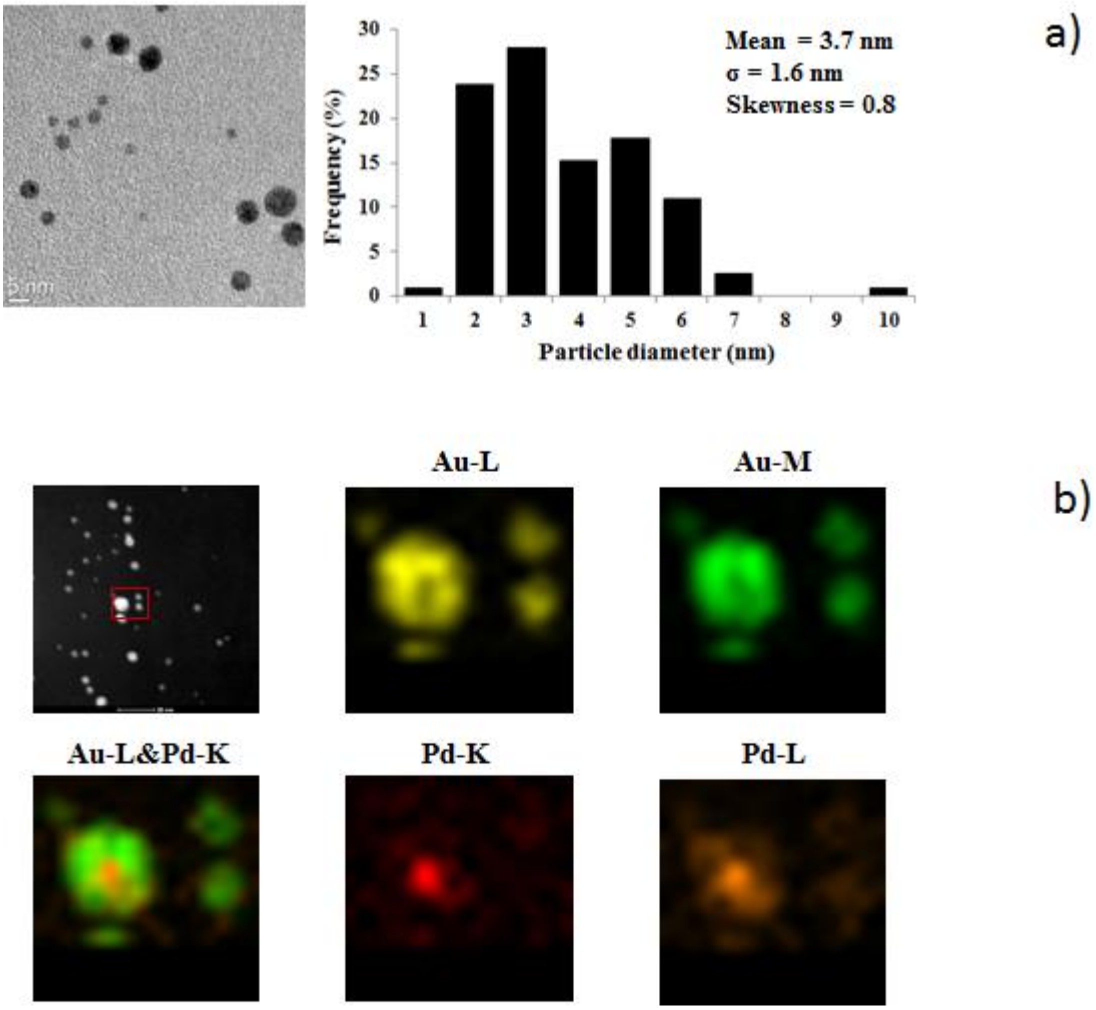

Figure 5-12 TEM images and particle size distribution of the $Pd_1@Au_6$ (Pd core) sample (a) and STEM image along with the corresponding Au-Lα, Au-Mα, Pd-Kα, Pd-Lα and (Au-L & Pd-K) elemental maps from the same area (b).

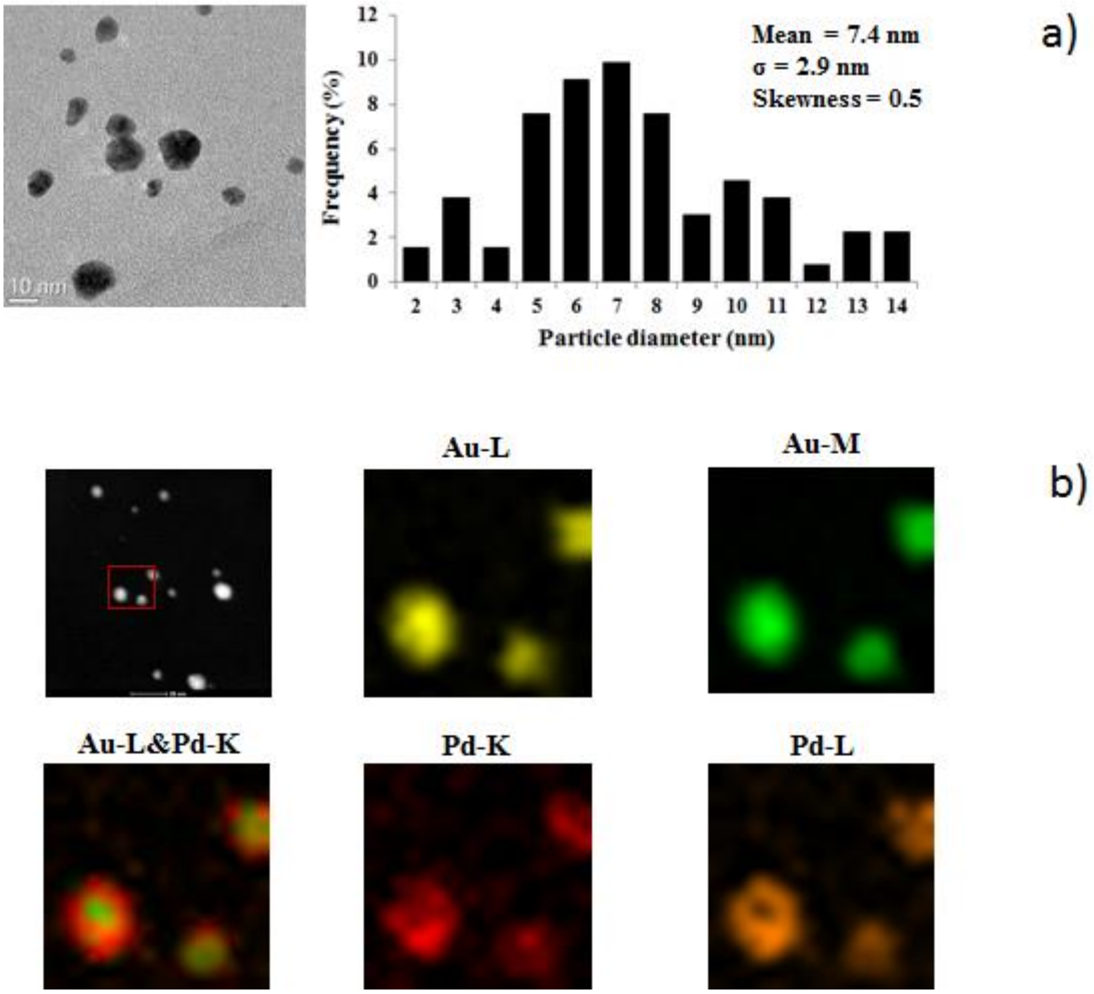

Figure 5-13 TEM images and particle size distribution of the sample $Au_6@Pd_1$ (Au core) (a) and STEM image along with the corresponding Au-Lα, Au-Mα, Pd-Kα, Pd-Lα and (Au-L & Pd-K) elemental maps from the same area (b).

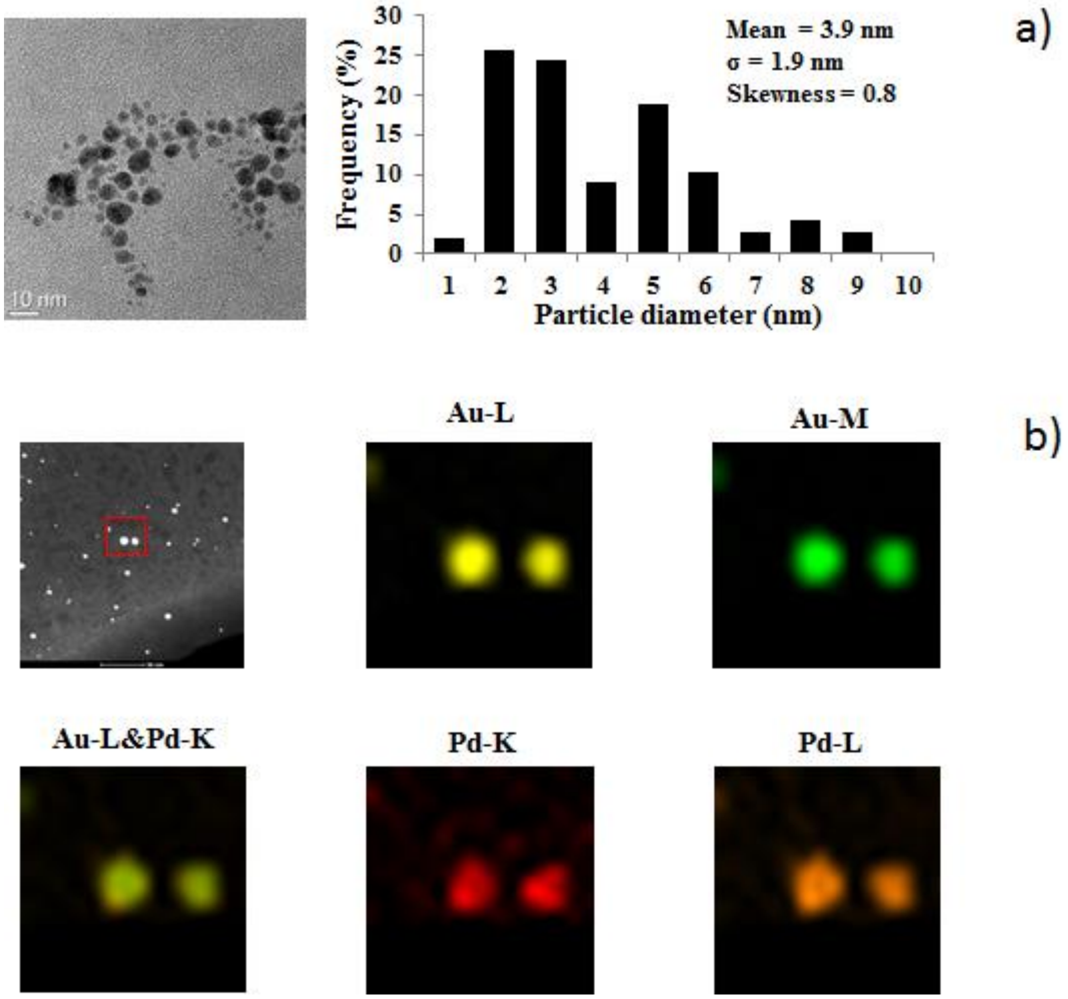

Figure 5-14 TEM images and particle size distribution of the Au_6Pd_1 (alloy sample) (a) and STEM image along with the corresponding Au-Lα, Au-Mα, Pd-Kα, Pd-Lα, and (Au-L & Pd-K) elemental maps from the same area (b).

Core-shell nanoparticles (Figure 5-12a and Figure 5-13a) have a sphere-like shape and their average diameter is 3.7 nm for $Pd_1@Au_6$ and 7.4 nm for $Au_6@Pd_1$, similar to the shape and dimension of the core metal. Alloy nanoparticles (Pd_1Au_6) have an average diameter of 3.9 nm. Figure 5-12b, Figure 5-13b and Figure 5-14b depict the HAADF-STEM elemental mapping of Pd, Au, and their overlapping for $Pd_1@Au_6$, $Au_6@Pd_1$ and Pd_1Au_6 nanoparticles; these results confirm that the particles show a morphology with either an Au-rich shell, or an Au-rich core or an Au-Pd alloy, respectively. Indeed, the signals of both Pd and Au can be clearly observed in elemental mapping images, indicating that both of the atoms are distributed within the whole nanoparticles with a concentration gradient which differed depending on the preparation method used. In the case of the $Pd_1@Au_6$ sample (Figure 5-12b), the analysis suggests that Pd was the predominant element in the inner part of nanoparticles, while Au was present on the particles surface. Conversely, with $Au_6@Pd_1$ (Figure 5-13b), the opposite trend was shown, further proving the predominance of Pd atoms on the surface of this catalyst. The low amount of Pd in the system prevented the formation of a well-defined shell; nevertheless, the Pd:Au ratio was clearly higher on the nanoparticle surface as compared to the core. Finally, in the case of Au_6Pd_1 nanosol (Figure 5-14b) the complete overlapping of Pd and Au signals was shown, which confirms the presence of an homogeneous alloy.

All the synthesized nanoparticles, except for the core-shell systems, were deposited on TiO_2 by incipient wetness impregnation, with a metal loading of 1.5 wt.%. BET analysis (Table 5-8) showed a decrease of the surface area value when the Pd content was increased. This effect was probably due to the higher organic content, necessary for the synthesis of small and stable Pd particles. Indeed, a greater amount of PVP may occlude the porosity of the support, when the suspension is deposited over the surface, as also shown for the Au-Cu system[6,7].

Catalyst	**Total metal loading (wt.%)**	**Pd (wt.%)**	**Au (wt.%)**	**Molar ratio Pd:Au**	**Surface Area (m^2/g)**
$Pd-TiO_2$	1.5	1.5	0	-	72
$Pd_3Au_1-TiO_2$	1.5	0.93	0.57	3	73
$Pd_1Au_1-TiO_2$	1.5	0.53	0.97	1	78
$Pd_1Au_3-TiO_2$	1.5	0.23	1.27	0.33	79
$Pd_1Au_6-TiO_2$	1.5	0.12	1.38	0.16	79
$Pd_1Au_9-TiO_2$	1.5	0.08	1.42	0.11	83
$Au-TiO_2$	1.5	0	1.5	-	82

Table 5-8 Structural parameters and chemical composition Au and Pd-Au supported on TiO_2.

All supported catalysts, both after drying and calcination, were characterized by XRD analysis. As an example, **Errore. L'origine riferimento non è stata trovata.** shows the XRD pattern of both dried and calcined $Pd_1Au_6-TiO_2$ sample; however, the information obtained from this analysis on the structure of the metallic phase are poor and no clear indication can be obtained from these data.

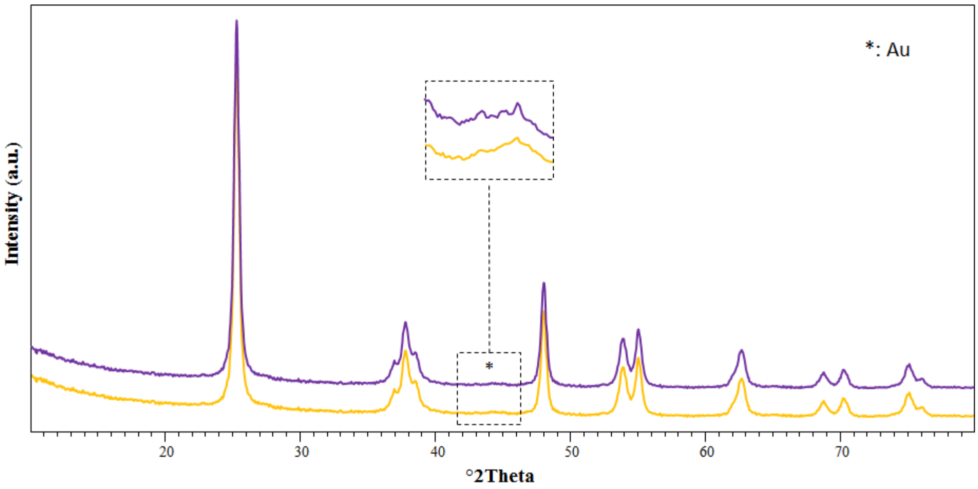

Figure 5-15 XRD pattern of Pd_1Au_6-TiO_2 dried (-) and calcined at 300°C (-) samples.

The TEM analysis of selected supported nanoparticles and their size distribution histograms are shown in Figure 5-16 (dried catalysts) and Figure 5-17 (calcined 300°C catalysts). The measurement of randomly chosen nanoparticles over the support confirmed that particles with a greater Au content had larger dimensions than Pd particles. Nevertheless, the metal phase was still characterized by dimensions between 3.4 nm and 6.9 nm, thus suggesting that the impregnation of metal sols on the TiO_2 support (Figure 5-16) and calcination (Figure 5-17) generates a high metal dispersion and does not significantly affect the active phase dimension. This behaviour is also showed in Table 5-9, where the average particle size of metal nanosols and supported catalyst are displayed.

Metal active phase	Type of sample	Average particle size (nm)
Pd	Sol	2,5 ± 0,8
	Dried catalyst	3 ± 1
Pd_1Au_1	Sol	3 ± 1
	Dried catalyst	5 ± 2
	Calcined 300°C catalyst	6 ± 1
Pd_1Au_6	Sol	4 ± 2
	Dried catalyst	6 ± 2
	Calcined 300°C catalyst	7 ± 2

Table 5-9 Average particle size of metal nanosol, dried and calcined catalysts for samples Pd, Pd_1Au_1 and Pd_1Au_6.

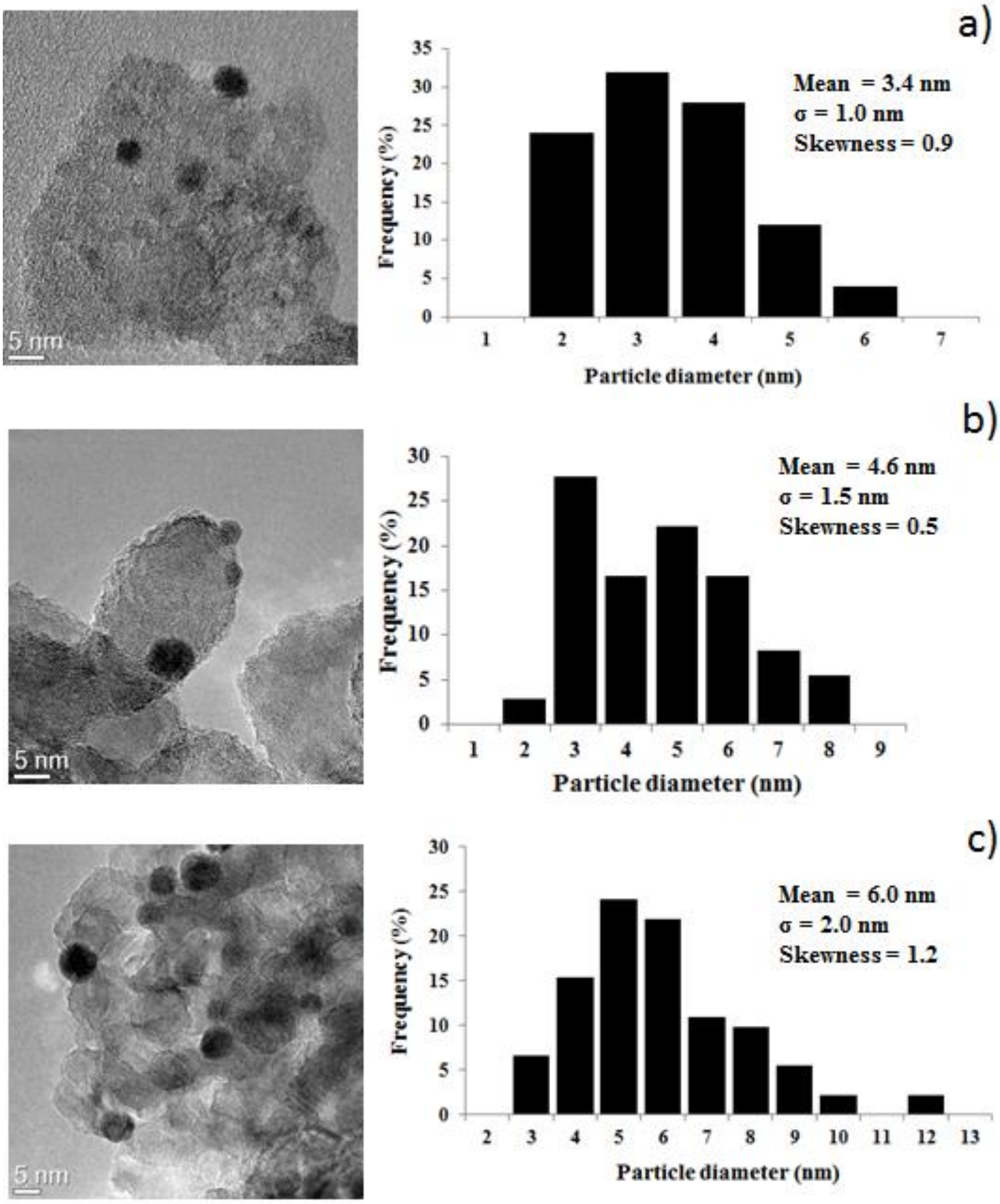

Figure 5-16 HR-TEM images and particle size distribution of the dried catalysts: a) Pd-TiO_2; b) Pd_1Au_1-TiO_2; c) Pd_1Au_6-TiO_2.

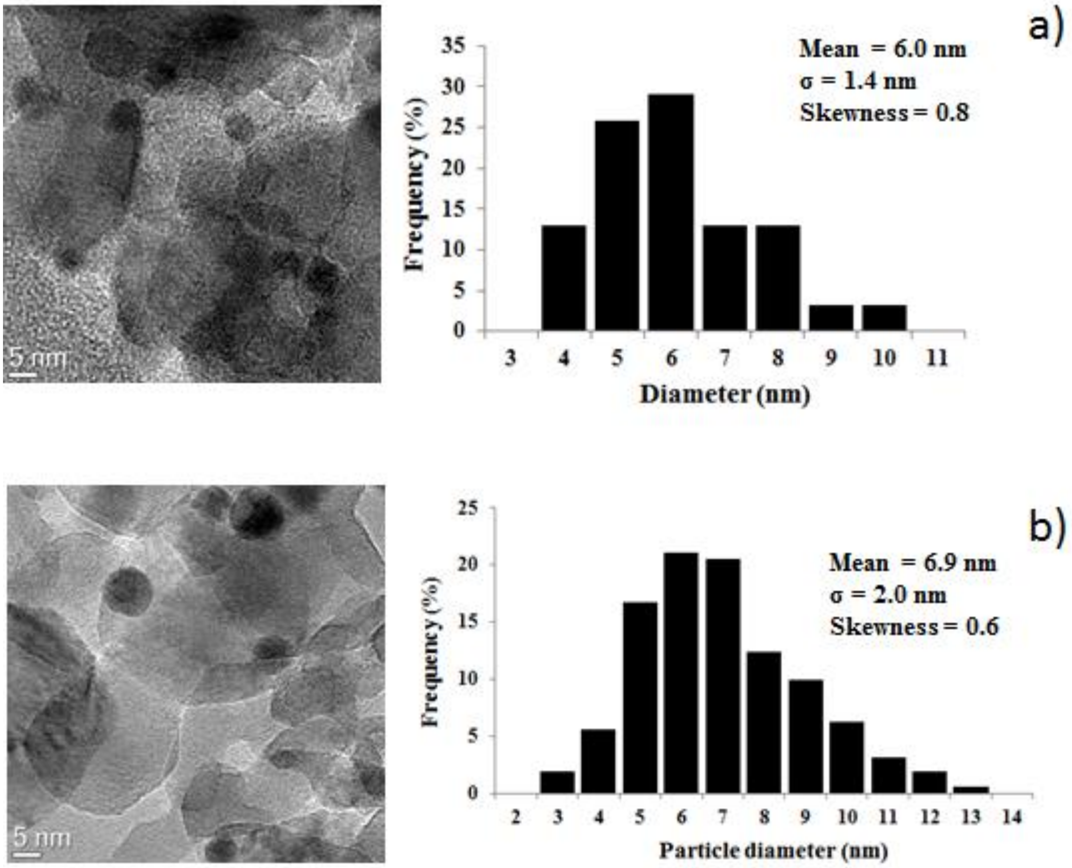

Figure 5-17 HR-TEM images and particle size distribution of the calcined catalysts: a) Pd_1Au_1-TiO_2; b) Pd_1Au_6-TiO_2.

Owing to the fact that the calcination process did not lead to particle aggregation, it could be considered as a very important step for catalyst preparation since it allows PVP removal. In fact, after deposition onto the support, nanoparticles are still surrounded by the stabilizing agent which can obstruct an efficient interaction between metal and the substrate, leading to a decrease in the catalytic activity. Therefore, PVP removal may favour catalyst performance. The thermal behaviour of PVP was studied in air by means of TGA (Thermogravimetric Analysis) and DTA (Differential Thermal Analysis) analysis; the obtained data are reported in Figure 5-18. From the graph below it is possible to observe the severe weight loss and the exothermicity due to organic combustion in the range 400-500°C. In addition, some catalyst were also analysed to see if there is any difference in the combustion behaviour for system with different active phase (Pd-TiO_2, Pd_1Au_1-TiO_2, Pd_1Au_6-TiO_2, Au-TiO_2). In Figure 5-19 TGA analysis for the selected catalyst are shown.

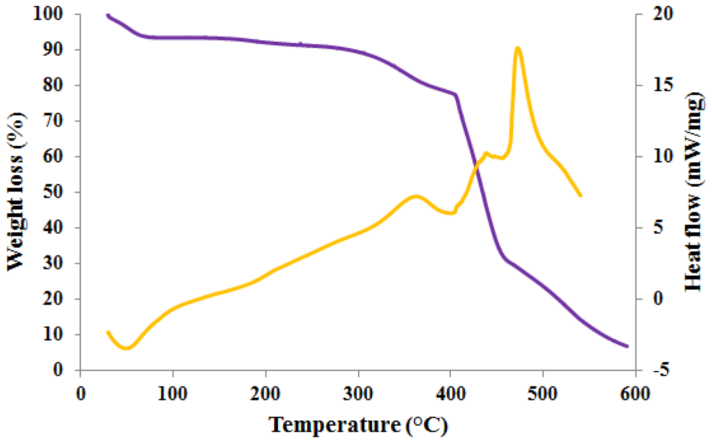

Figure 5-18 TGA (-) and DTA (-) analysis of PVP (polyvinylpyrrolidone).

For every sample, the weight loss that occurred at around 100°C is due to the release of water absorbed onto the catalysts. On the other hand, the bigger weight loss which took place at a temperature very close to 300°C is produced by the organic compounds (PVP and glucose) which remain from nanoparticles synthesis. The results underlined that the weight loss increase with the Pd content. This is caused by the fact that it had been necessary to use more PVP during the synthesis of palladium and palladium based nanoparticles.

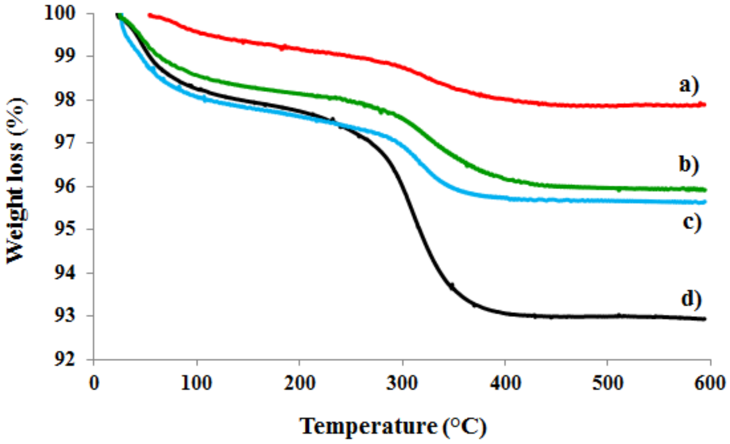

Figure 5-19 TGA analysis of dried supported catalysts. Legend: a) Au-TiO_2, b) Pd_1Au_6-TiO_2, c) Pd_1Au_1-TiO_2, d) Pd-TiO_2.

In Table 5-10 are reported the temperature at which the maximum weight loss occurred and the percentage value of the weight loss for each sample. It is evident that Pd-TiO_2 weight loss is nearly four times than that of Au-TiO_2. Moreover, this excess of organic compound may be due to the use of smaller cellulose filters (30 kDa) if compared to those used for gold based catalysts (50 kDa), which can keep together with the particles more organic molecules. In addition, a small shift of the maximum temperature coul be observed, moving from Pd to Au catalyst. This means that PVP combustion can be influenced by type of metal and may be favoured by the presence of Pd atoms.

Catalyst	Temperature (°C)	Weight loss (%)
Pd-TiO_2	308	5,0
Pd_1Au_1-TiO_2	316	2,2
Pd_1Au_6-TiO_2	318	1,9
Au-TiO_2	317	1,3

Table 5-10 Weight loss for analysed catalysts.

DTA analysis confirmed the trend previously described; the exothermicity increase with the palladium content. From the graph reported in Figure 5-20 DTA analysis of dried supported catalysts. Legend: a) Au-TiO_2, b) Pd_1Au_6-TiO_2, c) Pd_1Au_1-TiO_2, d) Pd-TiO_2.Figure 5-20 the maximum temperature shift could be easily observed. However, both metals can strongly promote PVP thermal combustion because PVP thermal analysis showed (Figure 5-18) a degradation temperature in the range 400-450°C.

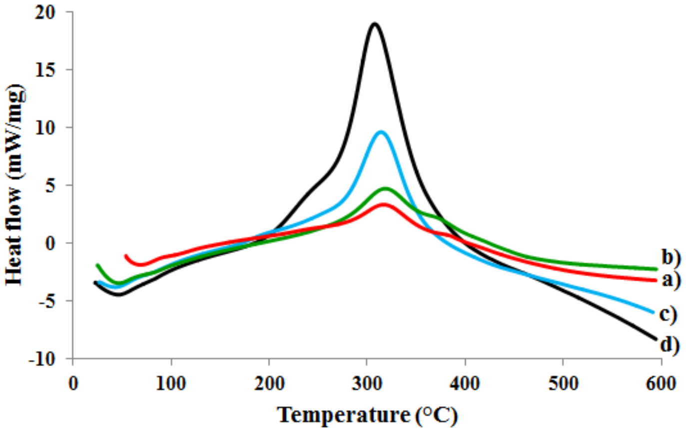

Figure 5-20 DTA analysis of dried supported catalysts. Legend: a) Au-TiO_2, b) Pd_1Au_6-TiO_2, c) Pd_1Au_1-TiO_2, d) Pd-TiO_2.

5.5 Catalytic Tests

The synthesis of FDCA by means of HMF oxidation has been widely studied over the past two decades using different reaction conditions and catalysts[8,9]. Scheme 1 shows the general HMF oxidation pattern.

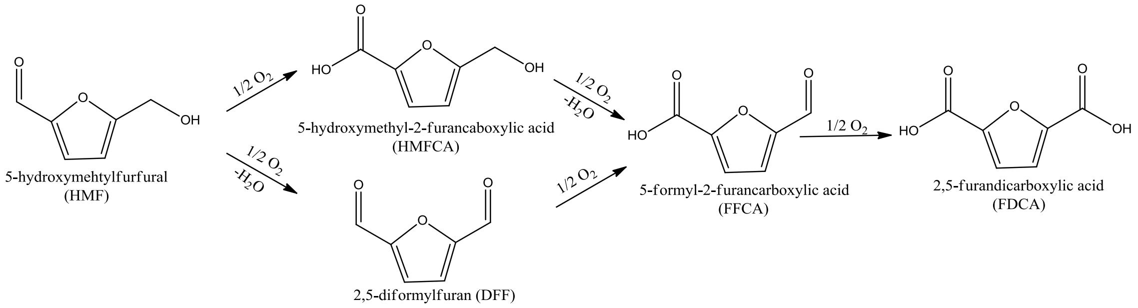

Scheme 5-2 General reaction network for HMF oxidation.

FDCA is usually produced in two stages: the carbonylic group is first oxidized to the carboxylic moiety, producing 5-hydroxymethyl-2-furancarboxylic acid (HMFCA); then, typically, the oxidation of the hydroxymethyl group in HMFCA yields FDCA through 5-formyl-2-furancaboxylic acid (FFCA) as the intermediate[10]. Furthermore, sometimes the formation of 2,5-diformylfuran (DFF) was also observed, mainly in the absence of an added base and with metals other than Au[11].

5.5.1 Effect of catalysts compositionErrore. Il segnalibro non è definito.

Both monometallic and bimetallic systems were tested as catalysts for HMF oxidation. First, the reaction was carried out on monometallic Au and Pd systems, in basic water, at different temperatures and with different NaOH contents (Table 5-11).

The results indicate that the Pd-TiO_2 catalyst is less active than Au-TiO_2 in FDCA formation. Indeed, with both catalysts and under similar reaction conditions, most of the reagent was transformed into HMFCA, but Pd-TiO_2 produced a slightly lower amount of FDCA than Au-TiO_2 (selectivity 8% vs. 12%). Moreover, FDCA yield remained almost unchanged when the amount of NaOH in the reaction was increased with Pd-TiO_2, whereas the Au-TiO_2 activity was significantly influenced by the base amount. This trend confirms previous results reporting that Pd catalysts are less affected by NaOH concentration than Au catalysts[12]. However, the presence of the base is fundamental also when Pd is used, since in neutral conditions there was no reaction at all. This finding is consistent with previous works[13,14] on metal-supported catalysts, in which the presence of a base is reported to facilitate the deprotonation of alcohol and to promote its conversion into the aldehyde.

Catalyst	NaOH/HMF molar ratio	T (°C)	HMF Conv (%)	HMFCA Sel. (%)	FDCA Sel.(%)	FFCA Sel. (%)	By-products Sel. (%)
TiO_2	2	70	74	20	0	0	80
	4	70	100	10	0	0	90
Pd-TiO_2	0	70	0	0	0	0	0
	0.5	70	54	100	0	0	0
	2	70	100	92	8	0	0
	4	70	100	92	8	0	0
	2	90	100	91	9	0	0
Au-TiO_2	2	70	100	86	12	2	0
	4	70	100	81	19	0	0
	2	90	100	78	13	9	0

Table 5-11 Comparison of the selectivity to the reaction products obtained with Pd-TiO_2 and Au-TiO_2 catalysts in different reaction conditions. Reaction time 240 min, O_2 pressure 10 bar. HMF:Metal molar ratio 1:0.01.

In order to gain information on the reaction network, the effect of reaction time in HMF oxidation was investigated. Figure 5-21 shows HMF conversion and products selectivity plotted in function of time, for the Pd-TiO_2 catalyst.

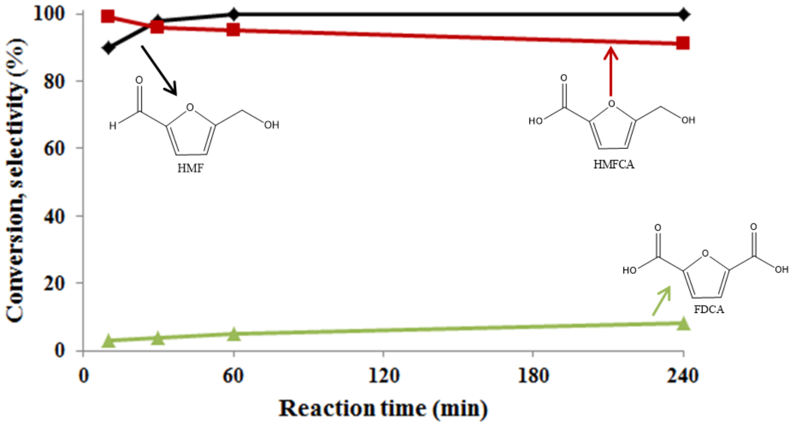

Figure 5-21 Reaction profile for oxidation of HMF on Pd-TiO_2 (dried at 120°C). Reaction conditions: temperature 70°C, O_2 pressure 10 bar, HMF:Metal:NaOH molar ratio 1:0.01:2. Legend: ♦ HMF conversion, ■ HMFCA selectivity, ▲ FDCA selectivity.

HMFCA formation was very fast under the conditions used; indeed, the complete transformation of HMF to HMFCA was obtained after just 30 min reaction time. However, the catalyst was very poorly active for the subsequent oxidation of HMFCA into FDCA, in fact yields to both HMFCA and FDCA were almost unchanged between 30 and 240 min time, which indicates that Pd is unable to promote the oxidation of HMFCA. Similar results were reported by Villa et al.[15] using Pd/C catalysts; these authors ascribed the observed trend to sample deactivation. Conversely, in our study the deactivation of the Pd-TiO_2 catalyst may be ruled out, since the further addition of HMF after 1 h led to complete HMF conversion and identical selectivity to both HMFCA and FDCA, as shown in the previous experiment.

As a general observation it must be underlined that, under the basic environment used, the less active catalysts also led to the formation of by-products due to HMF degradation[16]. However, for the Pd catalyst the immediate transformation of HMF avoided its degradation, while very pure HMFCA was obtained. This result confirms the need to quickly transform HMF so removing it from the basic reaction medium in order to produce pure FDCA, since the coloured degradation products originated from HMF and not from HMFCA[17,18]. The increase of the reaction temperature, from 70 to 90°C, did not succeed in enhancing Pd-TiO_2 catalytic activity (Table 5-11), in contrast with what previously observed with Au and Au-Cu catalysts (Table 5-11)[7].

The catalytic behaviour of bimetallic Pd-Au catalysts was significantly different from that of monometallic systems; in fact, the distribution of products was strongly affected by the Pd:Au atomic ratio (Figure 5-22). In particular, the results clearly show the presence of a synergic effect due to the presence of the two metals.

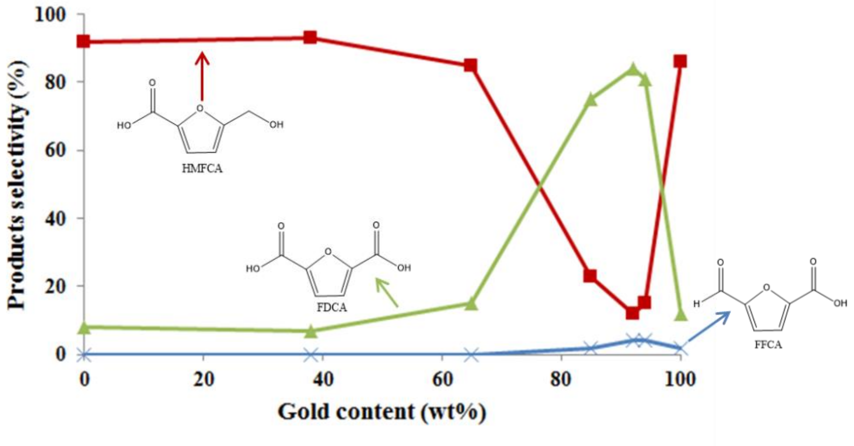

Figure 5-22 Product selectivity on catalysts at different Pd:Au atomic ratios. Results are given at total conversion of HMF. Reaction conditions: temperature 70°C, O_2 pressure 10 bar, reaction time 240 min, HMF:Metal:NaOH molar ratio 1:0.01:2. Legend: ■ HMFCA, ▲ FDCA, X FFCA.

An increase in FDCA selectivity was observed by increasing the Au content, until a maximum value was shown at a Pd:Au atomic ratio equal to 1:6 (Pd 8 wt.%, Au 92 wt.%). A further increase of the Au content resulted in a decrease of FDCA selectivity, although all catalysts with high Au content (Pd_1Au_3-TiO_2, Pd_1Au_6-TiO_2 and Pd_1Au_9-TiO_2) were more efficient in the formation of this product. These results confirm the recent data reported by Prati and co-workers – who used Pd-Au nanoparticles supported on activated carbon[15] for glycerol and alcohol oxidation. Therefore, a small quantity of Pd seems to be adequate to significantly change the electronic properties of Au and enhance the catalytic activity in alcohol oxidation. The characterization of these catalysts revealed both similar nanoparticle dimensions (in the range 4-6 nm) and homogeneous dispersion over the TiO_2 support; therefore an effect of metal particles size on the reactivity seems to be unlikely. Conversely, samples with low Pd content presented an alloy structure, and this morphology seems to be the desired one for producing effective catalysts.

As a preliminary conclusion of these reactivity experiments, we can state that the distribution of products in the oxidation of HMF was strongly affected by catalyst composition; Pd-TiO_2 was poorly selective to FDCA because of its inability to oxidise HMFCA. Conversely, FDCA yield was strongly increased by incorporating small amounts of Pd in Au nanoparticles.

5.5.2 Mechanistic investigations

In order to gain further insight on the reaction mechanism, the reactivity of the most active catalyst, Pd_1Au_6-TiO_2, was thoroughly investigated.

Figure 5-23 shows the HMF conversion and product selectivity in function of reaction time, with the catalyst dried at 120°C.

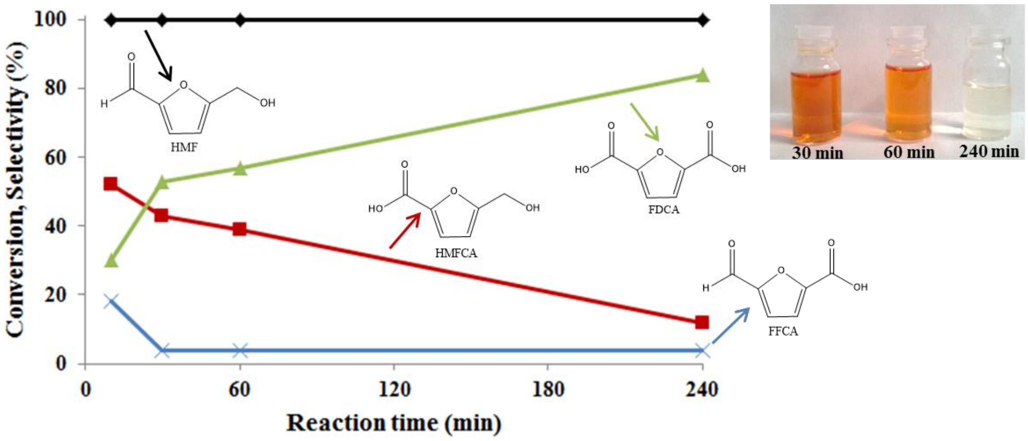

Figure 5-23 HMF conversion and product selectivities as a function of time on Pd_1Au_6-TiO_2 sample dried at 120°C. Reaction conditions: temperature 70°C, O_2 pressure 10 bar, HMF:Metal:NaOH molar ratio 1:0.01:2. Legend: ♦ HMF conversion, ■ HMFCA selectivity, ▲ FDCA selectivity, X FFCA selectivity. The insert shows the final mixture at different reaction times.

On this sample the conversion of HMF was always complete. During the first 10 min, the major product was HMFCA (50% selectivity), with lower selectivity to both FDCA and FFCA. The latter product was detected during the initial stage of the reaction, whereas the selectivity to FDCA increased with time. Results indicate that the reaction network consists of the direct and rapid transformation of HMF into HMFCA, while the rate-determining step for FDCA production is the oxidation of the hydroxymethyl group in HMF. Other by-products, such as DFF, were not detected, and after 4 h of reaction time, a FDCA selectivity of 85% was shown. The observed path reflects the reaction scheme usually reported in literature using basic conditions, as it was also observed for Au-TiO_2[6].

Since the catalysts used were synthesized by using PVP-stabilized sols, Pd_1Au_6-TiO_2 was thermally treated to examine the effect of PVP removal. Previous results[6,7] demonstrated that the PVP over Au and Au-Cu/TiO_2 catalysts did not prevent their activity in HMF oxidation. Nevertheless, it has been reported that the ligands chemisorbed on the nanoparticles may decrease catalyst activity[19,20]; therefore, further experiments were conducted in order to clarify this point.

To obtain clean metallic species, the Pd_1Au_6-TiO_2 sample was calcined at 300°C[16]. TEM results (Figure 5-16 and Figure 5-17) demonstrate that the Pd-Au-supported nanoparticles almost retained their size (the mean particle size was 7 nm, versus 6 nm obtained with the dried sample). Nevertheless, the thermal treatment significantly changed the catalyst activity (Figure 5-24), and FDCA selectivity registered after 4 h reaction time was 50% only. With regard to HMF conversion, the calcination treatment also decreased the rate of HMF transformation; in fact, HMF conversion registered after 30 min with the calcined Pd_1Au_6-TiO_2 sample was 82%. By further increasing the reaction time up to 1 h, the HMF conversion reached 100%, although many differences were observed in the products selectivity as compared to the dried catalyst. In fact, HMFCA, FFCA and FDCA were formed; however, while the transformation of FFCA to FDCA progressed with time, the concentration of HMFCA was constant during the experiment time, a clear indication that this intermediate did not undergo any consecutive transformation. The absence of reactivity for HMFCA with the concomitant increase in FDCA selectivity suggests that the pathway involving the former compound as the reaction intermediate for FDCA formation no longer took place, as already observed for monometallic Pd-TiO_2.

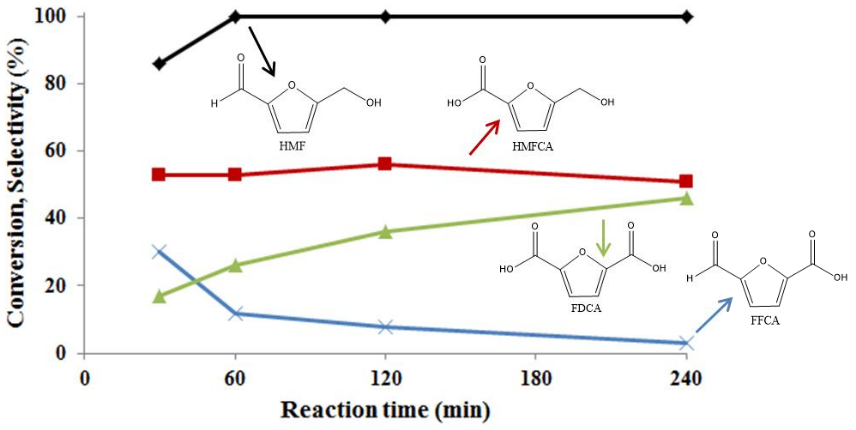

Figure 5-24 HMF conversion and product selectivities as a function of time on Pd_1Au_6-TiO_2 sample calcined at 300°C. Reaction conditions: temperature 70°C, O_2 pressure 10 bar, HMF:Metal:NaOH molar ratio 1:0.01:2. Legend: ♦ HMF conversion, ■ HMFCA selectivity, ▲ FDCA selectivity, X FFCA selectivity.

Taking into account the fact that the mean particle sizes for dried and calcined samples were very similar (i.e., 6 and 7 nm, respectively), this result suggests that the thermal treatment induces other modifications on the Pd-Au alloy. The significant change of activity, and a behaviour similar to that shown by the Pd catalyst, might be ascribed to the de-alloying of Au and Pd, with Pd segregation towards the surface upon calcination. This behaviour was already reported previously, where calcination led either to the production of an alloy with a Pd-rich shell and an Au-rich core, or to the formation of a Pd layer over a bimetallic nanophase[21,22]. Pd can migrate toward the outer part of the bimetallic nanoparticle and eventually form PdO, depending on both the support type and the nature of the thermal treatment adopted[23]. Nevertheless, tests performed using Pd-TiO_2 sample thermally treated at 300°C under different conditions (either under H_2 flow, or in air or first in air and then in H_2) demonstrated that neither the reduction, nor the calcination plus reduction treatment of the Pd catalyst could enhance FDCA selectivity (Figure 5-25). The segregation of Pd and/or PdO on the outer part of bimetallic nanoparticles might explain the change of reaction pathway for FDCA formation, similar to that one observed with monometallic Pd. Indeed, even with the calcined sample the formed HMFCA did not undergo any consecutive transformation.

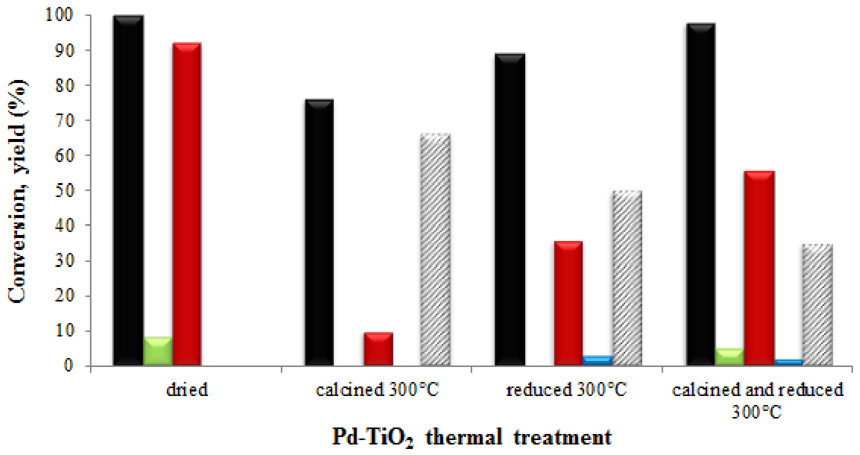

Figure 5-25 Comparison of catalytic activity for Pd/TiO_2 treated under different conditions. Reaction conditions: temperature 70°C, O_2 pressure 10 bar, HMF:Metal:NaOH molar ratio 1:0.01:2. Legend: ■ HMF conversion, 🟥 HMFCA selectivity, 🟩 FDCA selectivity, 🟦 FFCA selectivity, ▨ By-products selectivity.

Conversely, FDCA selectivity increased with reaction time and this clearly indicates the presence of a different pathway for its formation. As a matter of fact, the selectivity to FFCA decreased along with the reaction time increase; this might suggest a tandem reaction to FDCA through the formation of DFF and FFCA as intermediates.

For a better understanding of the reaction mechanism, some catalytic tests were conducted on calcined Pd_1Au_6-TiO_2 using the reaction intermediates as starting reagents (Table 5-12).

Entry	**Reagent**	**X_{HMF} (%)**	**Y_{FDCA} (%)**	**Y_{HMFCA} (%)**	**Y_{FFCA} (%)**	**Y_{HMF} (%)**	**Y_{BHMF} (%)**	**Y_{DFF} (%)**	**$Y_{By\text{-}products}$ (%)**
1	HMF (under N_2)	57	0	0	0	-	0	0	57
2	HMFCA	3	0	-	0	0	0	0	3
3	DFF	96	1	1	88	6	0	-	0
4	DFF (under N_2)	55	0	1	22	14	0	-	18
5	FFCA	11	1	0	-	0	0	0	10
6	FFCA (under N_2, no catalyst)	0	-	-	-	-	-	-	-
7	FFCA + HMF	-11 FFCA; 47 HMF	6	26	11	-	1	0	3
8	BHMF	70	2	20	9	34	-	2	3

Table 5-12 Reactivity experiments (X = conversion, Y = yield) from reaction intermediates over calcined Pd_1Au_6-TiO_2 catalyst. Reaction conditions: temperature 70°C, reaction time 30 min, O_2 pressure 10 bar, HMF:Metal:NaOH molar ratio 1:0.01:2.

First, a preliminary experiment was carried out by reacting HMF under N_2 (Table 5-12 – entry 1). This experiment made it possible to ascertain the absence of the base-induced disproportionation of HMF (Cannizzaro reaction) to HMFCA and 2,5-bishydroxymethylfuran (BHMF) under the reaction conditions used; however, a significant amount of HMF was degraded and a 57% conversion of HMF was observed after 30 min, producing a brownish solution.

The Cannizzaro transformation is the base-induced disproportionation of an aldehyde lacking a hydrogen atom at α-position to the carbonyl group. One molecule of the aldehyde acts as a hydride donor while the other functions as an acceptor, resulting in the production of an alcohol and a carboxylic acid. This reaction was recently demonstrated to be important in HMF transformation[24], and must be taken into account when studying furanic aldehyde reactivity.

In order to verify the ability of the catalyst to convert different reaction intermediates, HMFCA, DFF and FFCA were separately used as reagents. After 30 min reaction time, a very low conversion of HMFCA was shown (Table 5-12 – entry 2), which confirms the inability of the calcined catalyst to activate this molecule; moreover, no products of degradation were detected, indicating that the molecule is stable even in strongly basic conditions, probably because of the absence of the aldehydic group.

The use of DFF as the reagent (Table 5-1 – entry 3) resulted in the total transformation of this compound into FFCA, thus proving that the latter may be directly derived from DFF oxidation. DFF was reported to be an intermediate in HMF oxidation, especially when the reaction is carried out in the absence of a base[25], but it was not detected in our standard tests. Nevertheless, when our catalyst was used in extremely mild conditions (reaction temperature 25°C, 10 min, O_2 pressure 10 bar, HMF:NaOH 1:1), a small amount of DFF was formed, together with HMFCA and FFCA, in agreement with previously reported results. In the presence of O_2, the formation of a small amount of HMF made it possible to conclude that the Cannizzaro disproportionation makes a small, but non-negligible, contribution to DFF conversion, while the oxidation reaction is kinetically much more favoured. Nevertheless, when the reaction was carried out under N_2, besides FFCA important amounts of HMF and degradation products were observed (Table 5-12 – entry 4), suggesting the significant contribution of DFF disproportionation to the formation of FFCA and HMF (Scheme 5-3).

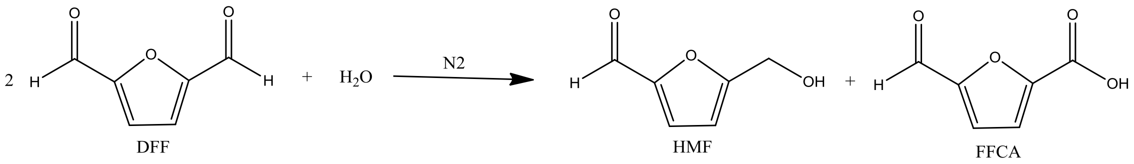

Scheme 5-3 Cannizzaro reaction of DFF under inert atmosphere in the presence of a base.

Unexpectedly, the conversion of FFCA was very modest under both O_2 and N_2 (Table 5-12 – entries 5 and 6), indicating that the calcined Pd_1Au_6-TiO_2 was almost inactive in FFCA conversion. Therefore, FDCA cannot derive exclusively from either FFCA oxidation and/or disproportionation: some additional parallel pathway for its formation should be hypothesized.

Indeed, when some HMF was added to the reaction medium (with a HMF/FFCA molar ratio 1:1), HMFCA, FDCA and BHMF formed in significant amounts (Table 5-12 – entry 7), an event which indicates the presence of a different path for FFCA conversion and FDCA production. In fact, during HMF oxidation FFCA may react with residual HMF by means of a Cannizzaro-type reaction, and this cross-disproportionation may yield different products: either (a) two molecules of HMFCA, which is a stable compound (entry 2 in Table 5-12), or (b) one molecule of BHMF and one of FDCA; the former is soon oxidised to HMF and HMFCA (entry 8 in Table 5-1). In fact, the products formed in the co-feed experiment (entry 7 in Table 5-12) were HMFCA, FFCA, FDCA, and traces of BHMF. However, due to the fact that HMF is a very reactive molecule (even with the less active calcined catalyst), and therefore the concentration of residual HMF was very low, disproportionation of FFCA with DFF (leading either to FDCA + HMF, or to HMFCA + FFCA) might also have contributed to products formation. Whichever was the reaction involved, our experiments showed clearly (see Table 5-12) that a disproportionation-type reaction involving FFCA as the reactant was the only route leading to FDCA formation, while FFCA itself was very slowly oxidised to FDCA. The formation of the right amount of BHMF, as expected from this disproportionation, could not be ascertained, due to the rapid oxidation of the latter under the conditions used, as confirmed by the test reported in Table 5-12 (entry 8).

A summary of the main reaction pathways involved in HMF oxidation on calcined Pd_1Au_6-TiO_2 under basic conditions is shown in Scheme 5-4.

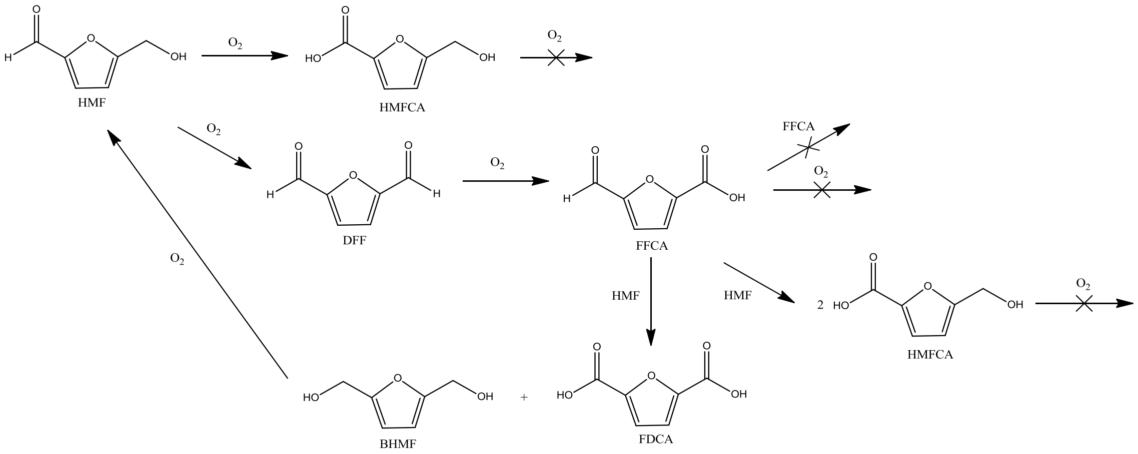

Scheme 5-4 Main reaction pathways for the oxidation of HMF on calcined Pd_1Au_6-TiO_2 catalyst.

We also carried out reactivity experiments aimed at elucidating the role of the Cannizzaro disproportionation with the dried Pd_1Au_6-TiO_2 sample. Preliminary results using FFCA as the reagent under differential conditions suggested the predominance of the oxidative pathway for FDCA formation, although a small contribution of the Cannizzaro reaction was detected; further studies are necessary to better clarify this point.

In conclusion, we demonstrated that the calcination treatment dramatically changed the reactivity of Pd_1Au_6-TiO_2, and altered the mechanism of FDCA formation from HMF. Indeed, this material was unable to oxidise molecules containing the –COOH functional group, such as HMFCA and FFCA.

3.2.3 Test using non-supported nanoparticles

PVP-protected Pd-Au nanoparticles with different structures (alloy and core-shell morphology) were tested as catalysts in order to confirm the presence of different mechanisms for FDCA formation in function of catalyst morphology. As previously reported, the synthesis of bimetallic Au(core)@Pd(shell) and Pd(core)@Au(shell) sols, with a Pd:Au molar ratio equal to 1:6, was carried out using the same method as for alloyed samples, but the second metal was added to the sol once the core-seed of the first metal had been formed. As detailed above, TEM, STEM and XEDS confirmed the expected distribution of metals within the nanoparticles; the synthetized sols were used as such in the reaction, without any support.

With the alloyed sol, the catalytic activity was very similar to that shown by the dried Pd_1Au_6-TiO_2 sample (Figure 5-26), despite the different nanoparticles dimension (3.9 nm for sols and 6.0 for the supported sample). This indicates that the effect of nanoparticles size on the reaction mechanism is negligible if compared to the effect of morphology, at least in the range of particles size investigated. The oxidation of HMF progressed through the rapid formation of HMFCA, followed by the subsequent oxidation to FFCA and then to FDCA. HMF conversion was always complete and the alloy was more efficient in converting HMFCA (in contrast to what shown with the corresponding supported calcined catalyst), forming FDCA with 80% selectivity after 4 h reaction time.

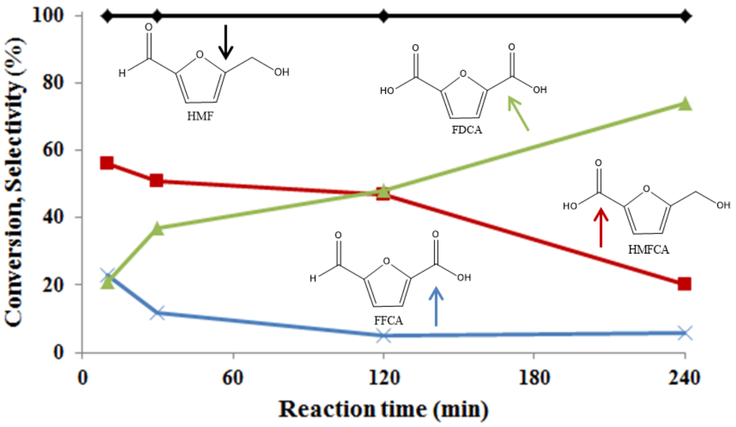

Figure 5-26 HMF conversion and product selectivities as a function of time on unsupported Pd_1Au_6 alloy nanoparticle. Reaction conditions: temperature 70°C, O_2 pressure 10 bar, HMF:Metal:NaOH molar ratio 1:0.01:2. Legend: ♦ HMF conversion, 🟥 HMFCA selectivity, ▲ FDCA selectivity, X FFCA selectivity.

Similar results were obtained using the Pd@Au sol, preferentially exposing Au atoms on the nanoparticle surface (Figure 5-27), which appeared highly active in HMFCA formation and conversion.

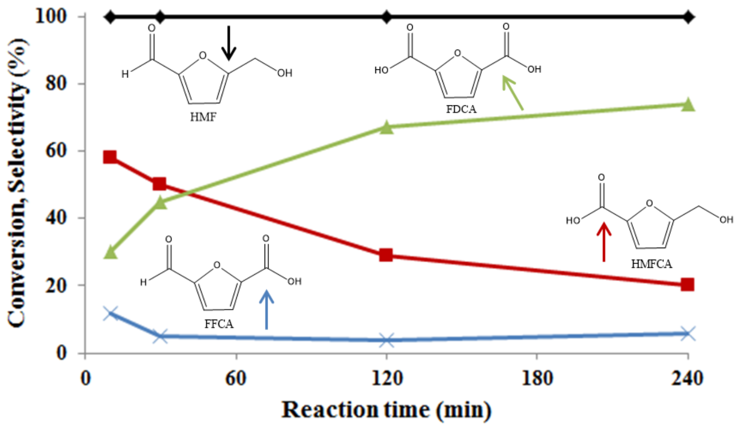

Figure 5-27 HMF conversion and product selectivities as a function of time on unsupported $Pd_1@Au_6$ core-shell nanoparticles. Reaction conditions: temperature 70°C, O_2 pressure 10 bar, HMF:Metal:NaOH molar ratio 1:0.01:2. Legend: ♦ HMF conversion, ■ HMFCA selectivity, ▲ FDCA selectivity, X FFCA selectivity.

Conversely, the use of a Pd-shell catalyst (Au@Pd) showed a very different trend (Figure 5-28). The sample was active in the first steps of the reaction network, producing both HMFCA and FFCA. However, the catalyst was poorly active for the subsequent oxidation of these molecules, as previously also observed for both the monometallic Pd-TiO_2 and the calcined bimetallic catalyst; correspondingly, the selectivity to HMFCA, FFCA and FDCA remained almost unchanged between 60 and 240 min reaction time, which suggests that Au is the key catalytic component under basic conditions.

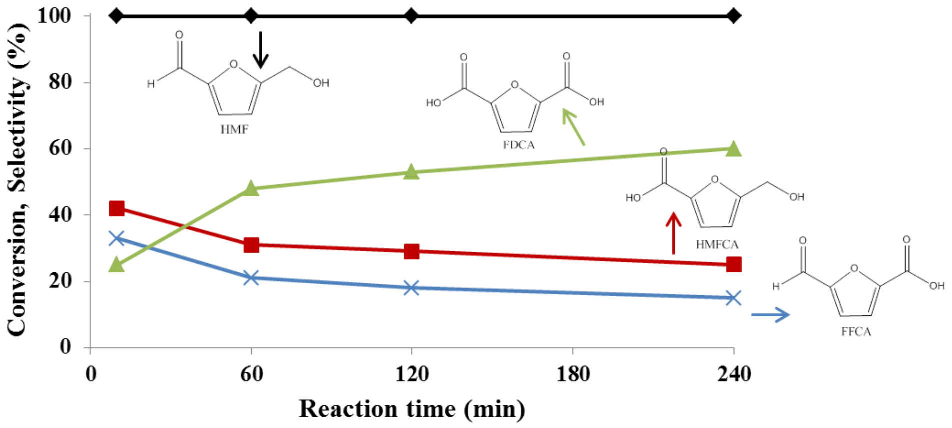

Figure 5-28 HMF conversion and product selectivities as a function of time on unsupported $Au_6@Pd_1$ core-shell nanoparticles. Reaction conditions: temperature 70°C, O_2 pressure 10 bar, HMF:Metal:NaOH molar ratio 1:0.01:2. Legend: ♦ HMF conversion, ■ HMFCA selectivity, ▲ FDCA selectivity, X FFCA selectivity.

5.6 Conclusions

The aerobic oxidation of 5-hydroxymethylfurfural in water over TiO_2-supported Au and Pd catalysts provides an environmentally benign route to 2,5-furandicarboxylic acid, an important compound serving as the starting point for the synthesis of bio-polymers.

Samples with different Pd:Au atomic ratio and morphology (alloy and core-shell) were prepared in order to investigate the effect of catalyst composition on catalytic activity and products selectivity. This study allowed us to conclude that the reaction network was strongly affected by catalyst composition. In fact, Pd-TiO_2 was poorly selective to FDCA, while the formation of the latter was strongly enhanced compared to Au-TiO_2 by alloying small amounts of Pd with Au. However, a thermal treatment of the supported Pd-Au alloy at 300°C led to the development of a catalyst whose behavior was similar to that shown by Pd-TiO_2, because of the segregation of Pd towards the outer part of the alloy nanoparticles, with Pd surface enrichment.

The reason for this behavior derived from the substantial inability of Pd and surface Pd-enriched alloys to oxidise the hydroxymethyl group of the intermediate compound, 5-hydroxymethyl furancarboxylic acid. With these catalysts, a different reaction pathway took place for 2,5-furandicarboxylic acid formation, involving a Cannizzaro-type reaction between the reactant, 5-hydroxymethylfurfural, and the intermediate compound, 5-formylfurancarboxylic acid. This mechanism was confirmed using core-shell nanoparticles, preferentially exposing either Au or Pd atoms.

---

[1] M. Blosi, S. Albonetti, G. Baldi, F. Gatti, M. Dondi, *Dyes Pigments* 94 (2) (2012) 355-362.

[2] S. Albonetti, M. Blosi, F. Gatti, A. Migliori, L. Ortolani, V. Morandi, G. M. Baldi, *Stud. Surf. Sci. Catal.* 175 (2010) 621-624.

[3] M. Blosi, S. Albonetti, S. Ortelli, A.L. Costa, L. Ortolani, M. Dondi, *New J. Chem*. 38 (2014) 1401-1409.

[4] A. Lolli, S. Albonetti, L. Utili, R. Amadori, F. Ospitali, C. Lucarelli, F. Cavani *Appl. Catal. A*: *General* (2014) *doi:10.1016/j.apcata.2014.11.020*

[5] W. Zhou, J.Y. Lee *Electrochem. Comm.* 9 (2007) 1725-1729

[6] T. Pasini, M. Piccinini, M. Blosi, R. Bonelli, S. Albonetti, N. Dimitratos, J. A. Lopez-Sanchez, M. Sankar, Q. He, C. J. Kiely, G. J. Hutchings, F. Cavani, *Green Chem*. 13 (2011) 2091-2099.

[7] S. Albonetti, T. Pasini, A. Lolli, M. Blosi, M. Piccinini, N. Dimitratos, J. A. Lopez-Sanchez, D. J. Morgan, A. F. Carley, G. J. Hutchings, F. Cavani, *Catal. Today* 195 (2012) 120-126.

[8] A. Shalkh, D. R. Parker, M. E. Janka, L. R. Partin, *US Patent* 2014/0142328 (2014) assigned to Eastman Chemical Company.

[9] N. K. Gupta, S. Nishimura, A. Takagaki, K. Ebitani, *Green Chem*. 13 (2011) 824-827.

[10] O. Casanova, S. Iborra, A. Corma, *ChemSusChem*. 2 (2009) 1138-1144.

[11] M.A. Lilga, R. T. Hallen, J. Hu, J. F. White, M.J. Gray, US 2010/0152470 (2010), assigned to Battelle Memorial Institute.

[12] S. E. Davis, L. R. Houk, E. C. Tamargo, A. K. Datye, R. J. Davis, *Catal. Today* 160 (2011) 55.

[13] S. E. Davis, B. N. Zope, R. J. Davis, *Green Chem*. 14 (2012) 143-147.

[14] S. E. Davis, A. D. Benavidez, R. W. Gosselink, J. H. Bitter, K. P. de Jong, A. K. Datye, R. J. Davis *J. Mol. Catal. A: Chemical* 388-389 (2014) 123-132.

[15] A. Villa, M. Schiavoni, S. Campisi, G. M. Veith, L. Prati, *ChemSusChem* 6 (2013) 609-612.

[16] S. Albonetti, A. Lolli, V. Morandi, A. Migliori, C. Lucarelli, F. Cavani, *Appl. Catal B* 163 (2015) 520–530.

[17] H. A. Rass, N. Essayem, M. Besson *Green Chem.* 15 (2013) 2240–2251.

[18] Z. Zhang, B. Liu, K. Lu, J. Sun, K. Deng *Green Chem*. 16 (2014) 2762-2770.

[19] A. Villa, D. Wang, D.S. Su, L. Prati, ChemCatChem. 1 (2009) 510-514.

[20] G. A. Somorjai, H. Frei, J.Y. Park, J. Am. Chem. Soc. 131 (2009) 16589-16605.

[21] J. Pritchard, M. Piccinini, R. Tiruvalam, Q. He, N. Dimitratos, J. A. Lopez-Sanchez, D. J. Morgan, A. F. Carley, J K. Edwards, C. J. Kiely, G. J. Hutchings, Catal. Sci. Technol. 3 (2013) 308-317.

[22] D. I. Enache, J. K. Edwards, P. Landon, B. Solsona-Espriu, A. F. Carley, A. A. Herzing, M. Watanabe, C. J. Kiely, D. W. Knight, G. J. Hutchings Science 311 (2006) 362-365.

[23] P. Paalanen, B.M. Weckhuysen, M. Sankar Catal. Sci. Technol. 3 (2013) 2869-2880.

---

[24] S. Subbiah, S. P. Simeonov, J. M. S. S. Esperança, L. Paulo N. Rebelo, C. A. M. Afonso, Green Chem. 15 (2013) 2849-2853.

[25] X. Wan, C. Zhou, J. Chen, W. Deng, Q. Zhang, Y. Yang, Y. Wang, ACS Catalysis 4 (2014) 2175-2185.

CHAPTER 6

Conclusions

5-hydroxymethylfurfural (HMF) oxidation to 2,5-furandicarboxylic acid (FDCA) was carried out under mild conditions using metal supported catalysts.

The results obtained in this work show that the catalytic activity is strongly influenced by:

- ✓ Type of support (TiO_2, CeO_2)
- ✓ Catalyst pre-treatment (calcination and washing in reaction conditions)
- ✓ Metal particles composition and morphology (Au, AuCu, Pd, PdAu both in alloyed and core-shell morphologies)

Au-TiO_2 catalyst was found to be very active for FDCA formation[1]; however, AuCu supported samples were more active and more stable than the monometallic counterpart. The most important feature for this type of catalysts is the formation of alloyed particles, characterised by smaller particles size. The alloy formation was responsible for the improvement in catalyst activity and stability; in particular, the sample with a metal molar ratio Au:Cu 3:1 showed the best catalytic performances[2].

On the contrary, ceria based catalysts seemed to be more influenced by the interaction between gold and support. The presence of alloyed copper did not enhance neither the activity nor the stability of the system, as we previously reported for TiO_2 based systems. PVP (polyvinylpyrrolidone) removal brought a great increase in the catalytic activity since it improved the contact of gold with cerium oxide (Figure 6-1). However, it is not easy to remove this stabilising agent and it remained partially on the bimetallic AuCu systems which are characterised by a greater PVP amount. This is the reason why an increase in FDCA yield was not observed after the washing treatment of Au_3Cu_1-CeO_2 catalyst. Calcination is the easiest way to eliminate PVP; however, particle size may increase because of the local exothermicity generated near the particle during the decomposition of the polymer. This effect is mainly observed in bimetallic sample, due to their higher PVP content[3]. However, if the catalyst is washed before calcination, particle sintering is limited because the exotermicity of the combustion process decreases. As a result, the sample that has been washed and then calcined has a higher FDCA yield that the calcined one.

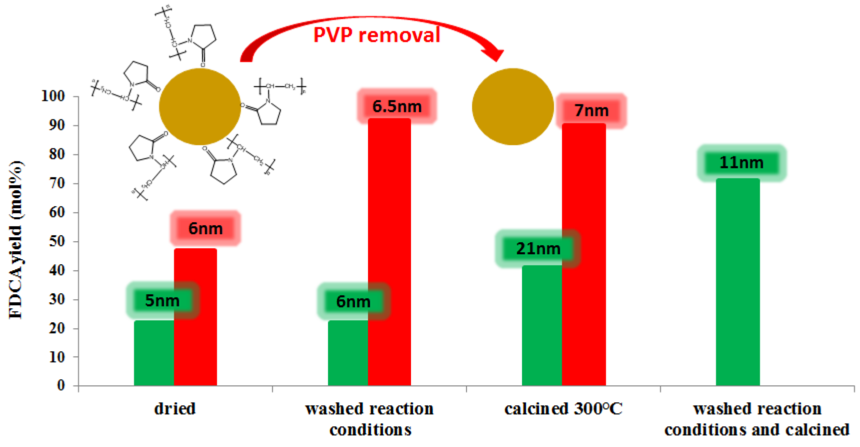

Figure 6-1 FDCA yield and metal particles size of Au-CeO_2 🟥 and Au_3Cu_1-CeO_2 🟩 catalysts as a function of different catalyst pre-treatments. Reaction conditions: temperature 70°C, reaction time 240 min, O_2 pressure 10 bar, HMF:Metal:NaOH molar ratio 1:0.01:4.

The preparation of cerium oxide using the hard template method allowed the formation of a support with high surface area and highly ordered mesoporous channels. However, with respect to the catalyst prepared with the commercial CeO_2 greater improvements were not observed, because of the presence of SiO_2 on the surface of the support. Residual silica, which remained from SBA-15 used for hard-template cerium oxide preparation, influenced negatively catalytic performance. Therefore, even if the mesoporous support was more promising with respect to the commercial one for redox properties and defective sites, silica presence was the most predominant factor. The positive effect which may be occurred in the presence of a high surface area, small particle size and surface defects was overcome by the presence of SiO_2, which avoided a proper gold-support interaction[4].

Finally, it was observed metal particles composition and morphology strongly affected the reaction network. In fact, Pd-TiO_2 was poorly selective to FDCA, while the formation of the latter was strongly enhanced compared to Au-TiO_2 by alloying small amounts of Pd with Au. However, a thermal treatment of the supported Pd-Au alloy at

300°C led to the development of a catalyst whose behaviour was similar to that shown by Pd-TiO_2, because of the segregation of Pd towards the outer part of the alloy nanoparticles, with Pd surface enrichment (**Figure 6-2**).

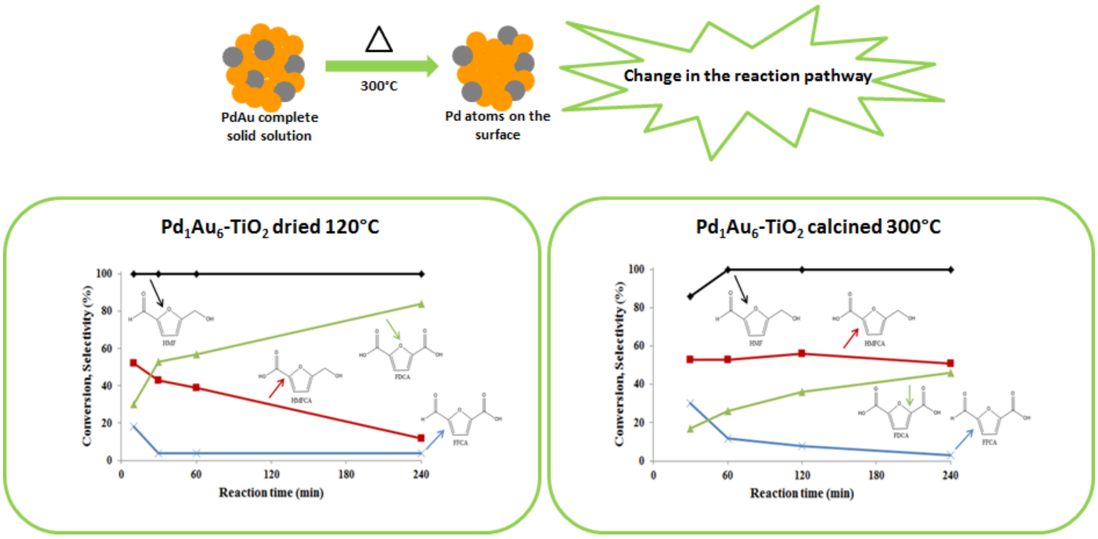

Figure 6-2 Change in particles morphology during catalysts calcination which led to a modification of the reaction pathway. Reaction conditions: temperature 70°C, O_2 pressure 10 bar, HMF:Metal:NaOH molar ratio 1:0.01:2.

The reason for the behaviour displayed in Figure 6-2 derived from the substantial inability of Pd and surface Pd-enriched alloys to oxidise the hydroxymethyl group of the intermediate compound, 5-hydroxymethyl furancarboxylic acid (HMFCA). On the contrary, for Au and homogeneous alloy PdAu based catalysts HMFCA decreased in the reaction medium since it was converted to FDCA. In the presence of catalysts with a Pd-enriched surface, a different reaction pathway took place for 2,5-furandicarboxylic acid formation, involving a Cannizzaro-type reaction between the reactant, 5-hydroxymethylfurfural, and the intermediate compound, 5-formylfurancarboxylic acid (FFCA). This mechanism was confirmed using core-shell nanoparticles, preferentially exposing either Au or Pd atoms[5] (Figure 6-3).

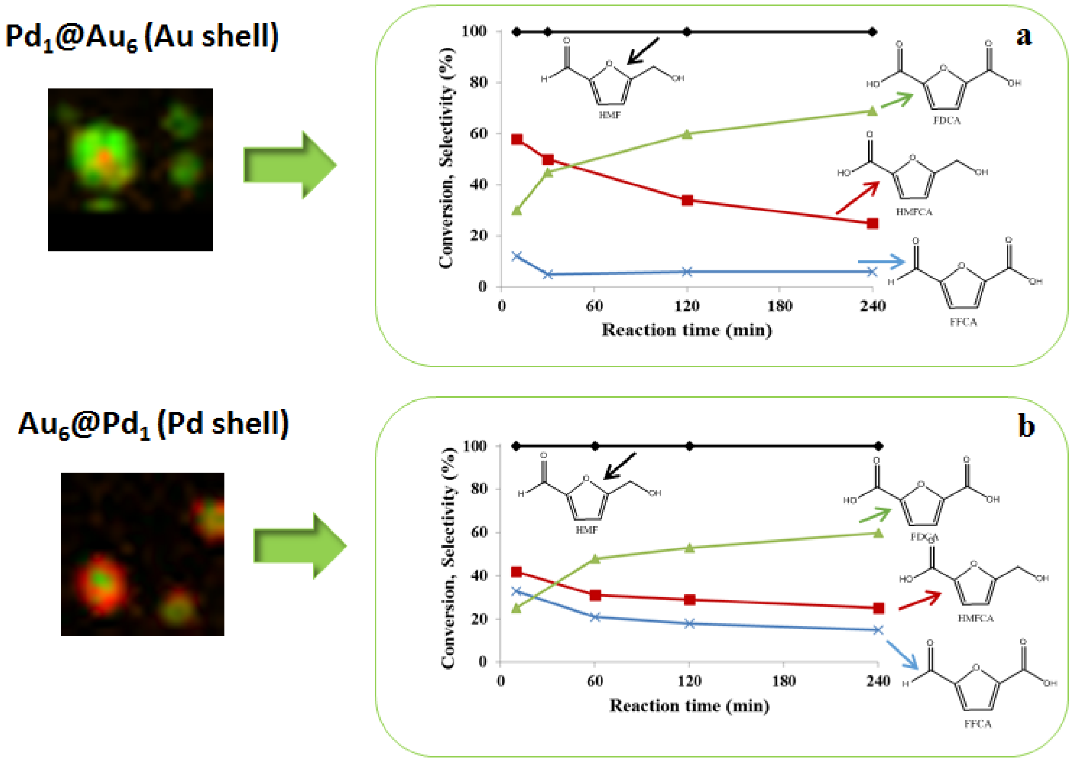

Figure 6-3 Different reaction pathway for nanoparticles exposing Au a) or Pd b) in the outer shell of the particle. Reaction conditions: temperature 70°C, O_2 pressure 10 bar, HMF:Metal:NaOH molar ratio 1:0.01:2.

---

[1] T. Pasini, M. Piccinini, M. Blosi, R. Bonelli, S. Albonetti, N. Dimitratos, J. A. Lopez-Sanchez, M. Sankar, Q. He, C. J. Kiely, G. J. Hutchings, F. Cavani, *Green Chem*. 13 (2011) 2091-2099.

[2] S. Albonetti, T. Pasini, A. Lolli, M. Blosi, M. Piccinini, N. Dimitratos, J. A. Lopez-Sanchez, D. J. Morgan, A. F. Carley, G. J. Hutchings, F. Cavani, *Catal. Today* 195 (2012) 120-126.

[3] S. Albonetti, A. Lolli, V. Morandi, A. Migliori, C. Lucarelli, F. Cavani, *Appl. Catal B* 163 (2015) 520–530.

[4] A. Lolli, F. Cavani, R. Amadori, S. Albonetti, M.G. Cutrufello, E. Rombi *in preparation.*

[5] A. Lolli, S. Albonetti, L. Utili, R. Amadori, F. Ospitali, C. Lucarelli, F. Cavani *Appl. Catal. A*: *General* (2014) *doi:10.1016/j.apcata.2014.11.020*